Universität Bonn
Physikalisches Institut

Development of a test beam telescope based on the ATLAS front end ASIC FE-I4

Theresa Obermann

Abstract: A beam telescope using FE-I4 readout chip based pixel modules of the ATLAS IBL upgrade was set up and tested. The data acquisition as well as the analysis were adopted from an already existing framework developed specifically for that purpose, namely EUDAQ and EUTelescope. By adding one FE-I4 based reference plane to the EUDET telescope, a region of interest trigger was implemented into the existing framework. Tests with this trigger were done using both the FE-I4 beam telescope as well as the EUDET telescope. A commissioning of the new trigger was done with a DEPFET sensor as device under test, showing that the data acquisition can be improved in terms of track efficiency to more than 80 %.

Universität Bonn

Physikalisches Institut

Development of a test beam telescope based on the

ATLAS front end ASIC FE-I4

Theresa Obermann

Dieser Forschungsbericht wurde als Masterarbeit von der Mathematisch-Naturwissenschaftlichen Fakultät der Universität Bonn angenommen.

Angenommen am: 14.08.2012

Referent: Prof. Dr. Norbert Wermes

Koreferent: Prof. Dr. Hartmut Schmieden

Contents

Introduction

Then a man named Tycho Brahe *evolved a way of answering the question. He thought that it might perhaps be a good idea to **look very carefully and to record exactly**...and then the alternative theories might be distinguished from one another. **This is the key of modern science and it was the beginning of the true understanding of Nature**...*

(Richard Feynman)

Central to the entire discipline of Physics is the concept of the experimental verification. It has been considered throughout the past four centuries and in the meanwhile has led to fascinating discoveries. First, and in direct relation to the Feynman citation, a model of gravitation was developed based on data that was taken from the observation of the position of the planets. In order to discover the nucleus inside the atom the same idea, to look very carefully and to disentangle the possible theories based on the data, was used by Rutherford. This concept has not changed in the past centuries, just our tools to do the observation evolved rather rapidly. In the following, the ATLAS[1] experiment, one of the most advanced observation tools in modern high energy physics (HEP), will be used to explain the needs of a versatile test beam telescope, whose development is the scope of this thesis.

The ATLAS experiment [1] is one of two general purpose detectors at the Large Hadron Collider (LHC) [2] at CERN[2] [3] at the French-Swiss border, near Geneva, which is a machine that brings protons to head-on collisions at very high energies. Currently collision energies up to a $\sqrt{s} = 8\,\text{TeV}$ are reached ($\sqrt{s} = 14\,\text{TeV}$ are to be expected). After the particle acceleration, the next step in a HEP experiment is the collision of the accelerated particles. The most interesting interactions

---

[1] A Toroidal LHC ApparatuS.
[2] Conseil Européen pour la Recherche Nucléaire.

involve short-lived particles that can not be observed directly with the detector as they decay before reaching it. However, the properties of the decay particles, that pass through the detector, can be measured. These particles constitute the final state of the interaction and a complete dataset containing information about the particles is called an event. In figure 0.1 these three steps of a HEP experiment are sketched.

The main purpose of the `ATLAS` detector is to reconstruct the event consisting of particles resulting from the collisions and ultimately to test the Standard Model (SM), which is - though incomplete - the most precisely tested theory of elementary particles. By doing so, one would be able to decide if the SM best describes the data or a new model is needed. Nevertheless, as mentioned, the SM is not yet complete. The `Higgs`-boson, the particle responsible for the generation of the mass of the exchange particles of the weak interaction, is one part of the SM which still lacks experimental proof. Its discovery would therefore strengthen this model, although it would not answer some of the most fundamental and still unresolved questions in particle physics today, as for example the matter-antimatter asymmetry, the abundance of dark matter and the unknown neutrino mass hierarchy. Recently, a new particle at the expected mass of the SM `Higgs`-boson has been discovered by both the `ATLAS` and the `CMS`[3] experiments [4, 5].

(a) input: accelerate and collide the protons head-on.

(b) interaction: many different theories try to model the way the particles interact.

(c) output: event display representing the particles resulting from the interaction.
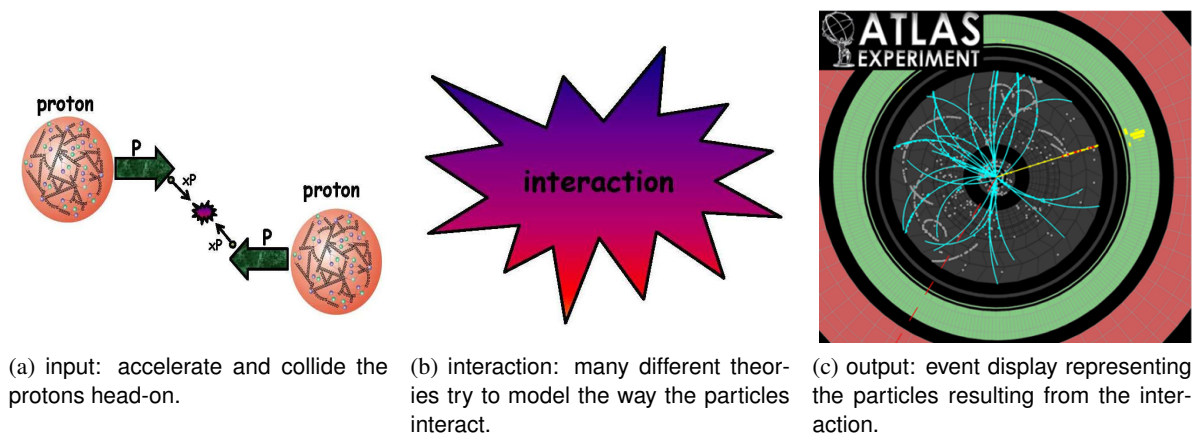
Figure 0.1: As a first step in a high energy physics experiment particles collide after having been accelerated. Then an interaction between the colliding particles takes place. The particles that emerge from this interaction are recorded with the detector and can be graphically represented through the shown eventdisplay (here one from `ATLAS` is shown).

For the particle detection and event reconstruction in `ATLAS` one needs to combine a variety of

---

[3]Compact Muon Solenoid.

sub-detectors in an onion-like arrangement around the interaction point. The whole detector needs to be able to completely measure the final state of a collision, that means to identify all the particles that come from the interaction point and measure their properties such as energy and momentum. Especially for neutrinos, particles that can only be identified through the concept of missing energy, an almost hermetic detector is needed such that most of the solid angle around the interaction point is covered.

In order to build, maintain and upgrade a huge detector like ATLAS a lot of research on detectors has to be done. Analysing new materials in order to test and compare their properties, which are significant for the application, is a common method. For example, diamond is a material recently in use in HEP, that is a strong candidate to be used for trackers in future experiments in the field. Before using a new technology, its properties have to be confronted against the technologies well established. Therefore, for a complete understanding of the new material properties, extensive testing has to be done. Parts of this testing can be accomplished with a beam telescope.

To perform specific detector tests, a beam telescope, placed in a particle beam and making use of common detectors whose properties are well understood, can be used. Consequently, a beam telescope is a useful tool for testing certain properties of new detector types. With it, properties like the efficiency, the spatial resolution or the charge collection uniformity of an unknown detector can be measured. The development of such a beam telescope, based on the integrated circuit FE-I4 [6] designed for the innermost layer of the ATLAS pixel detector currently being built, is the scope of this thesis.

Extensive use will be made of the infrastructure developed within the EUDET[4] project [7], a EU-project, which started in 2006 and ended in 2010. Its focus was detector research and development towards the International Linear Collider. The software packages for data acquisition (DAQ) - EUDAQ [8] - and for data analysis - EUTelescope [9] - will be used for the FE-I4 beam telescope developed in this work. For the detector specific DAQ of the FE-I4 readout chip the USBpix-system, developed in Bonn, will be used [10, 11]. Particle beams from ELSA[5], the accelerator complex in Bonn, DESY[6], a research facility in Hamburg, and CERN will be employed to study the FE-I4 telescope. Therefore

---

[4]Detector R&D towards the International Linear Collider.
[5]Electron stretcher ring - 'Elektronen Stretcher Anlage'.
[6]'Deutsches Elektronen Synchrotron'.

different setups with different beam energies will be presented in this thesis.

Chapter 1 will give an overview of the basic ideas of particle detection. Chapter 2 presents the materials and methods used in the measurements described in Chapter 3 and 4. The analysis of test beam data will be presented in Chapter 5 and a conclusion ends this work in Chapter 6.

Chapter 1

Basics of particle detection using semiconductor detectors

1.1 Principles of particle detection

The basic principle of the detection of any kind of particle is through its interactions with matter. Charged particles, like electrons or protons, interact electromagnetically with all particles that carry charge. Neutral particles like neutrons or neutral pions only interact with matter through the strong or weak force which differ in many orders of magnitude in strength and range compared to the electromagnetic interaction. In the following the interactions of charged particles with matter and the corresponding energy loss will be outlined. Neutral particles of any kind are not of interest for this thesis and are thus omitted here.

1.1.1 Energy loss of charged particles in matter

Charged particles passing through matter loose energy mainly through collisions with the electrons of the atoms that form the matter. The two most important ways of interacting are *ionization* and *excitation*. `Bethe` and `Bloch` calculated the energy loss of charged particles through ionization and excitation in 1932.

Bethe-Bloch-Formula

The energy loss of charged particles in matter can be described qualitatively by

$$-\frac{1}{\rho}\frac{dE}{dx} = K \cdot \frac{Z}{A} \cdot \frac{z^2}{\beta^2}\left[\frac{1}{2}\ln\left(2m_e c^2 \beta^2 \gamma^2 T_{max}/I\right) - \beta^2 - \frac{\delta}{2}\right] \tag{1.1}$$

where all particle and material properties are described in table 1.1 [12].

type	quantity	physical meaning
	dE/dx	energy loss per unit length
	z	charge in units of elementary charge e
particle properties	β	velocity in units of speed of light c
	γ	Lorentz-factor $\gamma = \sqrt{1/(1-\beta^2)}$
	T_{max}	maximum possible energy transfer in one collision
	Z and A	proton number and nucleon number
material properties	I	mean excitation energy
	ρ	density
constants	K	K=0.3071 $\frac{MeV\cdot cm^2}{g}$
	δ	density effect parameter

Table 1.1: Parameters of the Bethe-Bloch-formula, which describes the energy loss of charged particles in the range $0.05 < \beta\gamma < 500$.

Some characteristics of the Bethe-Bloch-formula, valid in the medium energy region of $0.05 < \beta\gamma < 500$, see figure 1.1, are:

- $1/\beta^2$-*decrease* in the interval $0.05 < \beta\gamma < 1$: charged particles loose more energy the slower they are, until they reach the Bragg-peak, where the highest energy deposition is reached. This peak develops where the particles are stopped. The particle current is constant over the whole length and drops to zero where the particles have come to a stop.

- $\ln\beta$-*increase* in the interval $2 < \beta\gamma < 500$: charged particles loose more energy at higher energies. Because of relativistic effects the transverse reach of the particles' electric field increases and therefore interactions at longer distances become possible. This effect increases the energy loss by 10 % with respect to the minimum energy loss.

- at $\beta\gamma \cong 3$ the curve has a *minimum*. The corresponding energy loss is given by $(dE/dx)_{mip} = 1.5\,\text{MeV cm}^2/\text{g}$ where mip stands for mimimum ionizing particle.
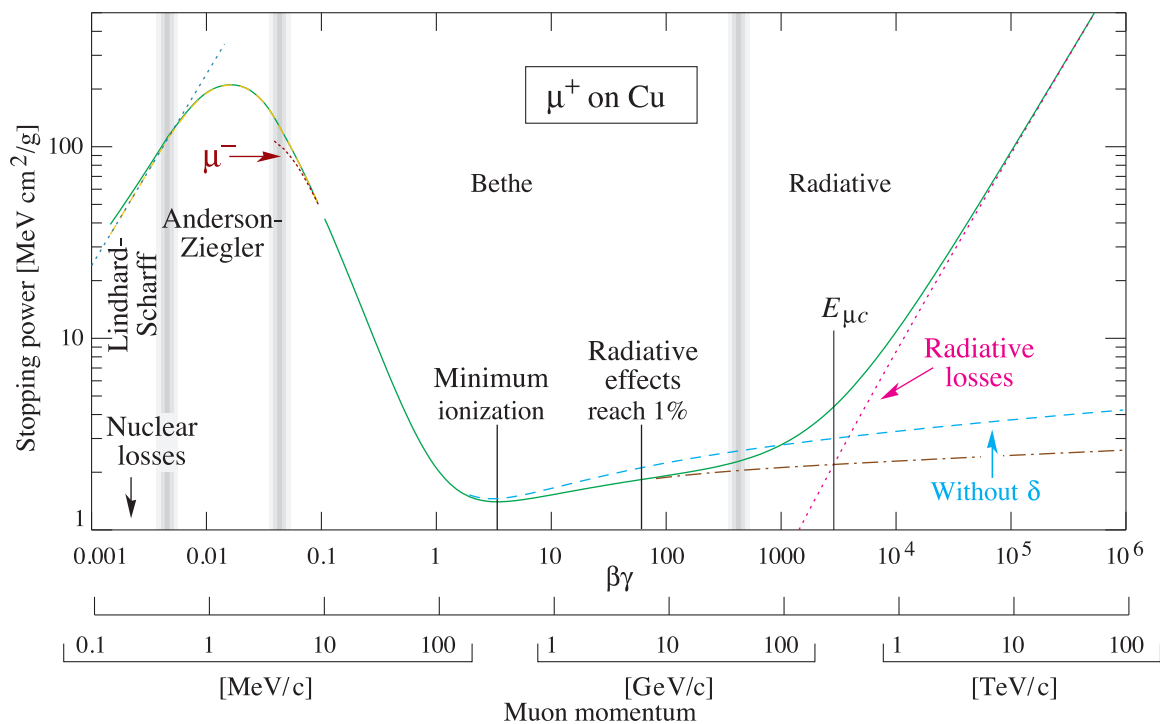

Figure 1.1: Energy loss of muons in copper. The `Bethe-Bloch`-region is between $2 < \beta\gamma < 500$ [12]. At higher energies radiative losses become important. The point where losses due to radiation equal those due to ionization and excitation is called critical energy and is shown in the figure as well.

In addition to ionization and excitation, also transition radiation and Čherenkov-radiation are incorporated in the `Bethe-Bloch`-calculation. Outside of the `Bethe-Bloch`-region the energy loss is no longer well described by the `Bethe-Bloch`-formula and other theories are needed for the low and high energy regions.

Bremsstrahlung anyhow is not included in the `Bethe-Bloch`-calculation and plays an important role for light particles at high energies (fig. 1.1), like e^-. They fall into the category of radiative losses since in the process of bremsstrahlung an electron emits a photon in the field of a nucleus when it is bend.

Landau-distribution

It is empirically shown that by measuring the same energy loss of a charged particle with a thin detector - thickness $\mathcal{O}(10-300\,\mu\text{m})$ - many times, the energy deposition follows a Landau-distribution, see figure 1.2 for pions of an energy of 500 MeV in silicon. The long tail towards higher energy
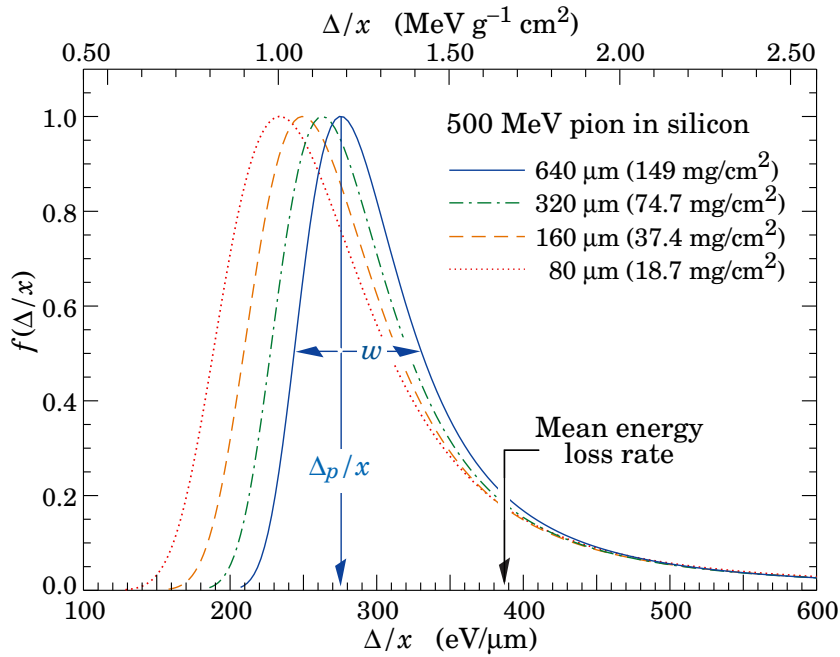

Figure 1.2: Landau-distribution of the measured energy loss of pions in four different thick silicon sensors [12].

losses is due to δ-electrons. These are secondary electrons which have a kinetic energy $T_{\text{kinetic},\delta}$ that is much bigger than the mean excitation energy and consequently the δ-electrons can further ionize neighbouring atoms themselves. They deposit additional energy in the detector and cause entries at high energy values. As a result, the most probable value of the energy loss $\left(dE/dx_{\text{mpv}}\right)$ is always smaller than the mean value of energy loss $\left(dE/dx_{\text{average}}\right)$. δ-electrons have a clear signature in the detector with an energy deposition over a comparatively large distance. These energy despositions come in addition to the average energy deposition of a mip and might lead to false hit reconstructions. Possibilities to reduce this effect make use of the long track signature of the δ-electrons and will be explored later in the analysis of the test beam data.

δ-electrons and energy transfer T

More information on δ-electrons is necessary to understand why they cause the long tail of the `Landau`-distribution. In order to discern δ electrons from electrons that come from `Bethe-Bloch`-energy losses one defines their kinetic energy to fulfill the following relation - $T_{\text{kinetic},\delta} \gg I$ - with I the mean excitation energy of the material, e.g. for almost all common detector materials I is of $\mathcal{O}(10\,\text{eV})$. This sets already a lower limit to $T_{\text{kinetic},\delta,\text{min}}$ which is $\mathcal{O}(10\,\text{keV})$. Then, for some detectors to cause an effect, this limit might be changed due to the geometrical measures of the device. The number of δ-electrons generated in a $200\,\mu$m thick silicon slice within a certain energy range can be calculated by

$$N_\delta \;=\; \frac{1}{2} K \rho \frac{Z}{A} \frac{z^2}{\beta^2} x \left(\frac{1}{T_{\delta,\text{min}}} - \frac{1}{T_{\delta,\text{max}}} \right) \cdot N_0 \;\Rightarrow\; N_\delta(200\,\mu\text{m Si}) = 3.6\,\text{keV} \left(\frac{1}{T_{\delta,\text{min}}} - \frac{1}{T_{\delta,\text{max}}} \right) \cdot N_0 \quad (1.2)$$

where N_0 is the rate of incoming particles, x the thickness, here $200\,\mu$m, and all other parameters as defined before [12]. The value for $T_{\text{kinetic},\delta,\text{max}}$ depends on the incoming particle and its velocity. The angle under which δ-electrons are emitted plays an important role for the energy deposition inside the detector. It turns out that δ-electrons follow an angular dependence like $1/\cos^3\theta$ where θ is the angle between the direction of the incoming particle and the direction of the outgoing δ-electron. As a result most δ-electrons get emitted under an angle close to $90\,°$. This causes the δ-electrons, created by a particle traversing perpendicular a thin detector to release all their energy inside the detector, see 1.3a.

To decrease the influence of multiple scattering, most semiconductor detectors are made especially thin In `ATLAS` the inner detectors cover the surface of a cylinder around the beam pipe. The pixel detectors used in this work have a thickness of approximately $200\,\mu$m and expand to roughly $2\,$cm x $2\,$cm in the perpendicular plane. Consequently a measurable effect from δ-electrons is likely to show up in the deposited energy of the pixels. In figure 5.3 the hit map of the `ATLAS` FE-I4 with a $200\,\mu$m thick sensor is shown for a test done with a radioactive source. One can clearly see an elongated track in the lower middle of the hit map, which is the clear signature of a δ-electron.
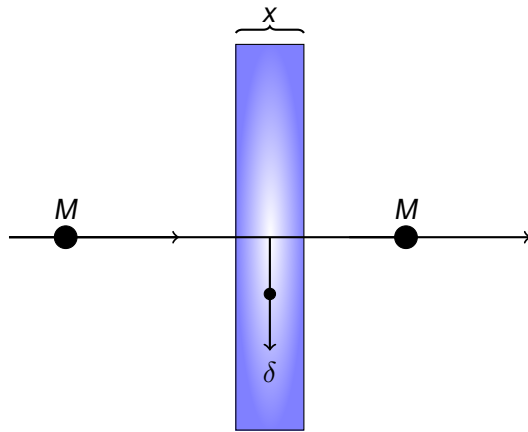
(a) Scattering of a particle of mass *M* off an electron at rest in a thin detector of thickness *x* for the most probable scattering angle θ which is close to $90°$.
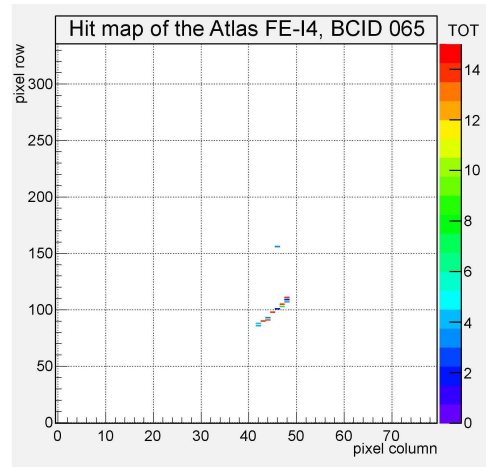
(b) Measured track with a pixel detector with FE-I4 readout. The elongated track, starting with a burst of high energy depositions at one end and evolving with smaller energy depositions to the other end, between columns 40 and 50 and rows 80 and 120, is a clear signature of a δ-electron.

Figure 1.3: Creation of a δ-electron in a thin detector and signature of a δ-electron in a pixel detector using the FE-I4 readout ASIC.

1.1.2 Multiple scattering effects

Particles passing through matter undergo many small angle scattering processes which are mainly due to `Coulomb` scattering from nuclei, see figure 1.4. This `Coulomb` scattering is well described by
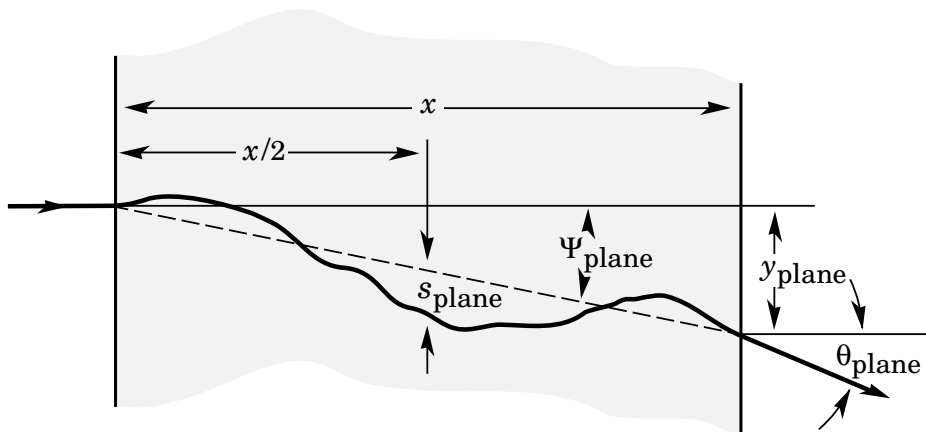

Figure 1.4: A particle that passes through matter is scattered many times by small angles. The total scattering angle is θ_{plane} - that is shown here - and is the same as θ_{rms} [12].

the Molière theory. For small deflection angles the distribution of the scattering angles is roughly Gaussian with a width θ_{rms}, which is called rms multiple scattering angle. This angle depends

strongly on the momentum of the particle and on the thickness of the material and can be calculated by

$$\theta_{\text{rms}} = \theta_{\text{plane}} = \frac{13.6\,\text{MeV}}{\beta \cdot p} \cdot z \cdot \sqrt{\frac{x}{X_0}} \left(1 + 0.038 \cdot \ln \frac{x}{X_0} \right) \tag{1.3}$$

where β is the velocity in units of c, p is the momentum in MeV/c, z is the charge and x is the thickness of the material and X_0 is the radiation length. For all vertex and tracking detectors it is crucial to reduce the material in order to decrease the displacement of the particle due to multiple scattering.

1.2 Principles of semiconductor detectors

Semiconductor detectors play a crucial role in particle physics and have a lot of applications in various other fields. The most basic silicon semiconductor detector is nothing else than a diode operated in reverse biasing. Such a diode consists of two differently doped pieces of silicon, n-doped and p-doped, put together.

PN-junction or diodes

A diode right after the formation and before the equilibrium is shown in the upper part of figure 1.5. The electrons in the n-doped region diffuse into the p-doped region and the holes in the p-doped region vice versa. This happens until an equilibrium sets in. A consequence of this development is the creation of a space charge region that is free of mobile charge carriers. The width of the free space charge or depletion region d, is given by the sum of both depletion widths in the p- and n-region, x_p and x_n respectively, which depend on the doping concentration $N_{A,D}$ and the applied voltage V_{bias} across the junction, as follows

$$d = x_p + x_n = \sqrt{\frac{2\epsilon V_{bias} N_D}{eN_A\left(N_A + N_D\right)}} + \sqrt{\frac{2\epsilon V_{bias} N_A}{eN_D\left(N_A + N_D\right)}} \qquad (1.4)$$

where the permittivity ϵ is a material constant and N_A and N_D are the numbers of acceptors and donors, respectively. Both widths x_p and x_n are approximately of the same length if $N_A = N_D$, see the second plot of figure 1.5 for $V_{bias} = 0$ and the third plot of figure 1.5 for $V_{bias} \neq 0$. But this is not the general case in most applications, as for example in a typical semiconductor detector, see the lower part of figure 1.5, where a highly doped region p^+ interfaces with a normally n-doped region. The diode is in general an electronics device which can have two defined states. Depending on the applied voltage across the junction, the diode can be open in a sense that there is a current going through it (forward bias) or it can be closed, in which case no current flows (reverse bias). In forward biasing the positive electrode is connected to the p-doped region which enhances the current through the diode exponentially. In reverse biasing the negative electrode is at the p-doped region and no current flows.

The depletion region is exactly the region that is important for the detection of charged particles.
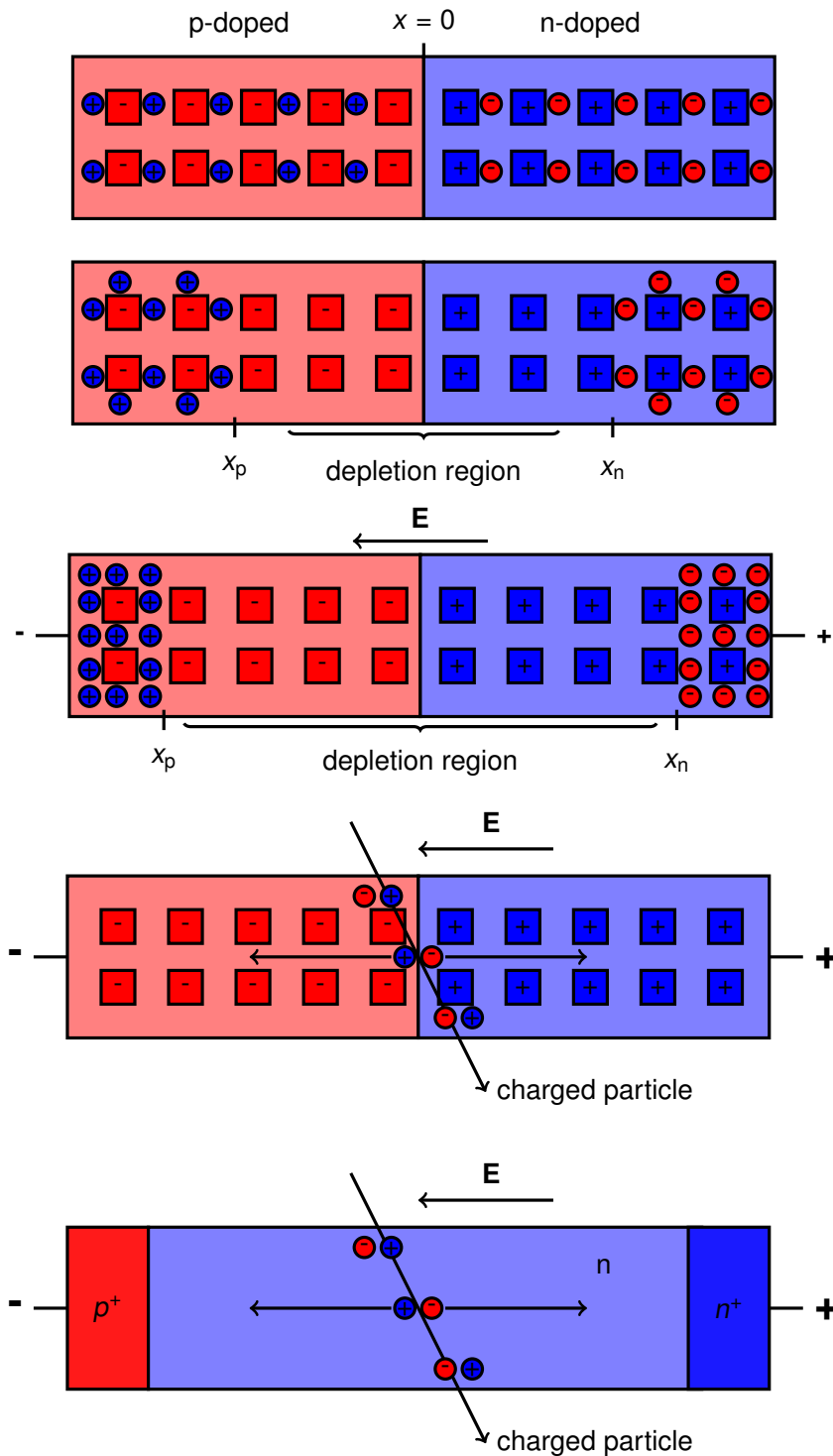
Figure 1.5: From pn-junction to sensitive detector volume. First all charge carriers are homogeneously distributed. Then the free charges diffuse until an equilibrium sets in. In order to increase the space charge region an electric field can be applied to the junction. Through the application of a high enough external voltage all free charge carriers can be removed from the pn-junction. A typical semiconductor detector has the doping configuration shown in the lowest part. It consists of two highly doped and a normally doped region.

If a charged particle passes through the depleted region it sets free charge carriers along its path, e^-h^+-pairs, which get - due to the applied voltage - collected at the electrodes. While moving according to the electric field (figure 1.5), the charge carriers induce a signal at the electrodes, which has be further processed by electronic circuits. The diode can be fully depleted by applying the proper reverse biasing, leaving no free charge carrier in the whole bulk. The energy loss in the whole volume contributes therefore to the signal.

1.2.1 Amplification and noise

Amplifiers are needed to amplify the weak signal coming from the semiconductor detector such that it can be further processed for storage and analysis by a dedicated circuit. Noise is amplified in the same way as the signal. Several amplifiers with special properties depending on the application have been developed. The type used here, the charge sensitive amplifier (CSA), has the property that it amplifies a signal in such a way that the amplitude of the output signal is proportional to the deposited charge by integration of the signal current, see figure 1.6.
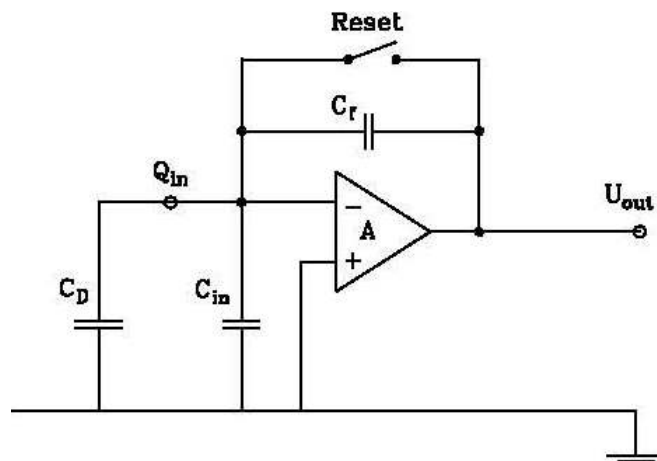
Figure 1.6: Charge sensitive amplifier circuit [13].

In order to flatten the steep rise, cut the long tail and improve the signal to noise ratio a shaper is used after the preamplifier. Noise can be minimized by using differential elements like high or low pass filters, that differentiate or integrate the signal respectively. The high pass filter causes the signal to fall more rapidly where the low pass filter decreases the rise time, see figure 1.7. The time constants are given through $\tau_{d,i} = R_{d,i} \cdot C_{d,i}$ where $R_{d,i}$ and $C_{d,i}$ are the corresponding resistance and

capacitance. A combination of both elements results in a filtering of low and high frequencies. As
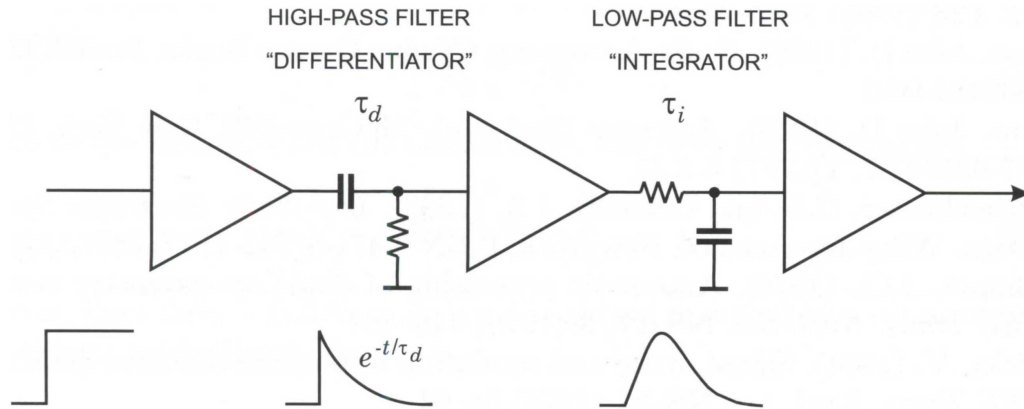

Figure 1.7: Noise filtering and signal shaping in a RCCR filter following a charge sensitive amplifier [14].

in a first approximation the noise level is independent of the frequency, whereas the signal usually

lies in a defined frequency band, the filtering will improve the signal to noise ratio.

Noise is the random electrical fluctuation. For estimating the noise of a semiconductor detector

system the circuit used for operating the detector needs to be analysed. A simple example of such

a circuit is shown in the left of figure 1.8. The capacitance C_d represents the detector that is biased
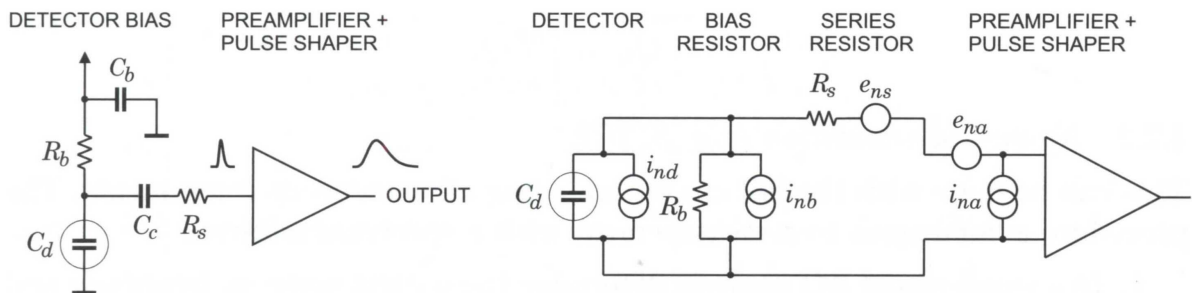
Figure 1.8: A detector front-end circuit and its equivalent circuit for noise calculations. [14].

through the resistor R_b. The capacitor C_b serves to protect the circuit from any external interference

coming through the bias supply line to ground and the capacitor C_c blocks the bias voltage from

the amplifier input. Any resistance between the sensor and the preamplifier input is represented

through the series resistance R_s. The noise sources in this circuit, shown in the right of figure 1.8,

are the following:

- Shot noise of the sensor leakage current acting as a noise current. As the sensor is operated

  in reverse biasing ideally no current flows through it. But, through thermal excitation, it is

possible that charge carries are generated, the current associated with this process is the leakage current. As shot noise is the quantity fluctuation of charge carriers that are being injected independently of one another this mechanism applies here. This random charge injection into an element, here the sensor, can be simulated by a parallel current source supplying the current i_{nd}.

- Thermal noise in all resistances. In the series resistor R_{s}, the fluctuation of the thermal velocity of charge carriers acts as a noise voltage e_{ns}. Any noise voltage created by the bias resistance R_{b} leads to a noise current i_{nb} flowing through the sensor and any resistance that is in parallel to it.

- In contrast to the above mentioned sources, which are both frequency independent, 1/f-noise is a frequency dependent quantum fluctuation and it exists in amplifiers. It varies with $1/f^{\alpha}$ where $0.5 < \alpha < 2$ is found experimentally. 1/f-noise is not completely understood, yet different explanations exist. One idea is that it is the result of the scattering of the charge carriers off lattice defects. At such defects the charge is trapped and released after a specific time resulting in a frequency dependent behaviour. In the amplifier both 1/f-noise and white noise add up and create a noise current i_{na} and a noise voltage e_{na} at its input.

All these noise sources add up to the total noise of the detector system.

A common quantity to estimate the noise is the equivalent noise charge (ENC). The ENC is the amount of charge $[e^-]$ that would be needed at the input of the preamplifier in order to create an output that is as large as the noise level. Assume that 10.000 electrons at the input create a signal of 1 V at the output and the measured noise level is about 10 mV. The ENC then simply is 100 electrons.

Chapter 2

Materials and Methods

In high energy physics hybrid pixel detectors are meanwhile a mature technology used by many experiments. One advantage of the hybrid technology is the immediate data processing, which allows for a fast and parallel readout of all channels. As a result such a detector can deal with high hit occupancies. Another advantage is the radiation hardness. Further, hybrid pixel detectors yield a large signal to noise ratio and have a low leakage current. However, reading out a lot of channels in parallel has a disadvantage concerning the high power consumption. As covering large areas is expensive and the number of pixel channels rises fast when increasing the radius of the pixel detector, hybrid pixels are only suitable for a region near the interaction point.

Other interesting silicon detector structures are Monolithic Active Pixels (MAPS) as well as DE-Pleted Field Effect Transistors (DEPFET). MAPS is the choice of sensor for the EUDET project as well as the AIDA telescope because very small pixel sizes with low material budget and low power consumption can be made with this technology. DEPFETs are used in this thesis as devices under test. Their design goal is a small pixel size as well as a radiation tolerance required for their environment, keeping the material budget also in very low levels.

The ATLAS experiment makes use of hybrid pixel detectors with a n-in-n structure, that means that a highly n-doped region is connected to a normally n-doped region. The complete pixel detector is made out of rectangular pixels that have 50 μm pitch in r-ϕ-direction and 400 μm pitch in z-direction resulting in resolutions of about 12 μm and 100 μm respectively. The pixels are arranged in three cylinders and six disks with in total 1744 modules, each consisting of 16 readout chips with 2880 channels. Summing this up the pixel detector, shown in figure 2.1a, has about 80 million pixels [16]

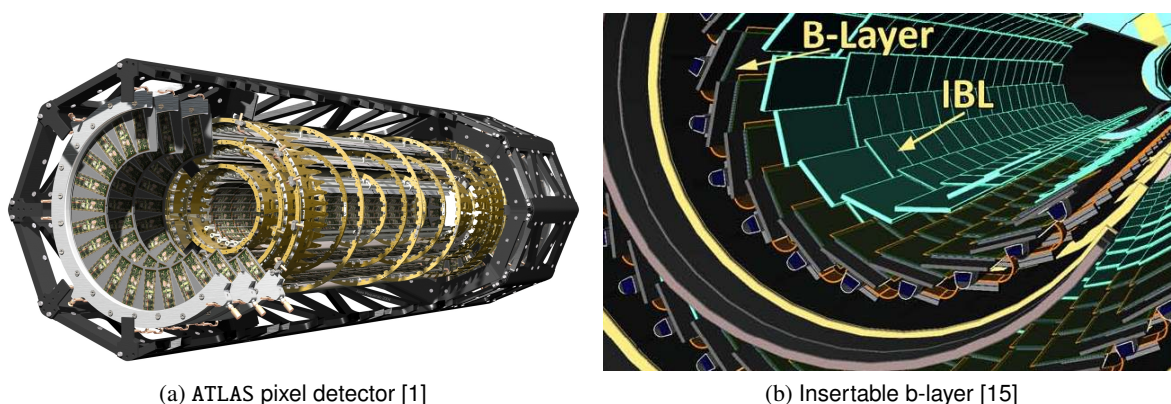(a) ATLAS pixel detector [1]   (b) Insertable b-layer [15]

Figure 2.1: The ATLAS pixel detector with its three layers as they are arranged around the beam pipe. The IBL will be placed between the current innermost layer and the beam pipe.

and therefore makes out half of the channels of the complete ATLAS detector.

Shown in figure 2.1b is the so called Insertable B-Layer (IBL). It is a new layer, which is meant to improve the reconstruction of the decay vertices of b-mesons and will be inserted between the beam pipe and the current innermost layer, the B-Layer. Since this layer will be closer to the interaction point than the B-Layer, it will be exposed to a higher particle flux and radiation dose. Simulations show that the hit loss of the readout Application Specific Integrated Circuit (ASIC) FE-I3 - currently installed in the ATLAS pixel detector - increases at higher luminosities, see figure 2.2. Consequently a new chip (the FE-I4) is needed for the first upgrade of the ATLAS detector in 2013 after what the expected luminosity is 10^{34} cm^{-2}s^{-1}. This ASIC then has to withstand a radiation dose of 250 Mrad in ten years. To cope with these requirements, some changes of the ASICs design were necessary. They are explained in detail in [17].

Hybrid pixel detectors are the devices used as telescope reference planes in this thesis and therefore the focus of the following explanations will be on their functionality.

2.1 Hybrid pixel detectors and sensors

Hybrid pixel detectors are devices which consist of a sensor and a readout chip that are put together through a technique such as bump-bonding, see figure 2.3a. As mentioned above, the advantages of hybrid pixel detectors are that the signal of all channels is fast processed in parallel and that they are very radiation tolerant. It is possible to use different technologies for the sensor and
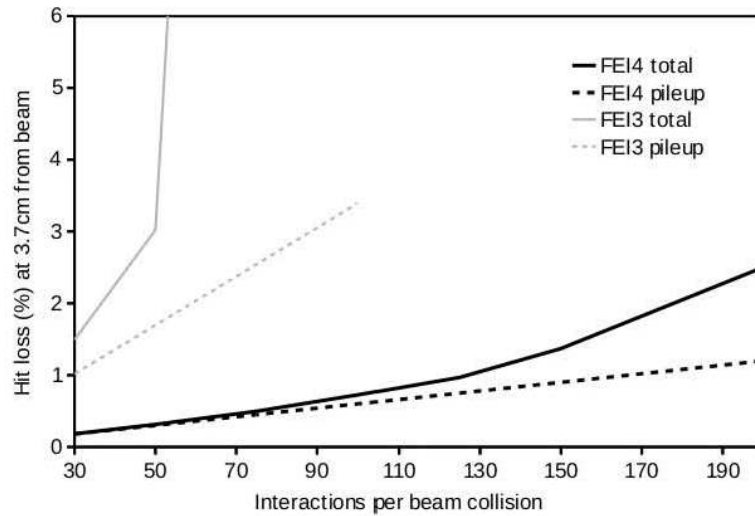
Figure 2.2: Hit loss of readout chips FE-I3 and FE-I4 in dependence of hit rate. For the IBL the expected interactions per beam collision is 75 [18].

the readout chip, which allows for different combinations of those in order to further improve the radiation hardness of the whole device. A disadvantage, however, is the high power consumption and the material budget.

A goal in high energy physics is to make the devices as thin as possible such that the particles loose as little energy as possible and to reduce multiple scattering in order not to disturb its path. Therefore efforts are made to keep both parts, the sensor and the readout chip very thin. Another approach is to have a single device through 3D integration or to improve the currently available monolithic detectors in terms of radiation hardness. As for today, hybrid pixel detectors are the device of choice in the ATLAS vertex detector and they will be used for the telescope developments in this work.

As already mentioned various sensor types for detector upgrades are currently under investigation. The most thoroughly studied type is the planar Si sensor shown in figure 2.3, see [19]. Planar pixel sensors are pn-junctions with a geometry like the one shown in figure 2.3b. One can see that the n^+-doped region is pixelized whereas the other side is flat throughout. The detector thickness is $\mathcal{O}(200\,\mu\text{m})$. The pitch can be as small as 50 μm. Sensors with a pitch of 50 μm and 250 μm will be used here. Their size is made to fit to the readout chip to which they are connected.

(a) Sketch of a hybrid pixel detector [19]. (b) Schematic of a planar n-in-n type sensor.
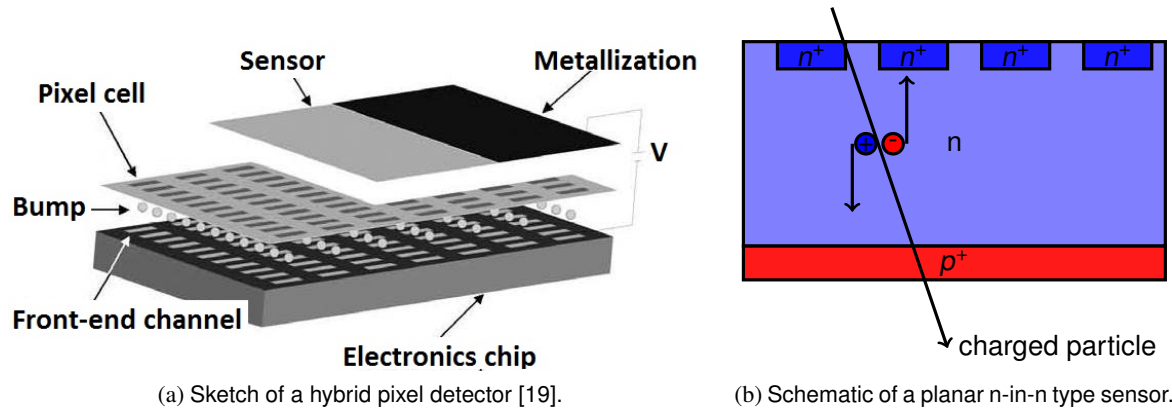
Figure 2.3: Schematic of a hybrid pixel detector with a sensor bump-bonded to a readout chip and a cross-section of a planar pixel sensor.

2.2 Readout electronics

To read out the sensor signal a front-end chip is needed. The chip used here, the FE-I4, can amplify and discriminate the signal of either the charge generated in the sensor or a known injected charge for testing purposes. It has been developed for the `ATLAS IBL` and has the following properties:

- rectangular pixels with pitches of $50\,\mu$m in r-ϕ direction and $250\,\mu$m in *z*-direction

- in total 80 columns ($250\,\mu$m pitch) and 336 rows ($50\,\mu$m pitch)

- size 18.6 mm x 20 mm

- feature size 130 nm, CMOS technology, high logic density.

Each pixel has the same analog circuitry. Consequently, to understand the analog functionality and how the chip is operated, it is crucial and sufficient to understand this one circuit.

2.2.1 Circuit of one pixel cell

The signal path from the creation of the charge in the depletion zone to the digital processing shall be described with the help of figure 2.4, where the complete analog circuit of one pixel of the FE-I4 is depicted. A charged particle traversing the sensor sets free charge carriers along its path - e^-h^+-pairs. Through their drift movement, due to the applied electrical field, they induce a signal at the preamplifier input. There the signal gets amplified by a CSA. The integrating capacitance
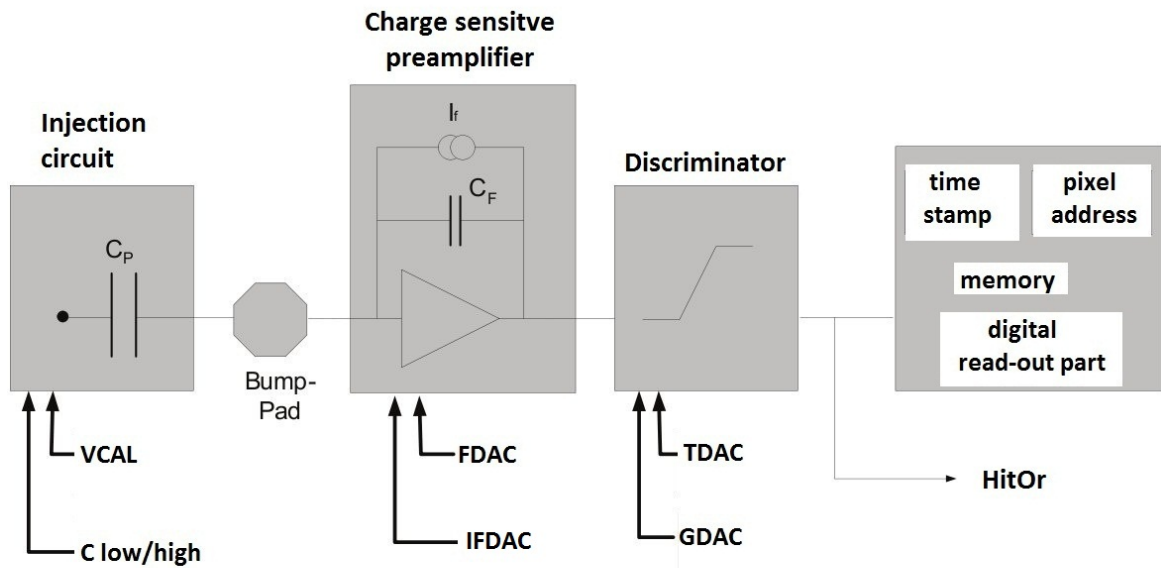
Figure 2.4: Injection circuit, preamplifier, discriminator and digital readout part of the FE-I4. The HitOr signal, which will be used to trigger on a region of interest in the following is the signal directly at the output of the discriminator [20].

of the CSA gets discharged by a constant current leading to a triangular shape of the signal at the output of the CSA. At the discriminator the signal gets compared to an adjustable threshold voltage and the output is a pulse with a length that corresponds to the time that the signal was above the threshold of the discriminator. Due to the triangular shape of the signal at the input of the discriminator the length that the signal stays above a certain threshold is proportional to the originally deposited charge. Therefore one measures the deposited charge in the number of clock cycles that the signal is above a certain threshold, the time over threshold (ToT), see figure 2.5.

The data, consisting of a time stamp of the start of the signal as well as the duration in terms of ToT as well as the pixel adress, is further processed by the digital part of the DAQ chain. Here a comparison between two counter values in the pixel cell, one for the time that has passed after a hit happened and one for the trigger latency, is done. By doing so, the FE-I4 only sends out the data of triggered events. This data is transferred to the periphery of the chip, sent out to the DAQ system and stored.
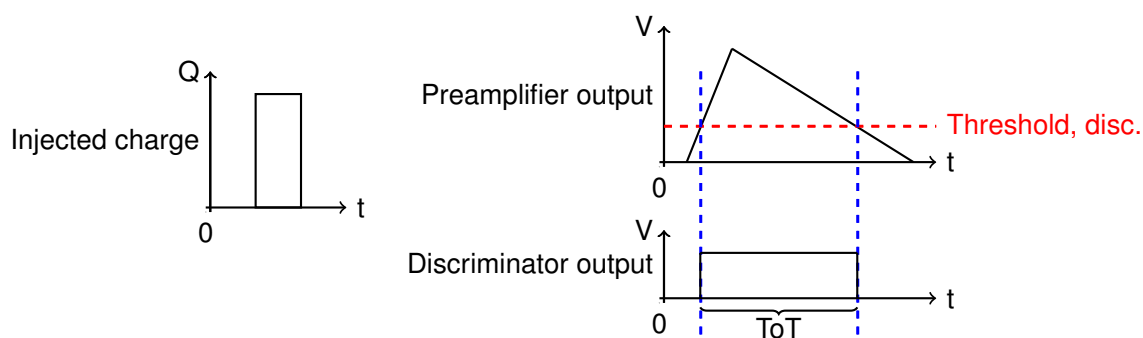
Figure 2.5: The injected charge pulse at the input of the preamplifier creates a triangular signal at its output. After being disciminated this signal is rectangular with the length being the ToT.

2.2.2 Creation of the HitOr signal

The discriminator output signal of all pixels is OR'ed together to form the HitOr signal of the chip. The time delay between the creation of the charge in the sensor and the HitOr signal after the discriminator is about 20-30 ns, see [6]. Then the HitOr signal acts as a gate to an nmos-transistor which is OR'ed with all other pixels of the same column, as can be seen in figure 2.6. The line to which all the nmos-transistors are connected is kept high on the potential Vdd by a constant current source as long as no transistor is open. As such the transistors act as pull-down transistors. In order for the HitOr signal to be high in case of a hit and low in case of no hit the signal gets inverted at the end. The lines of two columns are then OR'ed together and act again as an input to a pull-down transistor. All these double column pull-down transistors are connected together like it is done with the pixel signals in the single columns. The overall signal is then inverted again and connected to a pad of the chip. This overall chip HitOr signal is high if at least one pixel sees a hit and low otherwise.

2.2.3 Measuring the threshold of the discriminator

In order to gain information about the threshold the injection circuitry of the FE-I4 is used. The injection circuitry, which consists of two capacitances, C_{low} and C_{high}, allows for a charge injection from 0 to 140 ke, which corresponds to a range from 0 to 9.12 fC or up to three times the mean charge deposition of a mip. A simple method is to count the hits while injecting charges over the whole range. The result of such a measurement is the so called S-curve, as can be seen in figure
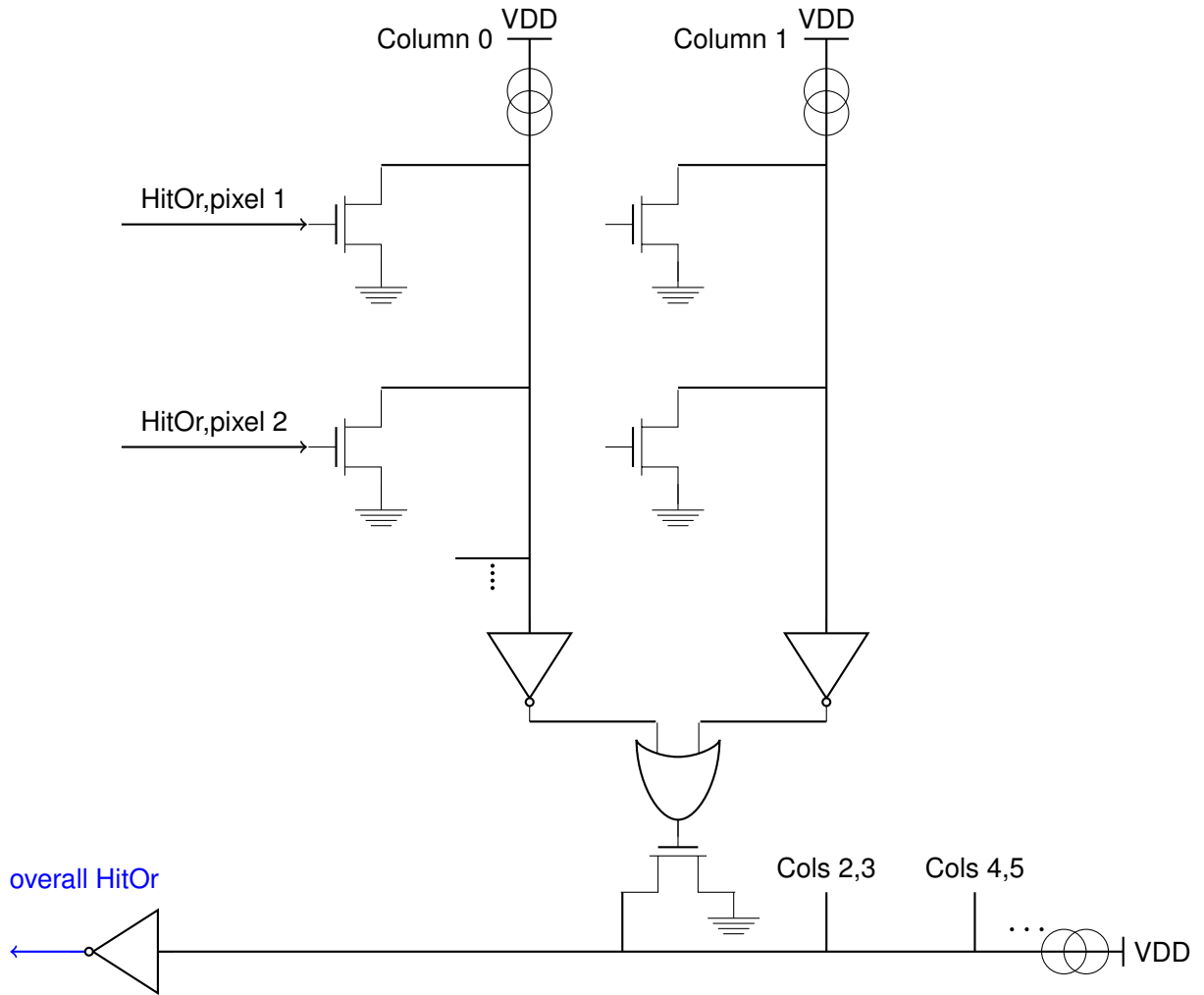
Figure 2.6: Schematic of creation of overall HitOr signal of FE-I4 chip. All pixels of one column are OR'ed together by pull-down transistors. The overall HitOr as a result is high if one of the pixels' discriminator is high and is low otherwise.

2.7. By injecting over a very wide range of charges one starts below the threshold and after a certain value above threshold. This should ideally result in no detected hit before the threshold and 100 % detected hits above the threshold, i.e. a step function. Due to noise in the electronics this is in reality not the case and the step function is being convoluted with a Gaussian function which then alters the detector response to follow a S-curve. The hit probability $p_{\text{hit}}(Q)$ in dependence of the injected charge Q can then be parametrized through formula 2.1.

$$p_{\text{hit}}(Q) \; = \; \Theta\left(Q - Q_{\text{thresh}}\right) \otimes \exp\left(-\frac{Q^2}{2\sigma_{\text{noise}}^2}\right) \; = \; \frac{1}{2}\text{erf}\left(\frac{Q - Q_{\text{thresh}}}{\sqrt{2}\sigma_{\text{noise}}}\right) \tag{2.1}$$
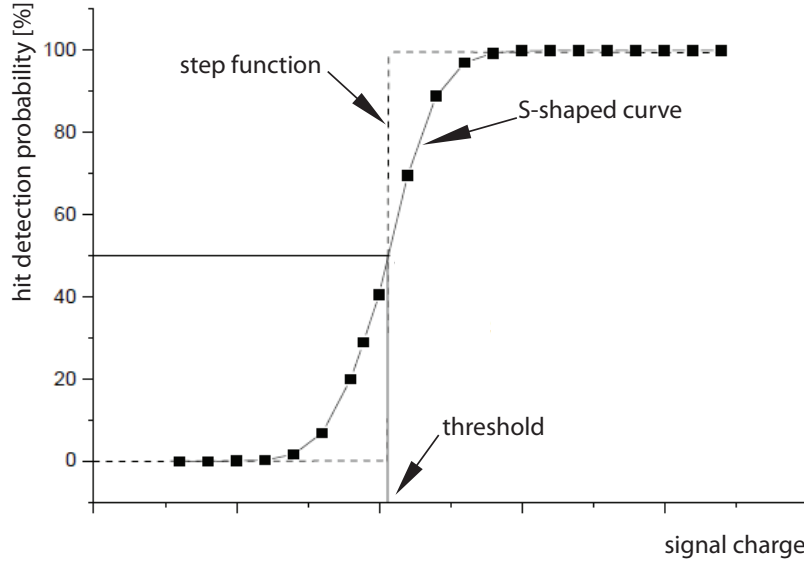
Figure 2.7: Hit detection probability as a function of the signal charge at the preamplifier input [11].

The 50 % hit mark of the S-curve defines the threshold of the discriminator Q_{thresh}, where the noise σ_{noise} is the determined by the width of the S-curve.

2.2.4 Calibration of the chip

The injected charge - a major input to the charge calibration - depends on the injection capacitances and on the voltage applied to them $Q_{\text{injected}} = C_{\text{injection}} \cdot \Delta V$. Due to production tolerances not every chip has the same injection capacitance and the exact value has to be determined experiment-ally. A value of $C_{\text{combined,measured}} = (6.7 \pm 0.67)$ fF, if both capacitances are used in parallel, was measured, see [21], as compared to the simulated value of $C_{\text{combined,simulated}} = 5.7$ fF. As the meas-urement was only done with one module so far and the measured value and the simulated value do not deviate too much, the simulated value will be used in the following. The voltage step ΔV, in the range from 0,..,1.2 V, that is needed for the injection is set by a Digital to Analog Converter (DAC). Therefore, the conversion factor between applied Voltage in mV into that one in Digits has to be determined. With these two values - injection capacitance and voltage to DAC-value conversion factor - a calibration of the chip can be done.

2.2.5 Tuning of the chip

In order to tune the settings of the discriminator threshold and the feedback current for all the pixels in a reasonable amount of time an automatic procedure is needed. Internally many DACs influence the threshold and the feedback current. The four most important ones are shown in figure 2.4. Locally the TDAC and the FDAC set the threshold and the feedback current in the pixel cell registers, respectively. Globally the GDAC and the IF-DAC fix both values coarsly for all pixels in the periphery. Several tuning algorithms are implemented in the software package `STControl`, that is used for operating the chip. Together with the `USBpix` readout system the whole DAQ of a chip can be done, see [10, 11, 17, 22].

The FE-I4 has been developed for the `IBL`, so a tuning close to the design values for the `IBL` operation is chosen also for the FE-I4 based modules used in this work in order to be in the linear region of all DACs. The threshold is tuned to be 3000 electrons and a response of 6 ToT corresponds to a charge at the input of 20 ke. After the proper tuning, the dispersion of the discriminator threshold over the whole chip of about 60 electrons is possible. Both tunings decrease the dispersion in threshold and ToT over all pixels. In figure 2.8 and 2.9 the threshold and ToT distributions before and after tuning are shown.

(a) Threshold distribution before tuning.

(b) Threshold distribution after tuning.
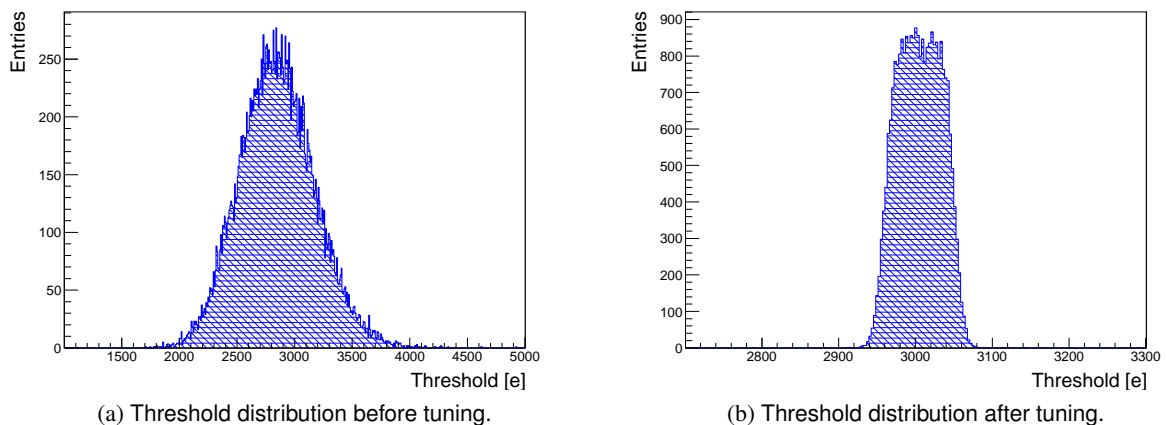
Figure 2.8: Threshold tuning. The dispersion before the tuning is in the order 400 e^-, while after a tuning it was found to be of the order 30 e^-, so basically all pixels have the same threshold which varies maximum 30 e from the target threshold value of in this example 3000 e^-.

(a) ToT distribution before tuning.

(b) ToT distribution after tuning.
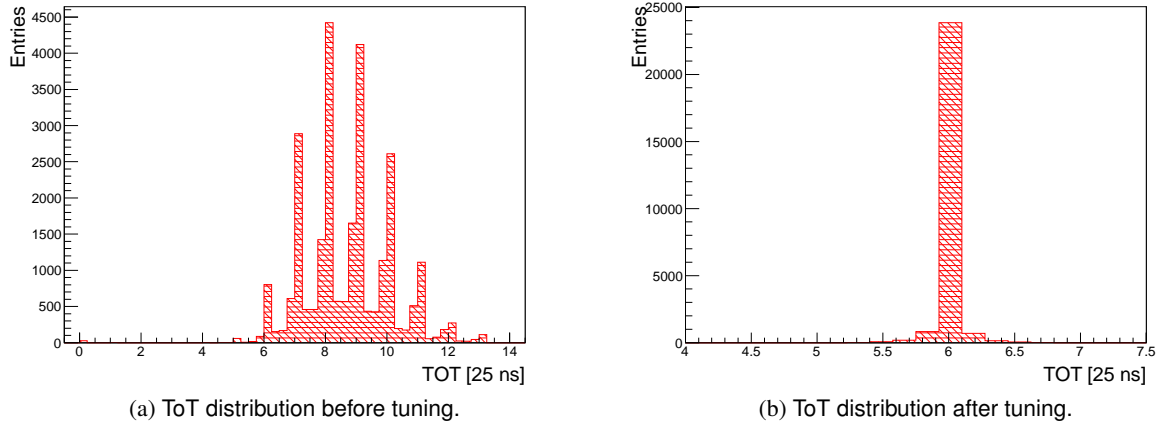
Figure 2.9: Time over threshold tuning. The dispersion before tuning is in the order of a few ToT while after tuning almost no dispersion is seen, so basically all pixels have the same ToT. The ToT is measured by injecting the same charge a hundred times and averaging over all values.

2.3 Basics of a beam telescope

A beam telescope is a detector system which is able to reconstruct the track of a particle going through with high precision of $\mathcal{O}(\mu m)$. By doing so, one can calculate the point where the particle passes through a device under test (DUT) and consequently measure and characterize its response. The reference planes are made out of well studied detectors. They are used to measure and reconstruct the hit positions which were created by the particle on its path and reconstruct the particles' trajectory (track).

As a triggering device, scintillators with photomultipliers in front and behind the whole assembly are often used because they deliver fast signals with rise times $\mathcal{O}(10\,\text{ns})$. An example for the setup of a general beam telescope is shown in figure 2.10. This setup of a telescope is however not very efficient if the dimensions of the DUT are much smaller than those of the trigger scintillators. Many tracks seen by the telescope and triggered by the scintillator are not passing through the smaller DUT.

One task of the `AIDA` project is to evaluate the possibilities of implementing a region of interest trigger by using a FE-I4 reference plane instead of one of the scintillators. By having a programmable region of interest the area on which the telescope is triggered can be chosen ad hoc. It can be chosen in a way that it matches the area covered by the DUT. This would make the data taking in a
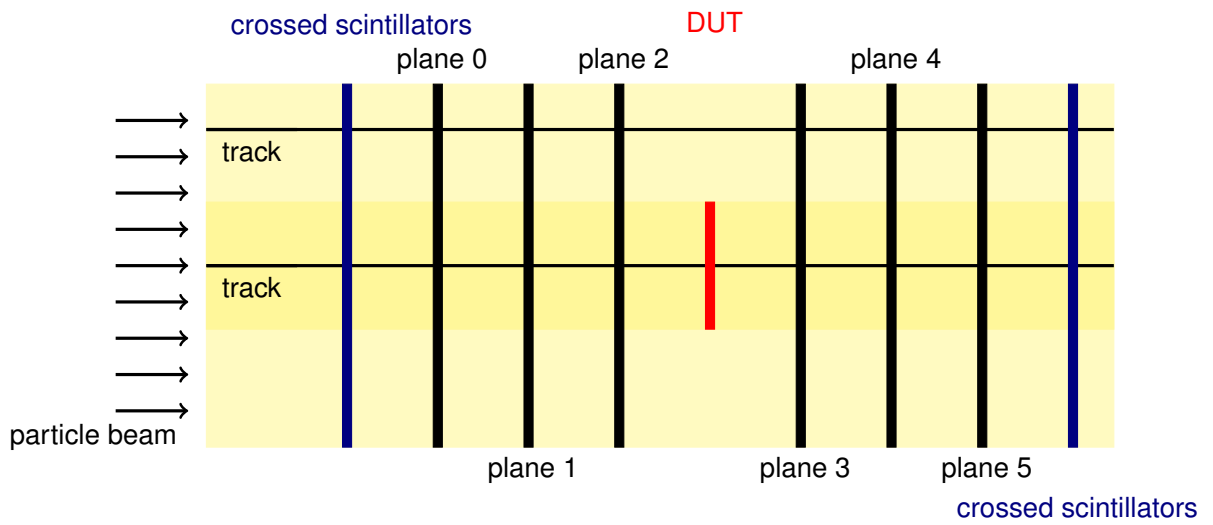
Figure 2.10: Usual setup of the EUDET-telescope with a DUT and scintillators as trigger generating devices.

test beam much more efficient.

One possible setup of a test beam telescope is with a FE-I4 reference plane instead of the two crossed scintillators behind the reference planes, see figure 2.11. This idea will be discussed in more detail in section 2.4.2.
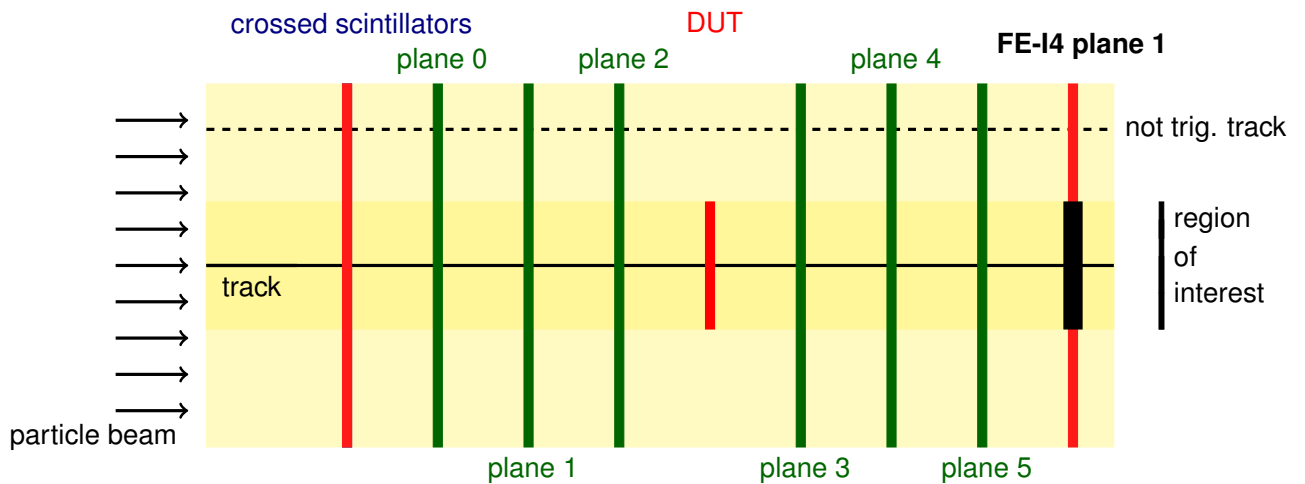
Figure 2.11: Setup of the EUDET-telescope with DUT and one FE-I4 plane as triggering device replacing the scintillators behind all reference planes. The track indicated by the dashed line will not be recorded.

2.3.1 Spatial resolution

The spatial resolution of a telescope contains the convolution of two elements. First, every plane has its own intrinsic spatial resolution which is determined mainly by the pixel pitch. If only binary readout is done, the resolution is given by $\sigma_{x,y,binary} = d_{x,y}/\sqrt{12}$, where $d_{x,y}$ is the pitch. The z-direction is defined as the direction of the beam axis. In the case of analog readout the resolution is empirically given by $\sigma_{x,y,analog} = d_{x,y}/\left(\sqrt{12} \cdot SNR\right)$.

Second, the spatial resolution of the complete telescope at the position of the DUT depends on the distance of the reference planes to each other and to the DUT and on the number of reference planes. Studies show that the optimal setup is not uniquely defined, see [23]. The results of this study are that six planes always give a better position resolution than four planes and that the resolution depends on the minimum reference plane to DUT distance as well as on the DUT thickness. Further, the spatial resolution is strongly influenced by multiple scattering effects and therefore by the thickness of the planes in terms of radiation length X_0 and the energy of the particle beam. The mean scattering angle θ_{rms} can be calculated by formula 1.3. A total thickness of silicon of 500 μm and the same for the aluminum support plate of the module is considered here. The multiple scattering angle with respect to the beam direction and the resulting extrapolation error at the next plane - after 2 cm of air - are given in table 2.1 for the relevant energies studied in this document.

The decrease in spatial resolution due to multiple scattering can be estimated from the extrapolated errors from one plane to the next plane. It is clear that - concerning spatial resolution - the conditions at the ELSA accelerator are not ideal. Nevertheless, for testing purposes the available energies are sufficient for the particles to pass through four planes.

accelerator	energy	multiple scattering angle [mrad]	extrapolated error [μ m]
	104 MeV	10	210
ELSA	338 MeV	3.2	65
	416 MeV	2.8	57
DESY	6 GeV	0.19	4
CERN	120 GeV	0.01	0.19

Table 2.1: Multiple scattering angle and extrapolated error for the different setups studied here.

2.3.2 Rate capability

As a beam telescope is used to determine properties such as spatial resolution and efficiency of an unknown detector, a large number of tracks needs to be measured. The data taking rate plays an important role since it is directly related to the measurement time. Currently rates of 4 kHz can be achieved with the EUDET-telescope. The limiting factor is the readout time necessary to get the data from one trigger which is about 230 μs needed to read two full frames. In general, many factors influence the rate:

- The time interval between a trigger arriving at the trigger logic unit (TLU) [24] and the issueing of the trigger signal to all attached detectors. In the case of the EUDET telescope this interval, the trigger latency, is (27 ± 3) ns [24].

- The time needed to acquire the data from all detectors. In the case of a telescope, the slowest device limits the rate. Further the DAQ of different detectors can have very different timing schemes, which influences the rate as well.

- The time needed to combine the data from all detectors to a common datastream. The limiting factor here is the PC on which this is done. If a combination needs to be done the only mode currently supporting this is the `Trigger Data Handshake` mode. It attaches a unique trigger number into the data stream of all detectors, while vetoing new triggers in the meantime.

All these different factors take time while in the end the slowest step is responsible for the overall rate capability.

2.4 Triggering scheme

Triggering signals are a key ingredient to any detector system. They define at which time an interesting event happened and start the data acquisition. Therefore the most important requirements on a triggering signal is that it should be fast and reliable.

2.4.1 Trigger logic unit

Once the signal of a triggering device is converted into a logic signal it can be further processed to create for instance a coincidence. With the TLU, developed in the EUDET-framework, such a coincidence and even more complicated combinations of the incoming signals can be formed by changing its configuration. This trigger logic unit has four trigger inputs, which can be seen in the upper right corner of figure 2.12, where the front of the TLU is shown [24]. The four lemo inputs can internally be put together through a logic AND, OR or Veto. The device which is first in the beam goes to Ch0 and the others follow accordingly.
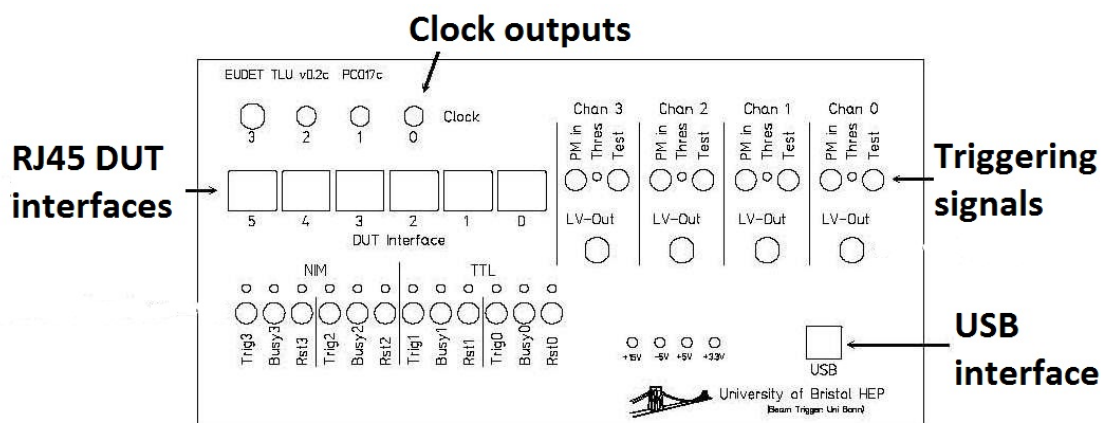
Figure 2.12: Front view of trigger logic unit. The triggering signals are connected to Ch3, Ch2, Ch1 and Ch0. In total up to six DUTs can be triggered using the RJ45 interfaces [24].

As mentioned above a telescope can be triggered for example by a scintillator signal. The primary signal of a scintillator gets amplified by a photomultiplier and results in a sharp peak of typically 20 ns duration. The EUDET telescope uses the coincidence of four scintillators, two in front and two behind, for triggering.

2.4.2 Implementation of FE-I4 region of interest trigger into EUDAQ

The possible setup of a telescope with a region of interest trigger implemented through the usage of FE-I4 reference planes is depicted in figure 2.11. By choosing a sensitive trigger region with the FE-I4, tracks that do not pass through the DUT can be excluded from the DAQ. At the same time the whole FE-I4 pixel matrix can be read. In the following, the necessary information to integrate

the triggering signal of the FE-I4 readout chip into the triggering scheme of EUDAQ will be given. As a triggering signal the HitOr of the whole FE-I4 will be used. In order to connect the HitOr
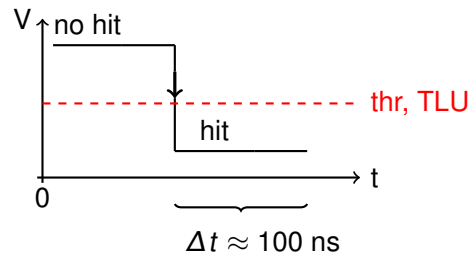
Figure 2.13: HitOr signal discrimination through TLU input. The TLU triggers on the falling edge of the HitOr signal.

signal to the TLU it has to be inverted again, because the TLU has been specifically designed to trigger on the falling edge of the input signal. The signal is discriminated by a tunable threshold of a comparator. A sketch of the HitOr signal acting as an input to the TLU is shown in figure 2.13 and a schematic of the TLU triggering inputs in figure 2.14, where the range of the input signal threshold can be set between -800 mV and 800 mV. Once the signal at the input is smaller than the threshold, a triggering signal will be processed by the TLU and the DAQ starts.
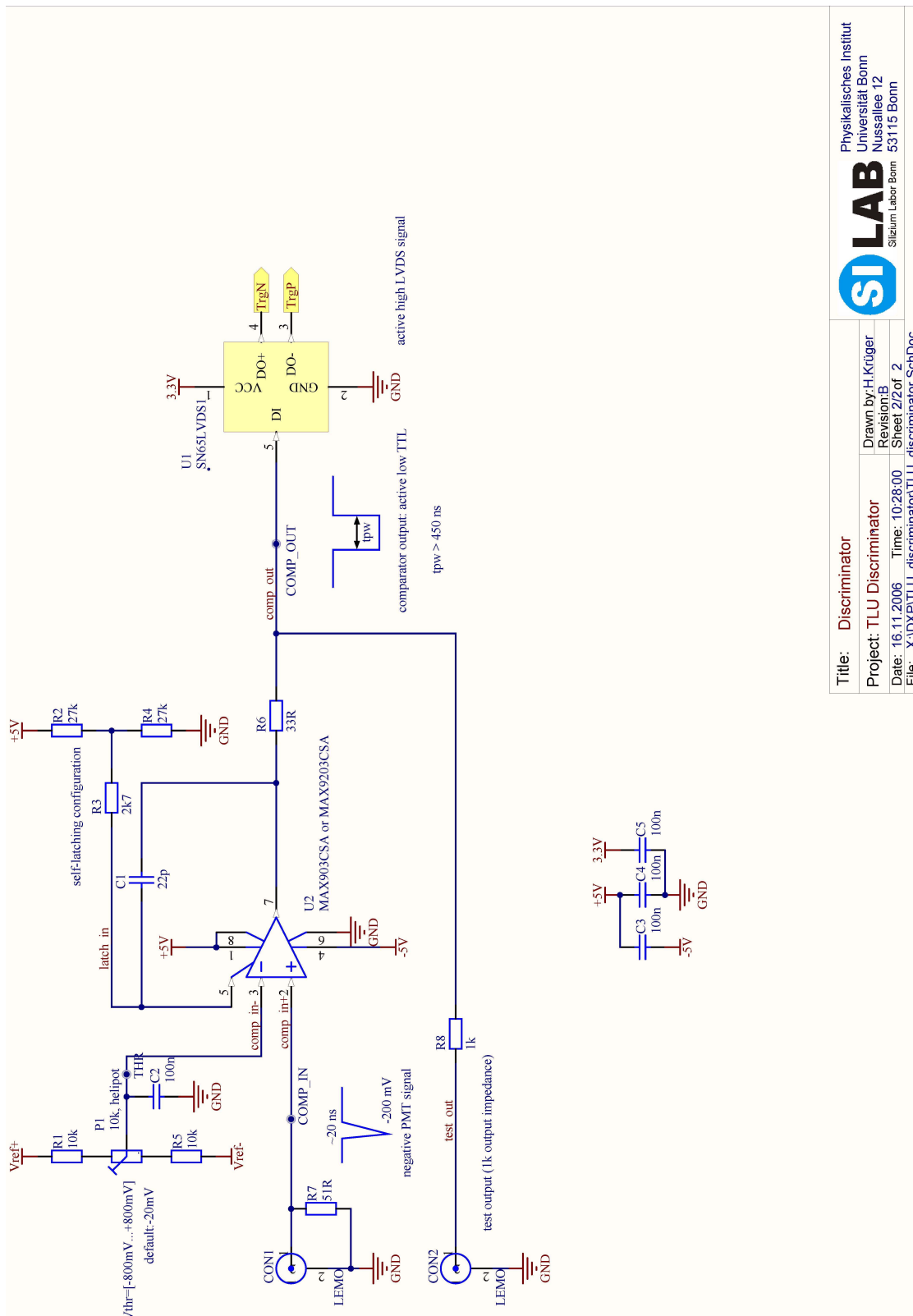
Figure 2.14: Discriminator board for trigger inputs of the TLU. The input has to be connected to CON1, from there the signal acts as input to a comparator with tunable threshold. The output of this comparator can be monitored from CON2. The length of this signal depends on the capacitance C1 and the resistances R2, R3 and R4. A typical length is 500 ns [24].

Chapter 3

Telescope measurements

Telescope measurements with a setup similar to the one described before but with reference planes using FE-I4 readout chip based pixel modules have been performed on the accelerator ELSA in Bonn and on the Super Proton Synchrotron (SPS) at CERN in Geneva. From now on such a telescope is referred to as a FE-I4 beam telescope. A specific test beam line in Bonn has been prepared for this work and therefore will be explained in more detail on the text. In addition, as the testing of the data acquisition of the FE-I4 beam telescope is one major part of this thesis it will be explained here.

3.1 Data acquisition with the FE-I4 beam telescope

To read out the FE-I4 chip based modules the laboratory testing platform USBpix (figure 3.1) is used [10]. The system hardware is based on a multi-purpose FPGA card, the S3MultiIO-board, and a dedicated adapter card. The FE-I4 based module is mounted on a single chip card (SCC) and connected to the mentioned adapter card through ethernet. The data, the trigger and the configuration commands go over this connection. The powering of the chip is done separately using bench power supplies with sense wires. The USBpix system is connected to the DAQ PC via USB. The software package STControl is used to control the whole DAQ. More detailed information about the USBpix system can be found in [11, 22].

The data acquisition of the FE-I4 beam telescope makes use of the EUDAQ framework. One key part of this DAQ is the trigger generation. EUDAQ uses a TLU specifically designed for the EUDET
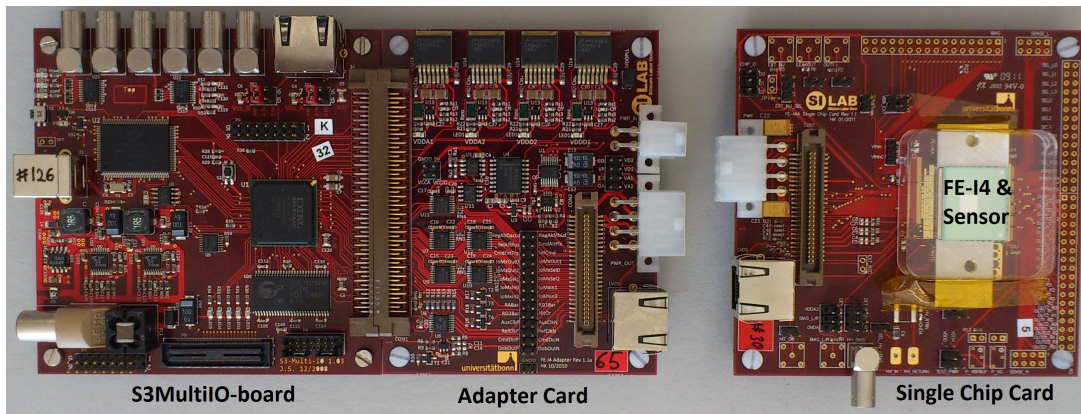
Figure 3.1: USBpix system consisting of S3MultiIO-board connected to FE-I4-adapter card. The FE-I4 together with the sensor is glued on the SCC.

telescope to generate and to issue the trigger signal to the detectors. Fulfilling the requirements of the FE-I4 beam telescope concerning triggering that TLU will be used. In figure 3.3a the whole DAQ chain and trigger generation and distribution is depicted.

In order to reconstruct the data taken with the FE-I4 beam telescope it is crucial to be able to combine the data of all detectors with the same trigger number in the correct way. For this purpose a unique number, the trigger number, is assigned in an univocal way to every trigger and included into the data of each single detector for further event reconstruction. The trigger number is generated by the TLU. While receiving the trigger signal, the detectors busy line is set to high, the trigger number is clocked out, the data+trigger number is send to the corresponding DAQ and the busy line is put to low again, see figure 3.2. After that the detector is free to accept a new trigger. In that way an online and offline synchronisation of the whole dataset can be done. The triggering scheme which realizes the above described method is called the `Trigger Data Handshake` and is used here.
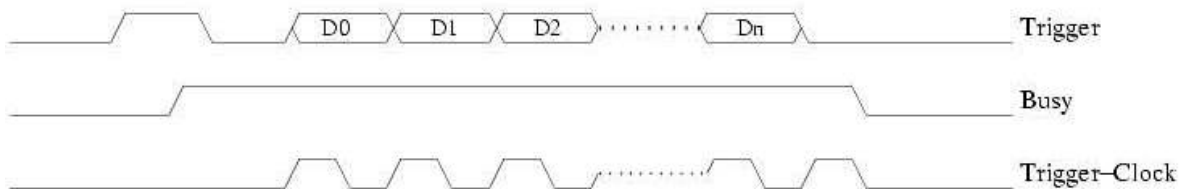
Figure 3.2: Sequence of TLU trigger mode `Trigger Data Handshake` [24].

In order to operate the FE-I4 based modules within `EUDAQ`, an integration of the `USBpix`-system into this framework was done, see [17, 22]. The scheme of the DAQ with `EUDAQ` is based on producers

that communicate to each other using TCP-IP protocol, see figure 3.3b. Detectors, that means reference planes as well as DUTs, are treated by the software in the same way. Consequently DUTs and reference planes are exchangeable in `EUDAQ`. Each detectors' producer sends its data
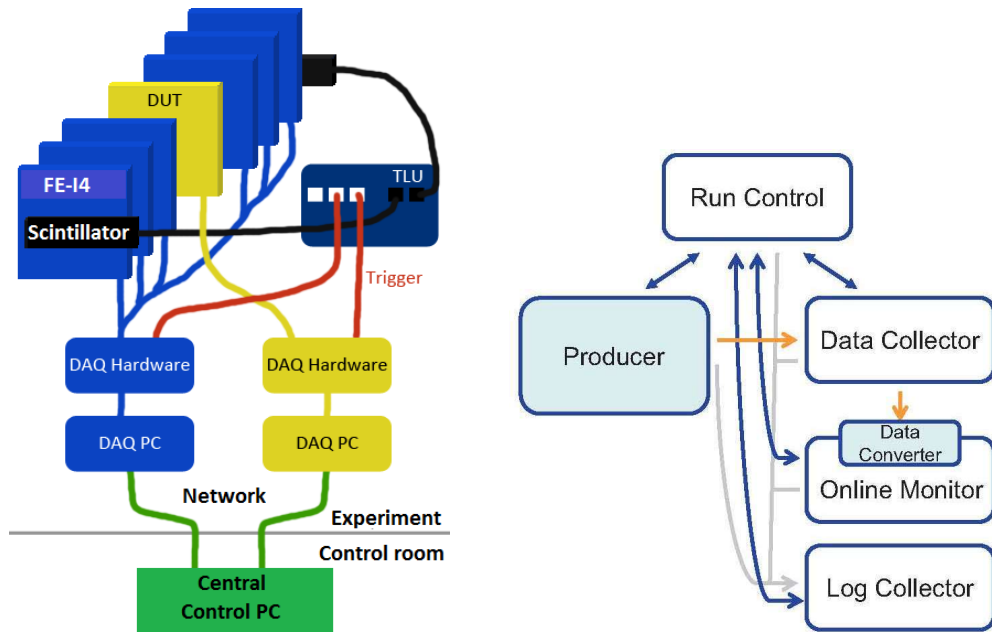
(a) DAQ scheme of FE-I4 telescope. The scheme mimics the `EUDET` telescope, just the reference planes are not `MIMOSA26` - Minimum Ionizing MOS Active Pixel Sensor as used by the `EUDET` telescope - but FE-I4 instead.

(b) Components of the `EUDAQ` framework and structure of the network communication. In blue commands and status updates, in orange data and in gray log messages are shown [17].

Figure 3.3: Hardware and software setup of FE-I4 telescope

- containing the trigger number - to the producer `Data Collector`, that combines all the data to form the telescope data. The producer `Run Control` configures all detectors and starts and stops the DAQ. Every producer sends status messages to the `Run Control` producer. Log messages are send to the producer `Log Collector`. Two data taking computers are needed to operate the telescope system. One is running the software `STControl` which is used to take the data from the FE-I4 based reference planes and the second is running the data acquisition software package `EUDAQ` and all its producers. It receives the data from the TLU and the `STControl`-PC, and combines it together to write and store the telescope data.

For testing the general functionality of the FE-I4 beam telescope all the following measurements do not include a DUT.

3.2 Setup of the telescope at the `ELSA` accelerator complex in Bonn

The main ring of the accelerator complex in Bonn, called `ELSA`, can accelerate electrons up to energies of 3.2 GeV [25]. A beam with such an energy is extracted and guided to one of the two hadron physics experiments. The setup for the FE-I4 beam telescope is placed behind the tagging system of the `Crystal Barrel` (CB) experiment [26]. Such a system is used to determine the energy of bremsstrahlung electrons by deflecting them with a magnetic field and detecting them with scintillators. By doing so one assigns an energy label to each electron and therefore calls this method tagging.

Being placed behind the tagging system, the FE-I4 telescope has access to the above mentioned bremsstrahlung electrons. In figure 3.4 one can see a schematic of the tagging system as well as the position of the telescope. In order to reduce the effect that multiple scattering has on the extrapolation error of the reconstructed track, the highest possible energy is favoured, therefore a position close to the photon beam axis is preferred. Due to mechanical constraints, the position shown behind slab number 35, is the one with the highest energy reachable, 413 MeV.

This setup of the telescope is sufficient for the commissioning of the FE-I4 telescope with full DAQ.
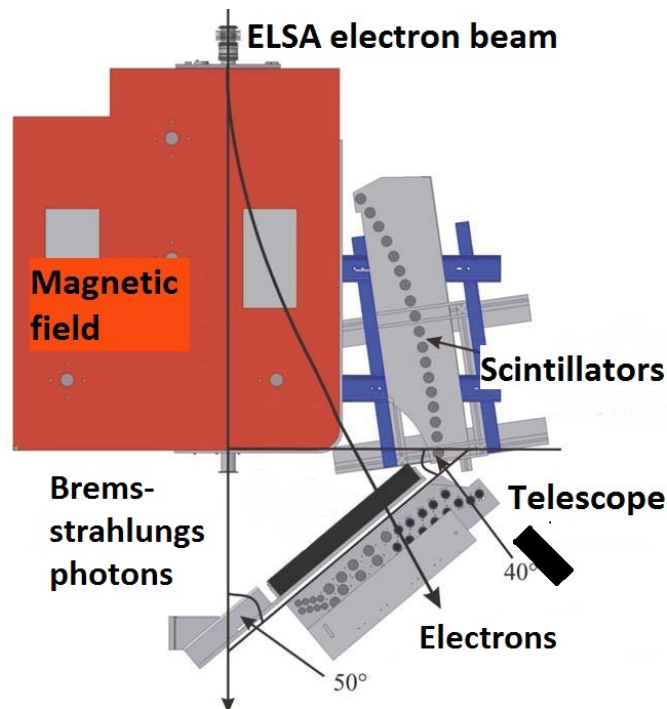
Figure 3.4: Place of FE-I4 telescope close to tagging system of CB.

3.2.1 Beam conditions

One fundamental requirement for telescope operation in a beam is that the energy of the beam particles is high enough in order for the particles to be able to pass through all planes. Further, the effect of multiple scattering increases with decreasing energy and this will have an effect on the telescopes pointing resolution as will be described later. The available beam energy at the chosen setup depends on many parameters and therefore is explained in more detail in the following. Also, the rate of the beam is of importance as it affects the measurement time. For reasons that will become clear in the following the rate and the energy of the beam are correlated for this setup.

The rate of electrons reaching the telescope can be determined by the rate of the extracted ELSA beam. This beam with energy E_0 hits first a copper radiator. The electrons pass the radiator and some emit a bremsstrahlungs photon. These electrons get deflected by a magnetic field and pass through the tagging scintillators before reaching the telescope. The probability of this process to occur and have an electron with an energy in the interval $[E_{e,min}; E_{e,max}]$ can be calculated with the formula 3.4:

$$\frac{N_e}{N_0} = \frac{d}{X_0} \left[0.75 \ln \frac{E_0 - E_{e,min}}{E_0 - E_{e,max}} - \frac{E_{e,max} - E_{e,min}}{3E_0} + \frac{(E_{e,max} - E_{e,min})^2}{2E_0^2} \right] \tag{3.1}$$

where N_0 is the number of incoming particles, N_e the number of electrons that emit a bremsstrahlungs photon, E_0 the energy of the incoming particles, d the thickness and X_0 the radiation length of the radiator. This probability is given for the different copper thicknesses used in the experiment in table 3.1. The calculation is done for the energy range of the electrons reaching the telescope position,

Thickness d [μ m]	N_e/N_0 [%] 412 MeV $<$ E_e $<$ 435 MeV	N_e/N_0 [%] 127 MeV $<$ E_e $<$ 2985 MeV
15	0.0016	0.2
50	0.00053	0.8
150	0.0016	2.4
300	0.0032	4.8

Table 3.1: Probability of having an electron emit a bremsstrahlungs photon resulting in a certain energy range normalized to the incoming number of electrons. The radiator, made in copper with different thicknesses, is assumed to have an X_0 of 14.3 mm.

as well as for the whole low electron energy range, because this rate is measured during a run and is therefore useful as a control value. No correction is done here for the whole angular region because the angular spread of the outgoing electron beam is very small [27]. The energy range of 412 MeV to 435 MeV electrons is taken from a conversion factor measured by the CB collaboration, see table 3.2. The energy scaling factor between the energy of the ELSA beam E_0 and the energy of the electrons measured at scintillator number 35 is 0.13. The expected rate on scintillator 35 is found to be 30 kHz.

Scintillator number	30	31	32	33	34	35	36	37
Energy conversion factor	0.114	0.117	0.121	0.125	0.129	0.130	0.133	0.137

Table 3.2: Conversion factors of CB tagger. The values are understood to correspond to the energy in the middle of each scintillator. Only the fraction of scintillators which are closest to the telescope are shown here.

3.2.2 Threshold setting and noise occupancy

The threshold setting of a telescope plane is directly related to the signal strength and noise hit rate, as higher thresholds cut out more signal and lower thresholds result in an increased noise hit rate. As the amplitude distribution of noise is Gaussian around zero, some noise pulses can cross the threshold. The noise hit rate however depends strongly on the threshold setting, see figure 3.5. When lowering the threshold it is clear that the number of hits due to noise fluctuations increases [14].

(a) Noise fluctuations around baseline.

(b) Setting of the threshold in a threshold discriminator system.
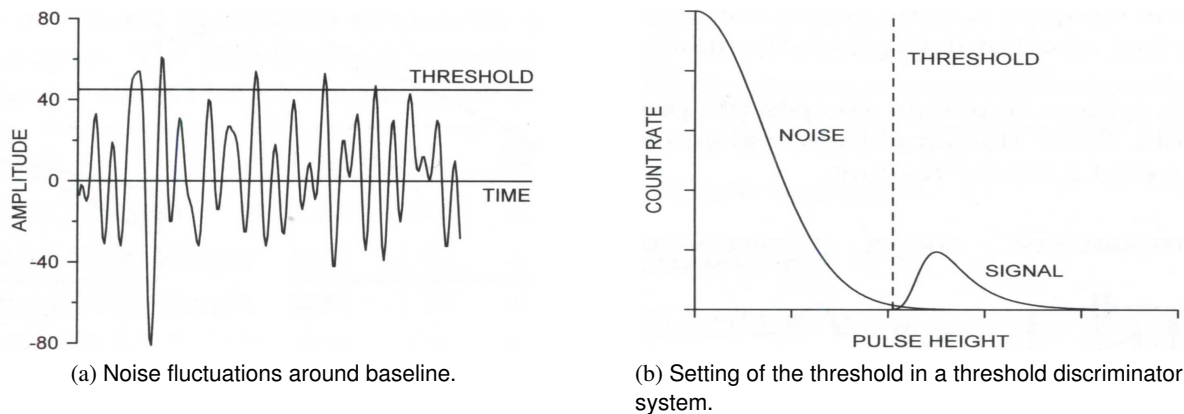
Figure 3.5: Noise pulses will exceed an amplitude threshold with a rate dependent on the threshold setting [14].

In order to find the lowest threshold with an acceptable noise hit rate, the fluctuations of the signal Δ_{Landau}, the distribution of the threshold σ_{thr} and the mean noise value itself ENC need to be considered as they all contribute to the effective noise σ_{eff}, see figure 3.5b. An acceptable noise hit rate in terms of efficient tracking requires the threshold to be five times higher than the effective noise [14]:

$$\sigma_{\text{eff}} = \sqrt{\Delta_{\text{Landau}}^2 + \sigma_{\text{thresh}}^2 + ENC^2} \; ; \quad Q_{\text{thr}} > 5 \cdot \sigma_{\text{eff}} \tag{3.2}$$

.

Signal fluctuation $\Delta_{\textbf{Landau}}$ The most probable value for the signal of a mip from a $200\,\mu$m thick silicon sensor is $16\,$ke ($\approx 80\; e^- h^+$-pairs per μm). The fluctuation of this signal follows a Landau-distribution, as is shown in chapter 1.1.1.

Threshold dispersion $\sigma_{\textbf{thresh}}$ The threshold dispersion over the FE-I4 after a tuning can be reduced to $30\,e^-$ for a threshold of $3000\,e^-$, see chapter 2.2.5. That means that for a tuned readout chip the threshold of $68\,\%$ of all pixels lies between $2985\,e^-$ and $3015\,e^-$. A few pixels, however, have a very low threshold and will therefore increase the rate of noise hits. Like this, the threshold dispersion contributes to the effective noise. The smaller the threshold dispersion, the lower is the probability to find pixels with very low thresholds.

Noise mean ENC   The electronics noise can be measured with the S-curve method described in section 2.2.3. With a FE-I4 based module at IBL operation point an average noise value of about $157\,e^-$ is measured, assuming the simulated values of the injection capacitances mentioned in chapter 2.2.4. The dispersion over the whole chip after tuning is $7\,e^-$, see figure 3.6.

Measuring the noise occupancy   In a readout chip as the FE-I4, where the state of the discriminator is sampled with the bunch crossing frequency $f_{\text{sample}} = f_{\text{bunch}} = 40\,$MHz, the number of recorded noise hits is measured in terms of this frequency and the sampling interval Δt. Then the time fraction that the system is open for noise hits is given by $f_{\text{sample}} \cdot \Delta t$. The according noise rate is given by $f_{\text{sample}} \cdot \Delta t \cdot f_{\text{noise}}$ with f_{noise} being the noise rate for the given threshold. The probobility
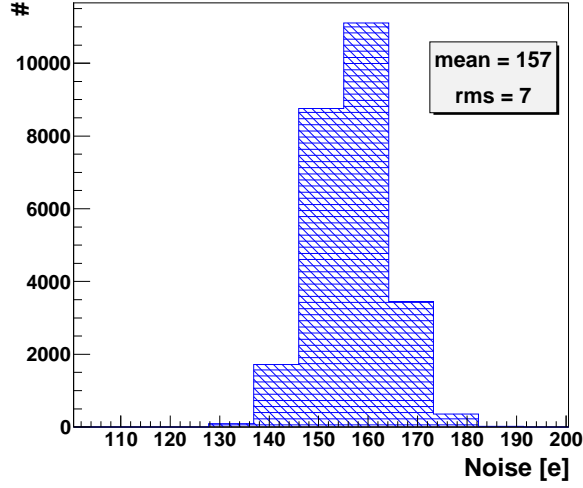
Figure 3.6: Noise distribution of a 200 μm thick sensor with FE-I4 readout.

for noise hits to occur - the noise occupancy - is given by

$$P_{\text{noise}} = \Delta t \cdot f_{\text{noise}} \tag{3.3}$$

So as to understand the behaviour of the noise occupancy better, it is measured in dependence of the threshold for a FE-I4 based reference plane. The noise occupancy is measured by sending N arbitrary triggers at a sampling frequency of 40 MHz and can be calculated by:

$$P_{\text{noise}}/\Delta t = f_{\text{noise}} = \frac{\text{number of hits}}{N \cdot 25\,\text{ns} \cdot 40\,\text{MHz}} = \frac{\text{number of hits}}{\text{number of triggers}}. \tag{3.4}$$

It happens that after sending more than a 10^9 triggers no hit is measured. In this case one artificially assigns one hit to such a pixel. Therefore only a limit on the noise occupancy can be defined, then $P_{\text{noise}}/\Delta t < 10^{-9}/\text{25ns}$. In figure 3.7 one can see the noise occupancy of a planar silicon sensor 200 μm thick with FE-I4 readout for different thresholds. From threshold 3000 e$^-$ to 900 e$^-$ the noise occupancy is below $10^{-9}/\text{25ns}$. As in this measurement 10^9 triggers are sent this means that most of the pixels have measured no hit. Only at a threshold of 800 e$^-$ some pixels start to measure hits and the noise occupancy rises to approximately $5 \cdot 10^{-8}/\text{25ns}$.

Taking into account the measurement of the noise occupancy, the above mentioned requirements of an efficient tracking and the design operation point of the FE-I4, a threshold of 3000 e$^-$ is chosen
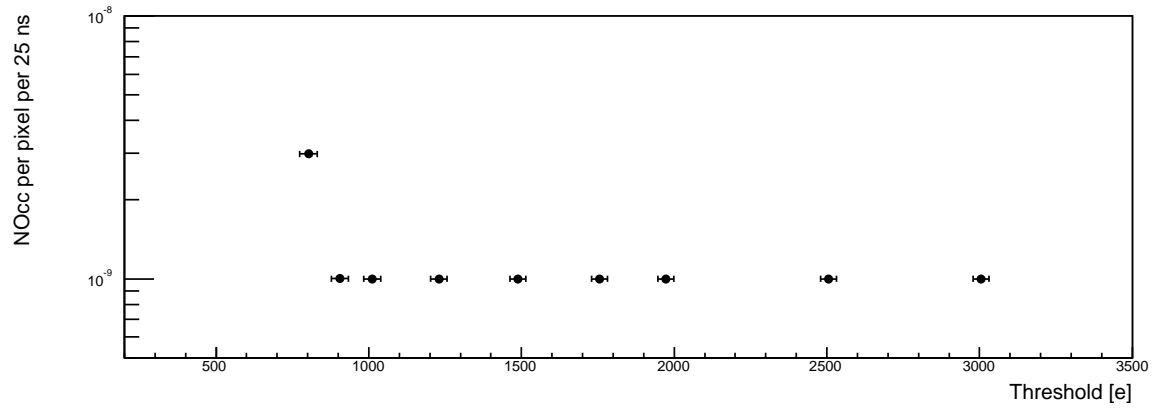
Figure 3.7: Noise occupancy of a 200 μm thick sensor with FE-I4 readout measured for different threshold settings.

for the operation of the FE-I4 beam telescope.

3.2.3 Bias voltage setting of the telescope

To reduce the electronics noise as much as possible and for having all the volume active while telescope operation the full depletion of the reference planes is required. Therefore the proper bias voltage $U_{bias} > U_{full\ depletion}$ is desired for the telescope reference planes. In order to determine the full depletion voltage $U_{full\ depletion}$ of the sensors a measurement of the noise against the bias voltage U_{bias} can be used as it gives information about the development of the depletion zone inside the sensor. The noise of the sensors is directly correlated to the capacitance of the depletion region and thus varies inversely with the width of the depletion zone. While the depletion zone grows, the capacitance of the sensor decreases. Consequently the noise decreases as well, until a saturation sets in when the sensor is fully depleted. The described behaviour can be seen in figure 3.8 where the noise against the bias voltage is plotted for all telescope reference planes. At lower voltages the noise is rather high whereas it falls and saturates at voltages around 40 V. From figure 3.8 it follows that the sensors are fully depleted for bias voltages $U_{bias} > 40$ V. Assuming a factor two for safety for the depletion a bias voltage of 80 V is chosen.
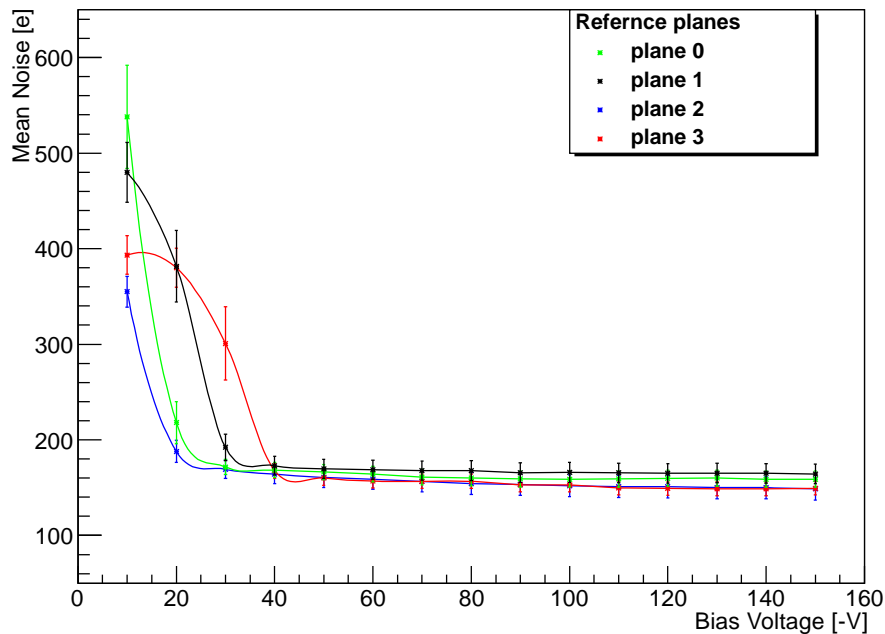
Figure 3.8: Noise measured against bias voltage.

3.3 Telescope results from operation at ELSA

Two types of telescope measurements were done at ELSA. The first measurement is with a setup of two planes and an ELSA energy of 800 MeV (104 MeV at the position of the telescope) and the second is carried out with four planes and the maximum energy of 3200 MeV (416 MeV at the position of the telescope). In both cases the trigger signal is the coincidence of two scintillators covering the area delimited by the FE-I4, one in front and one in the back of the telescope planes.

3.3.1 Test of two planes with 104 MeV e^- at ELSA

With the setup described above, and shown in figure 3.9 schematically, data was taken with electrons of 104 MeV reaching the telescope. At such low energy the distortion of the electrons due to multiple scattering plays a significant role. A calculation yields a multiple scattering angle of $\theta_{\text{rms}} = 10$ mrad. The extrapolated shift from one plane to the other in x- or y- direction is 210 μm for an inter plane distance of 2 cm in air. That means that on average a particle is scattered from one plane to the next by one pixel in the x-direction and four pixels in the y-direction. Such big shifts would have a significant influence on the later data analysis and this configuration is just meant to be used for the first sanity checks.
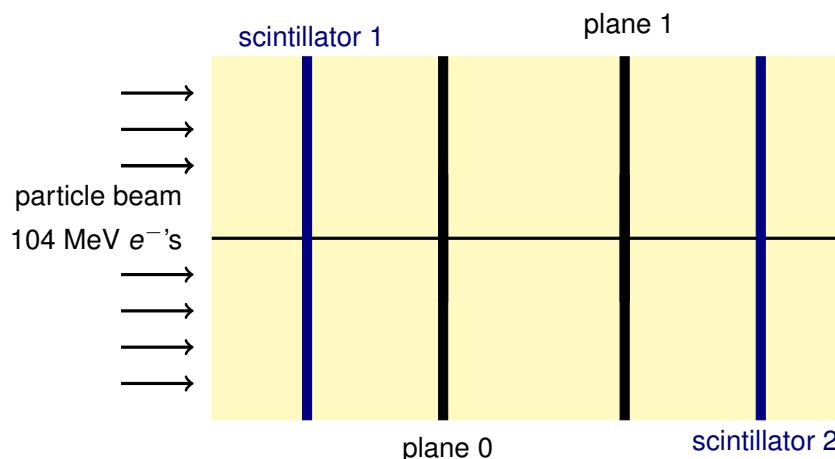
Figure 3.9: Telescope setup with two FE-I4 one-chip assemblies

The hitmaps of both planes show all hit entries in a plot where the pixels are assigned relative to each other like on the real chip but not to scale, see figure 3.10a and 3.10b. The left two columns

do not show any entries since they have been masked in order to avoid noisy pixels which are observed predominantly at the edges. From the homogeneous distribution of the hits it can be followed that the telescope is well centered in the beam.

(a) Hitmap plane 0

(b) Hitmap plane 1

(c) X Correlation between plane 0 and plane 1

(d) Y Correlation between plane 0 and plane 1
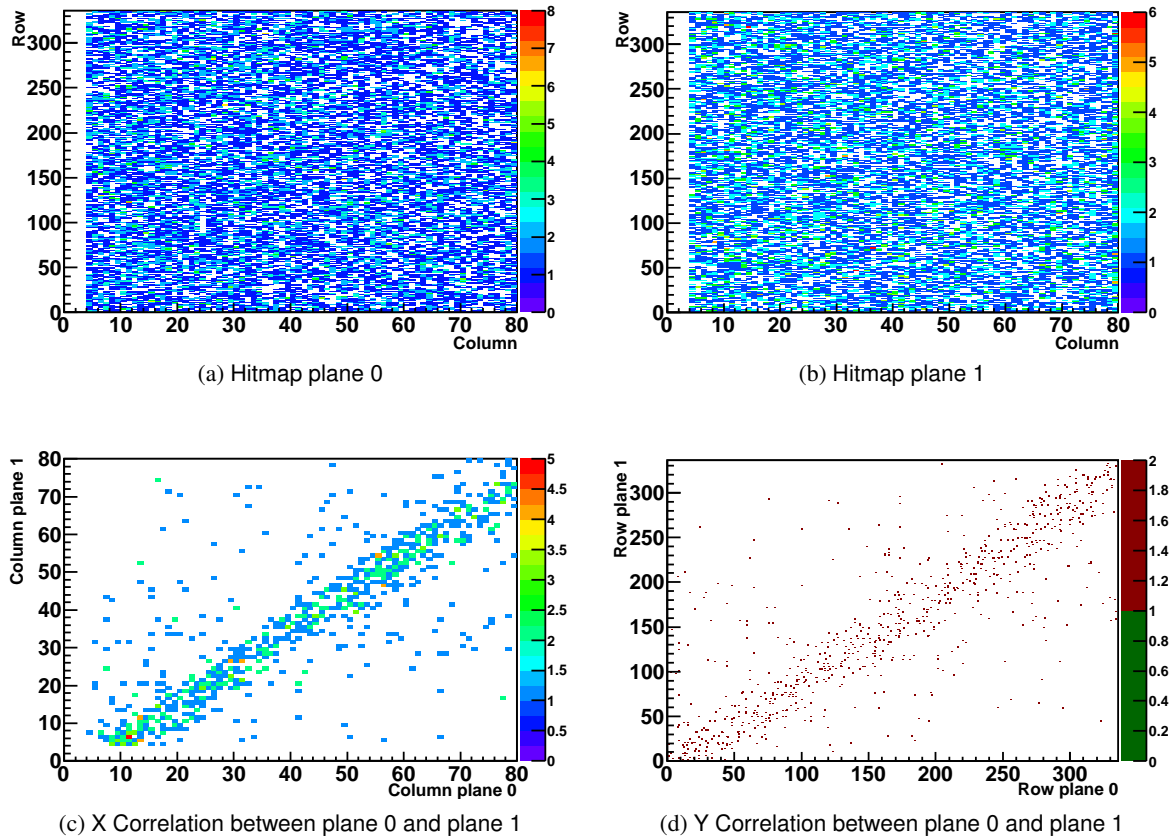
Figure 3.10: Hitmaps and correlation plots of two plane telescope setup with e^- of 112 MeV. The hitmaps show a homogeneous distribution of all hits. A dispersion appears around the diagonal in the correlation plots.

While operating the telescope, correlation plots of successive planes are a useful tool for checking the data acquisition. These plots reveal the relation between the x and y-coordinates of both planes. Particles that pass through the telescope undeflected create hits in the same coordinates on both planes for perfectly aligned planes. This would result in entries only at the same coordinates in the correlation plot and therefore a diagonal line through the origin.

In both correlation plots, shown in figure 3.10c for the x-axis (250 μm pitch) and 3.10d for the y-axis (50 μm pitch), a diagonal is visible. Two deviations from the ideal case become apparent. First, the diagonal has a certain width. This is an expected effect, because due to multiple scattering the

particles get deflected while passing the telescope. It can be estimated from the extrapolated shift, which is in this case $210\,\mu$m from the first plane to the second. As the statistics is very low the width of the diagonal is roughly estimated to extend over ten pixels in the x-direction and fifty pixels in the y-direction, resulting in a width of 2.5 mm for both directions. Second, the diagonal does not go through the origin. This feature is expected if planes are not perfectly aligned to each other. In that case, the coordinates of successive planes are still correlated but the coordinates in one plane are always shifted by the same amount relative to the other coordinates of the other plane. Nevertheless, the shift of the diagonal can be corrected by an offline alignment of the planes. For

(a) Correlation plot of a 10 mm long sensor with a finite pitch of 1 mm, perfect alignment, no scattering, no noise.

(b) Correlation plot of a 10 mm long sensor with a finite pitch, not aligned, no scattering and no noise.

(c) Correlation plot of a 10 mm long sensor with a finite pitch, not aligned, scattering (green) and noise (turquoise).
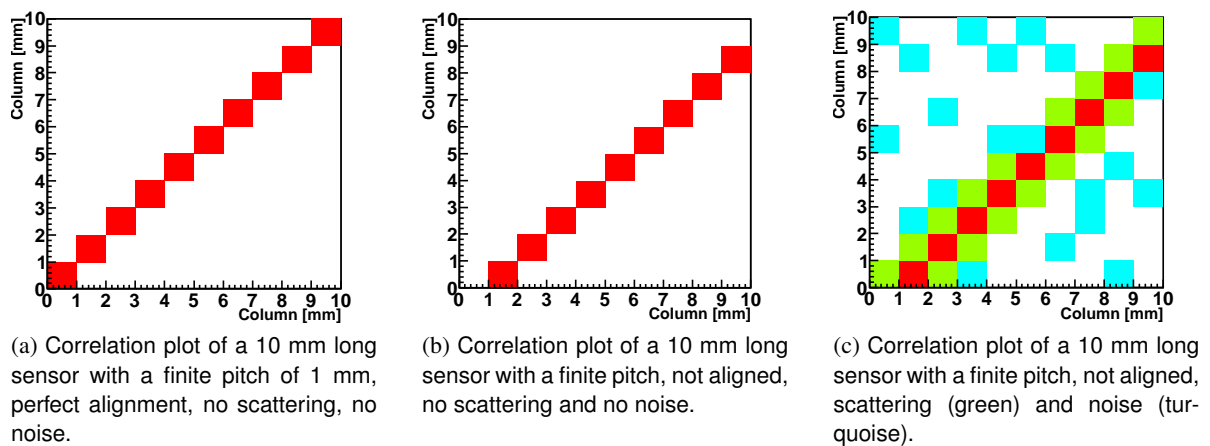
Figure 3.11: Effects of misaligned planes, multiple scattering and noise on the correlation plots of telescope planes.

complementarity, the expected features of the correlation plots as discussed for figures 3.10c and 3.10d can be seen individually in figure 3.11. Here, the influence the shift due to misalignment and the effects of multiple scattering and noise are depicted for a fictive sensor.

The diagonals of the correlation plots of the measurement (figures 3.10c and 3.10d) reveal the synchronous data acquisition of the telescope. For each trigger that is generated by the TLU and send to the both planes, the producer `Data Collector`, that combines the data, receives data sets from both planes that have the correct trigger number and system number attached, see figure 3.12. The `Trigger Data Handshake` mode is fully functional.
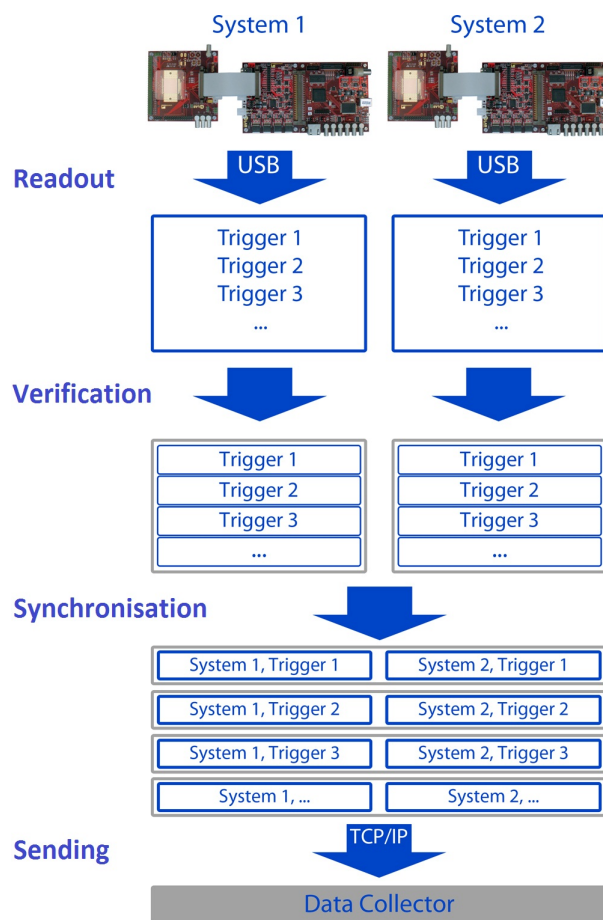
Figure 3.12: Data synchronisation and merging of two FE-I4 readout systems `USBpix` [17].

3.3.2 **Test of four planes with** $416\,\text{MeV}$ e^- **at ELSA**

Once the full functionality of the mechanical setup and DAQ with two planes has been reached, the natural continuation is the addition of two extra telescope planes. With such a setup, consisting of four planes, measurements with electron energies of approximately $416\,\text{MeV}$ at the telescope were done, while running the primary beam at maximum energy, $3.2\,\text{GeV}$. At this energy the multiple scattering angle is only $\theta_{\text{rms}} = 2.8\,\text{mrad}$ and the estimated extrapolation error is $57\,\mu m$, at a distance of $2\,\text{cm}$. This displacement has roughly the same magnitude as the pixel pitch of $50\,\mu m$. The trigger, as in the previous case, is generated as a coincidence between both scintillators.

Out of 12 possible correlation plots, between all the planes, only six are shown in figure 3.13 for the correlations between the first plane and all other planes. As a diagonal shows up in each of these plots the data synchronisation with four planes works as it should.

Compared to the correlation plots in figure 3.10 the width of the diagonal is much reduced, and the effect of the smaller multiple scattering angle is clearly visible. Again the statistics is very low and a coarse estimate gives a width of 1.5 mm for both directions. This decrease in width by a factor of one third reflects the smaller extrapolated shift due to multiple scattering. Further with four planes, and therefore more material in total, the width of the diagonal is expected to increase from plane 0 to plane 1,2 and plane 3. Due to the low statistics nevertheless this effect is not visible.
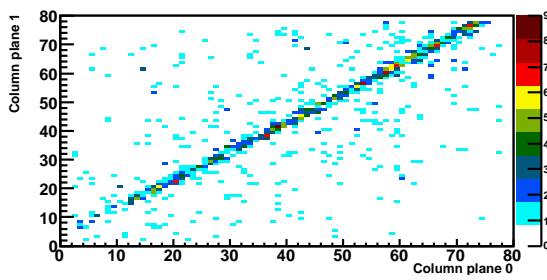
(a) X Correlation between plane 0 and plane 1
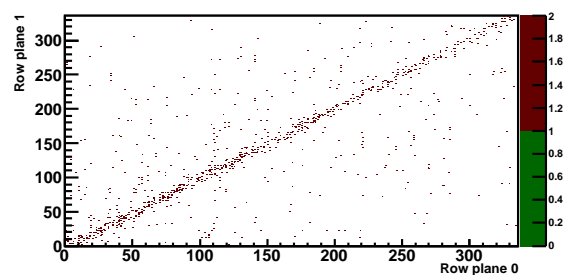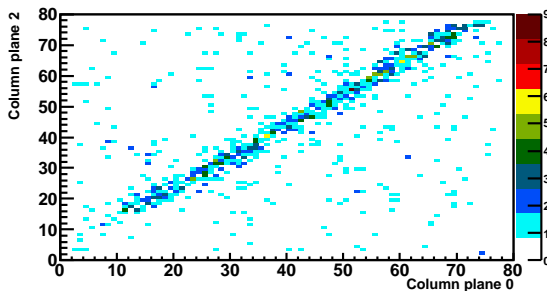
(b) Y Correlation between plane 0 and plane 1

(c) X Correlation between plane 0 and plane 2
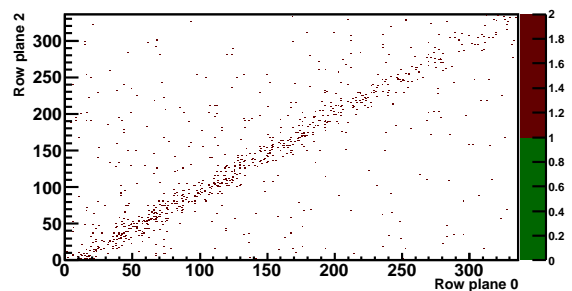
(d) Y Correlation between plane 0 and plane 2
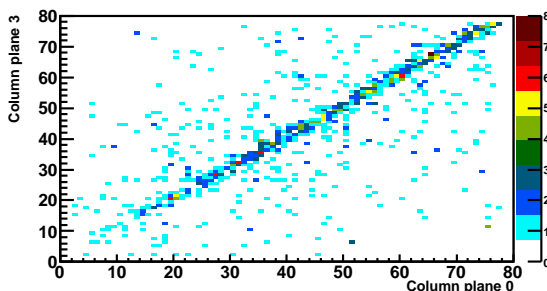
(e) X Correlation between plane 0 and plane 3
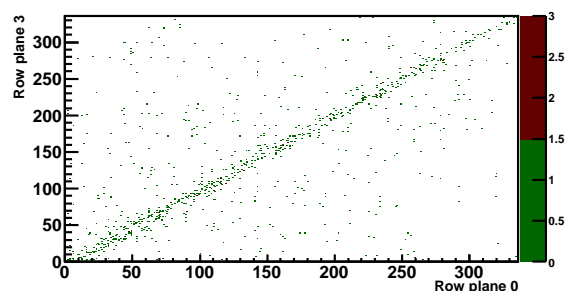
(f) Y Correlation between plane 0 and plane 3

Figure 3.13: Correlation plots between the first telescope plane against all other planes. The higher energy (416 MeV) with respect to the measurements shown in 3.10c and 3.10d is clearly visible in the width of the diagonal.

3.4 Telescope results from CERN using $120\,\mathrm{GeV}\,\pi$ beam

Although the basic functionality of the telescope system is demonstrated with the measurements done with low energy electrons in ELSA, additional tests with high momentum particles will help to study intrinsic properties of the sensors getting rid of the distortion due to the multiple scattering. Using the CERN accelerator complex, a beam of protons with an energy of 400 GeV is extracted from the Super Proton Synchrotron (SPS) and guided to a target to create a pion beam. After a selector magnet, 120 GeV pions are delivered to the experimental area where the FE-I4 beam telescope was installed. For this energy a multiple scattering angle of $\theta_{\mathrm{rms}} = 0.01\,\mathrm{mrad}$ is calculated. The extrapolation error due to multiple scaterring at this energy is $0.19\,\mu\mathrm{m}$ for a plane 2 cm away.

Two different configurations were studied, one with all the planes close together, only 2 cm apart, which is the smallest distance reachable using the SCCs for support. This setup is depicted in figure 3.14. In the second setup, the sensors are arranged in two telescope arms, with two planes each. The distance between the arms is set to 10 cm, enough space for the addition of one DUT in between.
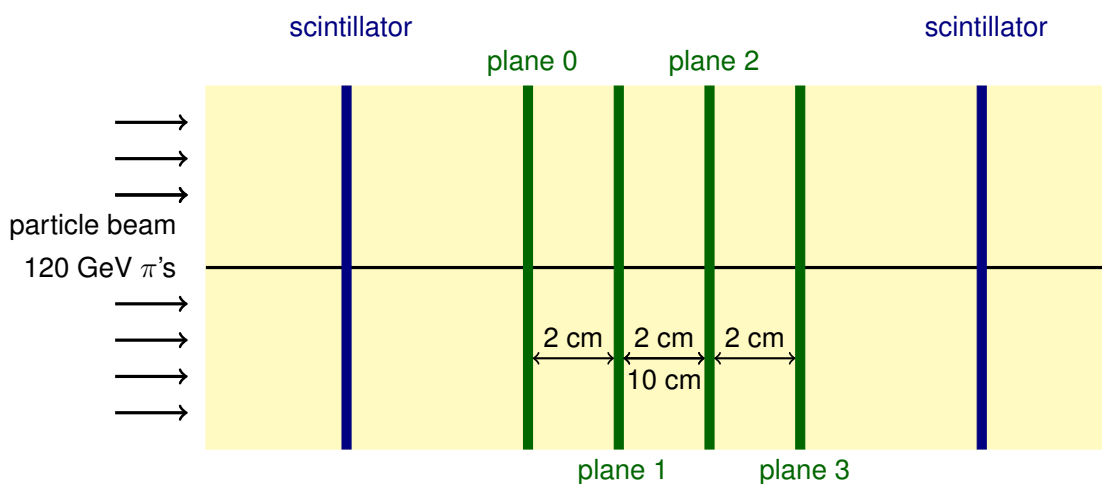
Figure 3.14: FE-I4-telescope with four planes and a different middle distance.

As the pointing resolution of the FE-I4 telescope not only depends on the intrinsic resolution but also on the extrapolation error of the fitting, as is explained in more detail in section 5.1.5, two different middle plane distances were chosen.

The six correlation plots relative to plane 0 where all plane to plane distances are equal are shown

in figure 3.15. Only the correlations between the first plane and all other planes are drawn for

(a) X Correlation between plane 0 and plane 1

(b) Y Correlation between plane 0 and plane 1

(c) X Correlation between plane 0 and plane 2

(d) Y Correlation between plane 0 and plane 2

(e) X Correlation between plane 0 and plane 3

(f) Y Correlation between plane 0 and plane 3
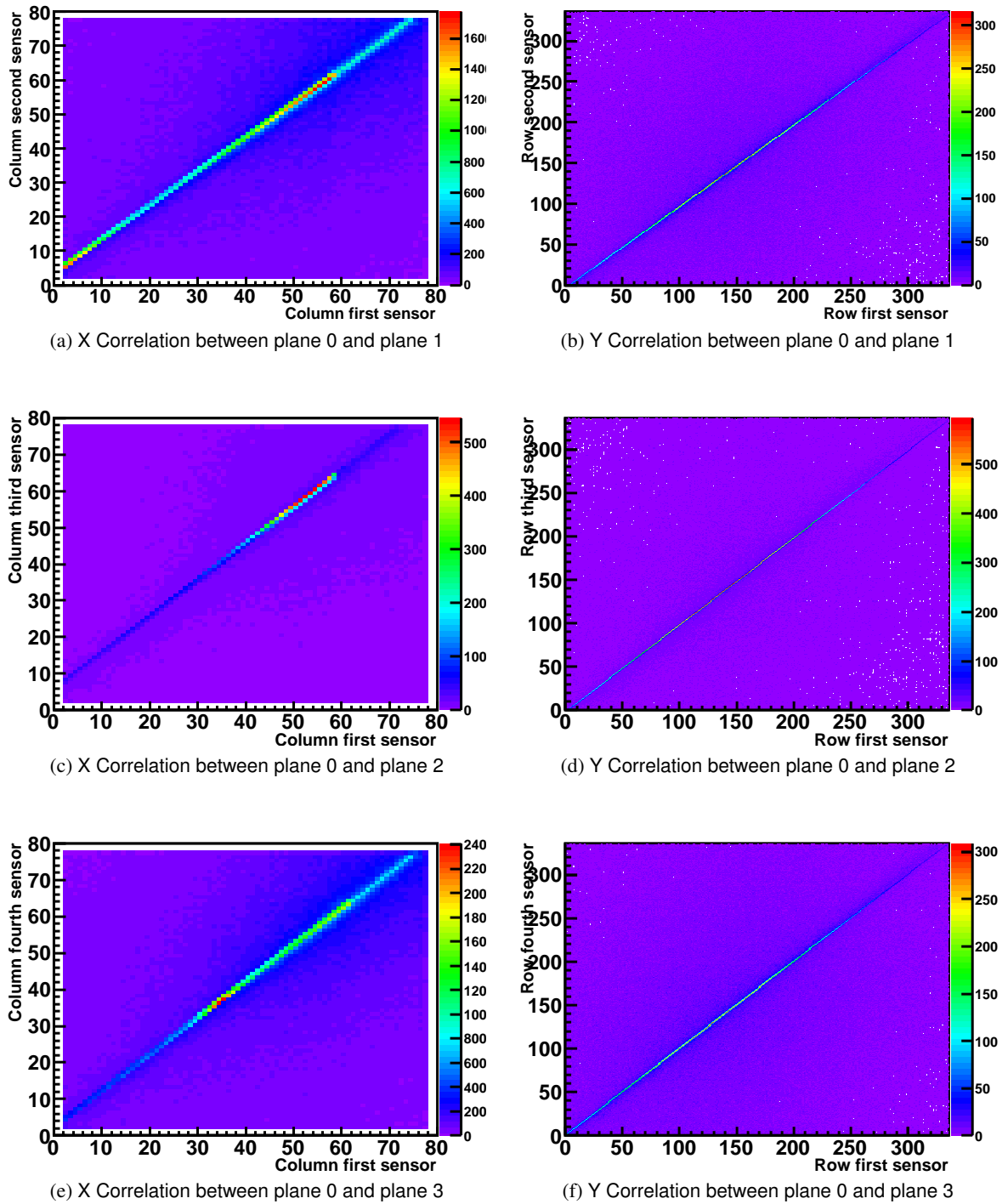
Figure 3.15: Correlation plots of first telescope plane to all other planes. Setup at CERN using 120 GeV π beam.

simplicity. The width of the diagonal has much decreased compared to the widths measured at ELSA. As much more statistics are available the width of the diagonal is determined through a fit of a Lorentz-curve on top of a quadratic background to the projection of one slice as shown in figure 3.16.
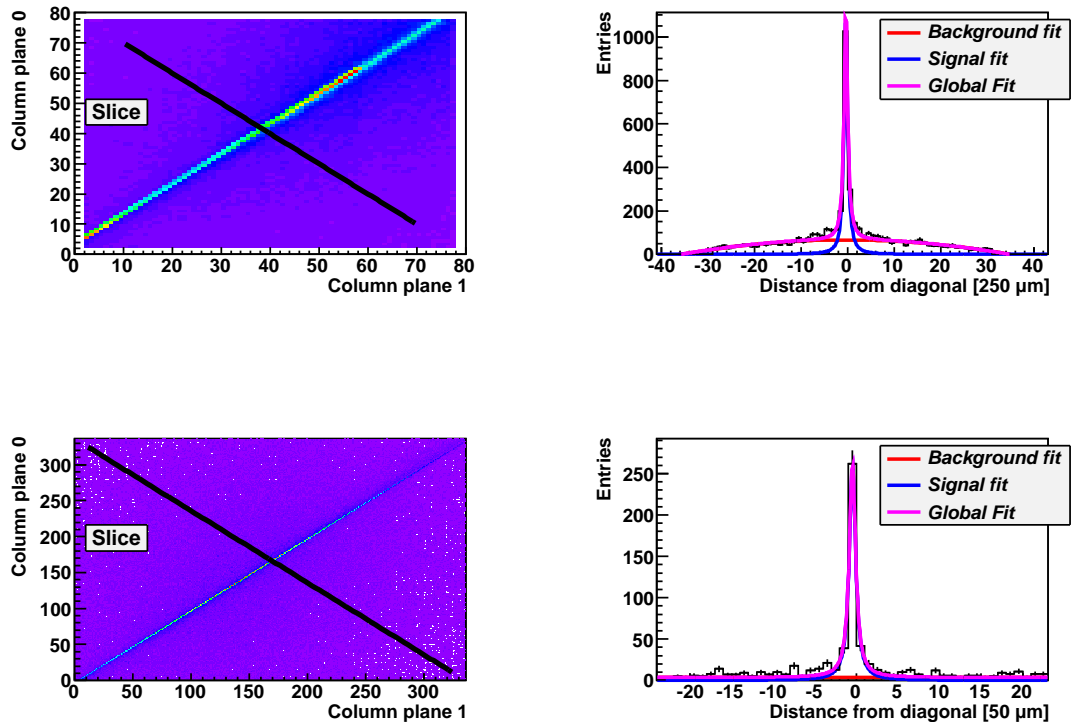
Figure 3.16: Experimental determination of diagonal width through projecting one slice, indicated through the black straight line, on the distance to the diagonal. In the upper two plots the X correlation and the projection of the X-diagonal are shown while in the lower part the same plots for the Y direction can be seen.

The width is found to be 0.96 ± 0.05 pixels in x direction and 0.92 ± 0.06 pixels in y direction for the diagonal of plane 0 and plane 1. Accordingly the width in x- and y-direction are $\sigma_x = 240 \pm 12.5\,\mu$m and $\sigma_y = 46 \pm 3\,\mu$m. As the extrapolated shift due to multiple scattering - $0.19\,\mu$m - is much smaller than both pixel pitches, it can be neglected. That is why now the width of the diagonal is limited by the pixel pitch in both directions.

In each of the correlation plots, figures 3.15a to 3.15f, one sees that the data acquisition works as expected. With both middle plane distances more than a million triggers are recorded. As for a test

beam data analysis with FE-I4 reference planes one needs roughly 10.000 triggers to make a plane alignment, the amount of triggers collected is sufficient. The analysis of the data is the content of chapter 5.

3.5 Comparison of multiple scattering effects

Measurements of the width of the diagonal of the correlation plot for three different energies are available. Those can be compared to the extrapolated shift from one plane to the next plane in order to see the effects of multiple scattering. In table 3.3 those values are confronted. From this table one can see that there is not a one to one correspondence between the calculated shifts and the measured widths, yet they both follow the same trend, that is, the effect of multiple scattering reduces at higher energies. Further, at 120 GeV the multiple scattering can be neglected and the pitch size only determines the width of the diagonal.

Energy E [MeV]	estimated shift [μm]	x width [mm]	y width [mm]
104	210	(2.5 ± 0.3)	(2.5 ± 0.3)
416	57	(1.5 ± 0.2)	(1.5 ± 0.2)
120.000	0.19	(0.24 ± 0.01)	(0.046 ± 0.003)

Table 3.3: Calculated shifts due to multiple scattering after a distance of 2 cm air and measured widths of diagonal from correlation plots.

Chapter 4

Measurements with region of interest trigger

In a telescope configuration a selective trigger is vital to ensure an efficient data acquisition. Tests with such a region of interest (ROI) trigger will be shown in the following. First, the implementation of different ROI windows is tested with the setup at ELSA. Second, the integration into the framework of the EUDET telescope is shown with a measurement done at DESY in Hamburg, where the ROI trigger is used to trigger the readout of the EUDET telescope reference planes. Third, the full functionality of the new method of ROI triggering is shown, using the EUDET telescope as well as a DEPFET DUT. This comissioning stage was carried out with a DUT at CERN.

4.1 Tests of different ROIs with $338\,\text{MeV}\ e^-$ at ELSA

As shown in the previous chapter, the basic functionality was tested with two FE-I4 planes, see figure 4.1. Instead of triggering the DAQ on the coincidence of two scintillators, the first module will be used to trigger the DAQ of both sensors in order to test the functionality of the ROI.

4.1.1 Tests with full ROI

To trigger the EUDET telescope only on particles passing through the whole active region as defined by the area of the reference planes, it is necessary to have a triggering device that covers these planes completely. With a FE-I4 reference plane, the biggest selectable triggering region is the whole pixel array, so a size of 16.8 mm x 20 mm. In order to test this feature the whole chip is set to be trigger sensitive except for the edges as they are known to have a different noise behaviour.
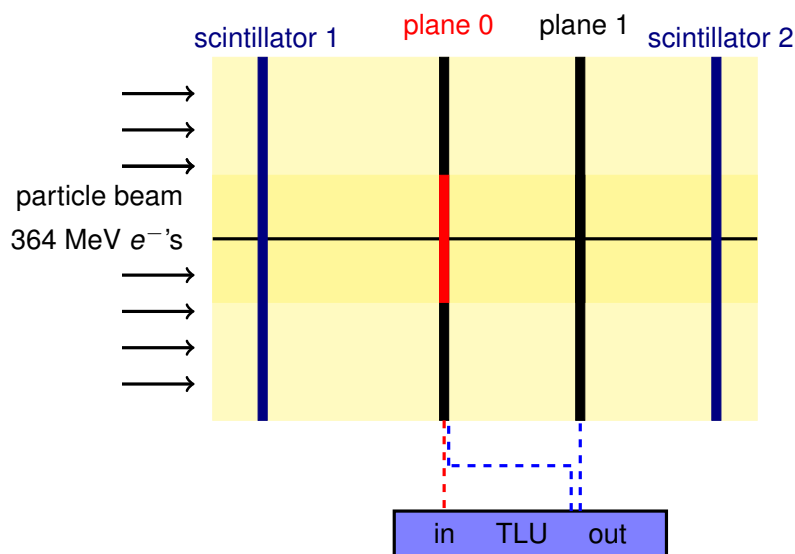
Figure 4.1: Telescope setup with two FE-I4 one-chip assemblies

The resulting hitmaps and correlation plots of the test with the full ROI are shown in figure 4.2. Both planes are in good alignment with the beam. The columns and rows that are switched off naturally show no entries. The diagonal in both x- and y-direction extends over the selected ROI.

From the diagonal it can be concluded that the triggering on the ROI - as set by the first plane - works as expected. Further, the data acquisition is obviously not disturbed by having almost all pixels trigger signal switched on. The TLU can handle the signal from the ROI of the FE-I4 reference plane and the data get synchronised in the correct way. No spurious effect coming from the new triggering method on the DAQ is observed.

4.1.2 Tests with different ROI windows

The ability to adjust the ROI window, using the HitOr of the FE-I4, according to the needs of the DUT configuration is one of the major advantages compared to scintillators, where triggering on the whole area is the only option. Further, the alignment of small scintillators to a DUT in a test beam is not accurate, as the exact positions are not always easy to measure. Here the programmable ROI has the advantage that it covers a relatively large area of 16.8 mm x 20 mm down to a single pixel (250 μm x 50 μm). This makes a coarse alignment to the DUT mechanically easy and fast. A more precise alignment to find the exact position of the DUT relative to the FE-I4 reference plane can be

(a) Hitmap plane 0

(b) Hitmap plane 1

(c) X Correlation between plane 0 and plane 1

(d) Y Correlation between plane 0 and plane 1
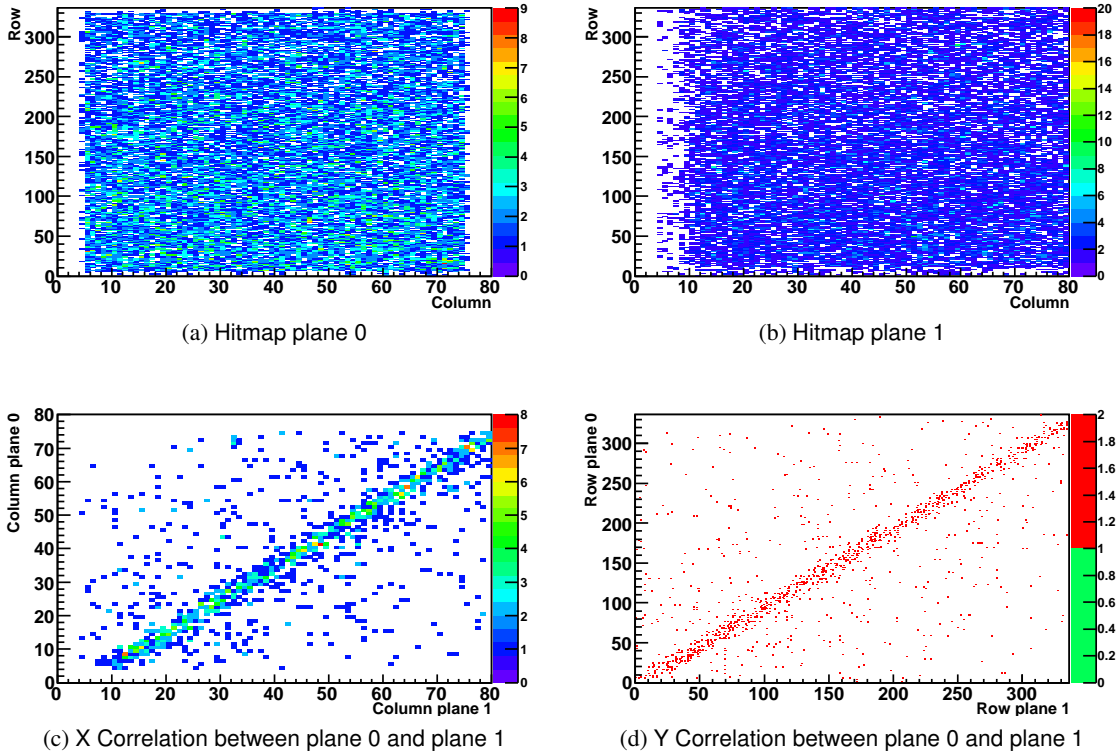
Figure 4.2: Hitmaps and correlation plots of telescope planes, HitOr window 18mm x 18mm, Run1169

done together with the correlation plots and the hitmaps.

In order to check the feature of choosing any region required by the application, two regions of different size are tested:

- ROI window of 10 mm x 10 mm: The hitmaps and correlation plots of an ROI of 10 mm x 10 mm size are shown in figure 4.3. In both hitmaps the region on which the whole telescope was triggered is visible. The ROI in plane 0 has exactly the form to which it is configured with very sharp edges. On the hitmap of plane 1, these edges are softened out due to multiple scattering. In both hitmaps the beam profile can be seen. The telescope is not well centered in the beam, a shift to smaller row-values and smaller column-values of the setup would be necessary to be better aligned with the beam.

- ROI window of 5 mm x 5 mm: The hitmaps and correlation plots of an ROI of 5 mm x 5 mm size are shown in figure 4.4. The hitmaps show the ROI on which both planes are triggered. In the correlation plots two pronounced bands in the column region from 50 to 70 and row region

from 55 to 75 are visible. These are entries from false combinations which are produced due
to noise hits in one of the planes.

(a) Hitmap plane 0

(b) Hitmap plane 1

(c) X Correlation between plane 0 and plane 1

(d) Y Correlation between plane 0 and plane 1
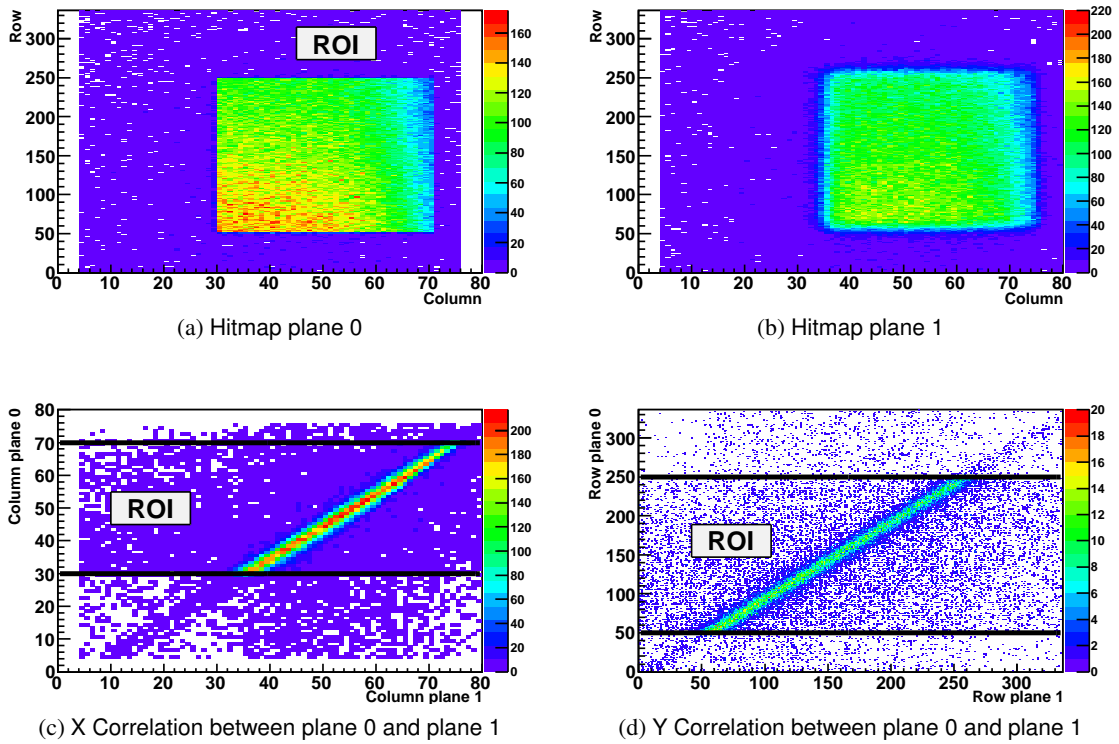
Figure 4.3: Hitmap and correlation plots of both telescope planes. The HitOr defines an active window of
10 mm x 10 mm.

(a) Hitmap plane 0

(b) Hitmap plane 1

(c) X Correlation between plane 0 and plane 1

(d) Y Correlation between plane 0 and plane 1
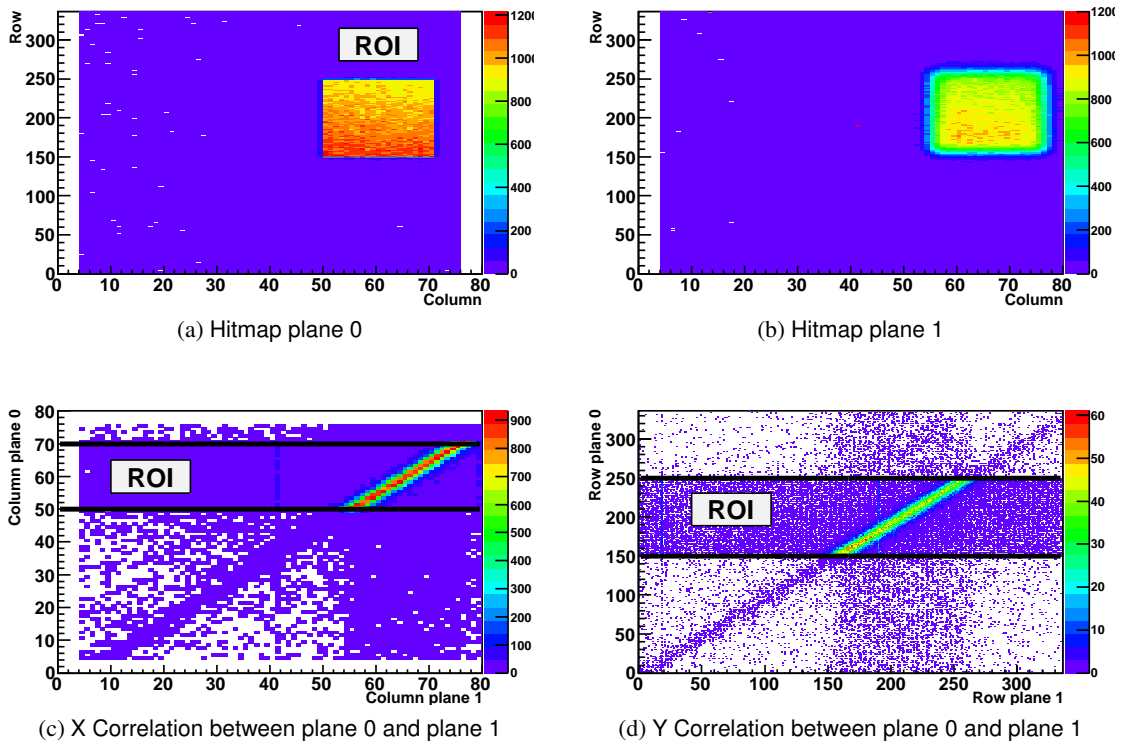
Figure 4.4: Hitmap and correlation plots of both telescope planes. The HitOr defines an active window in this case of 5 mm x 5 mm.

4.2 Frame by frame analysis of events

A detailed study of the hitmap in figure 4.3 reveals a fact that should not be present. There are hits outside of the defined ROI even in the plane on which it is triggered. Therefore, a more detailed frame by frame analysis of all triggers is required, in order to sort out the reason why those hits are present in a 'forbidden' region. Each trigger is sorted into three categories: only hits inside the ROI, hits inside and outside the ROI and hits only outside the ROI. In the ideal case there should be

(a) Frames with hits only inside the ROI. (b) Frames with hits inside and outside the ROI.
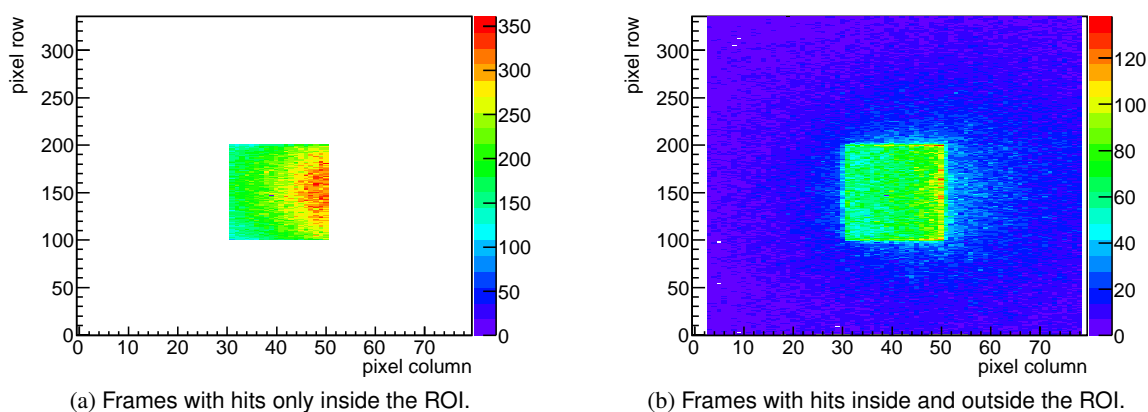
Figure 4.5: Frames sorted by hit positions, as measured at CERN. Approximately 450.000 frames are used for the analysis.

only triggers which have at least one hit but only inside the ROI. The case that there is a hit inside the ROI as well as outside is expected to occur rather often depending on the incident particle flux, because it might happen that in one trigger there are two particles of the beam passing the telescope at the same time, one of which causes the trigger. In figure 4.5 one can see the result of such a sorting for roughly one million of collected triggers. The measurement was done with the setup at CERN as described in the previous section. After analysing these triggers it turns out that no trigger is found where there is only a hit outside of the ROI. Therefore a limit of the occurrence of these unfavoured events of $< 10^{-6}$ can be given. The same analysis is done with data from a measurement at ELSA with a beam energy of 338 MeV, see figure 4.6 for the hitmaps. As hits only outside of the ROI occur , the corresponding hitmap is shown as well, see figure 4.6c. The numbers counted for both measurements are compared in table 4.1.   A small difference in the fraction of double hits occurs for the measurements at ELSA and at CERN. Both beams have different particle

(a) Frames with hits only inside the ROI.

(b) Frames with hits inside and outside the ROI.

(c) Frames with hits only outside the ROI.
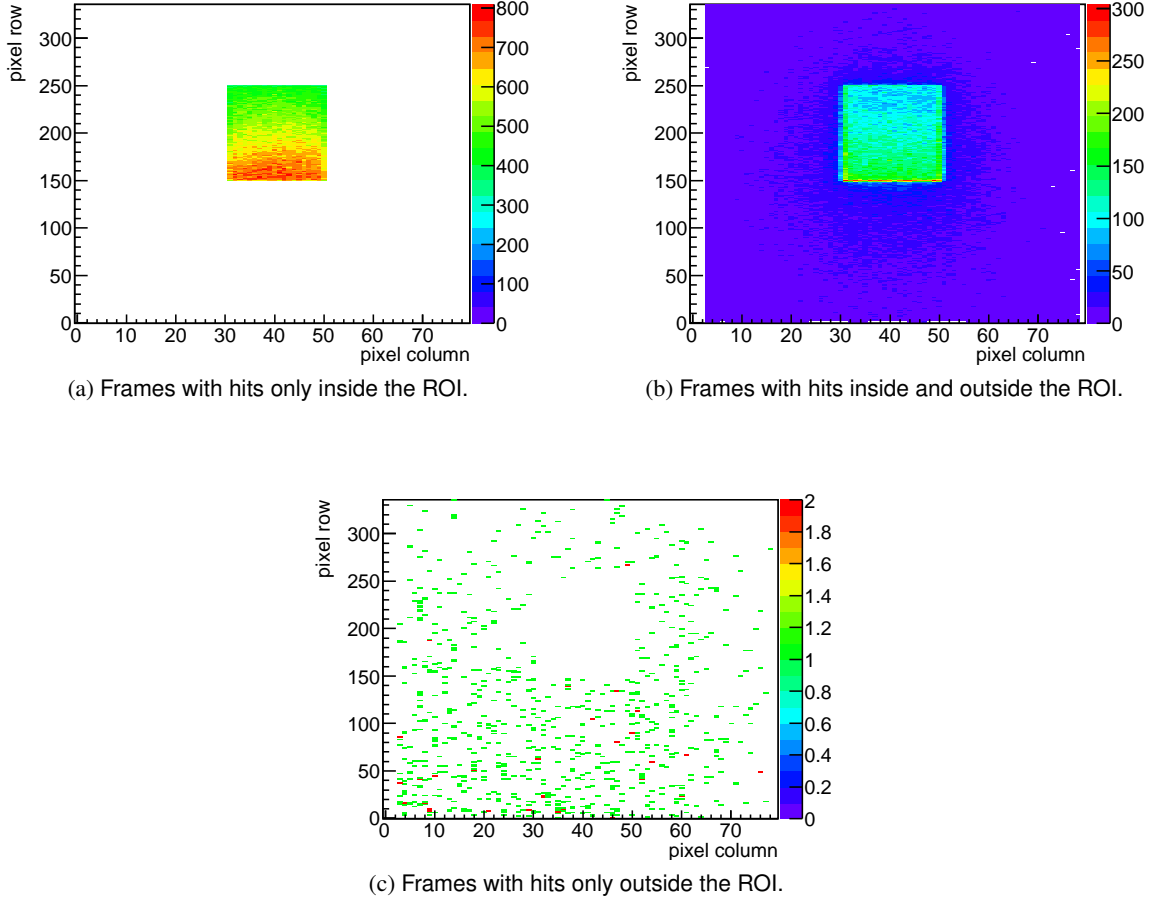
Figure 4.6: One million frames sorted by hit positions, as measured at ELSA. A few events with hits only outside the ROI occur.

accelerator	energy	#triggers	inside ROI + double hits [%]	outside hits [%]
CERN	120 GeV	443.588	> 99.99	< 0.01
ELSA	338 MeV	1.051.303	> 99.99	< 0.01

Table 4.1: Results of frame by frame analysis of measurements at ELSA and CERN.

fluxes and therefore a different fraction of double hits is to be expected. Contrary, the origin of hits only outside of the ROI is not identified yet. A possible reason is the threshold setting of the FE-I4 as well as the threshold setting of the TLU discriminator. If the thresholds are too low, noise hits might cause a fake trigger. In that case the frame could be empty or by chance contain a hit which can be on the whole pixel matrix, as it is uncorrelated to the trigger. Anyhow, as seen from both measurements, the probability of having a trigger from the area outside of the ROI is negligible.

4.3 Integration tests with `EUDET` telescope

Although the functionality of the HitOr was demonstrated using the FE-I4 telescope standalone, a dedicated campaign for the integration with the `AIDA` telescope was done at `DESY`. The commissioning of the FE-I4 region of interest trigger together with an `EUDET`-like telescope was done at `DESY` in Hamburg with electrons of 4 GeV using the setup shown in figure 4.7 and 4.8: a FE-I4 reference plane is placed in between the two telescope arms, each arm equipped with three `MIMOSA26` reference planes close to each other, and two crossed scintillators, in front and behind the whole assembly. As ROI, an area of 3 mm x 7 mm, shown in figure 4.9, was selected in this case and the whole telescope is being triggered on a coincidence between the ROI and three scintillators. As
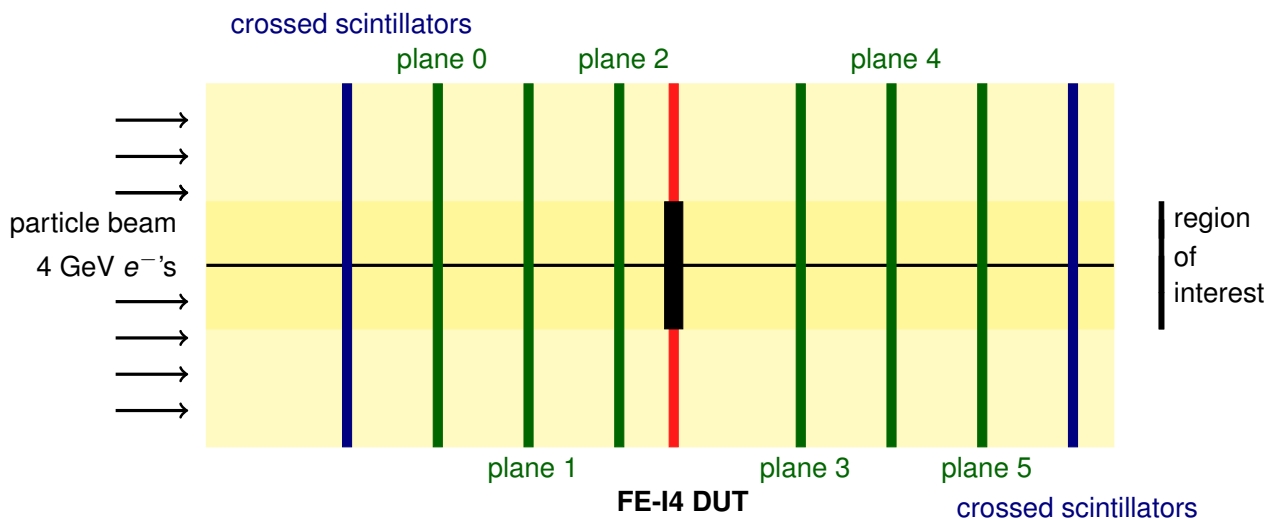
Figure 4.7: Setup of the `Eudet`-telescope copy `Anemone` together with a FE-I4 reference plane.
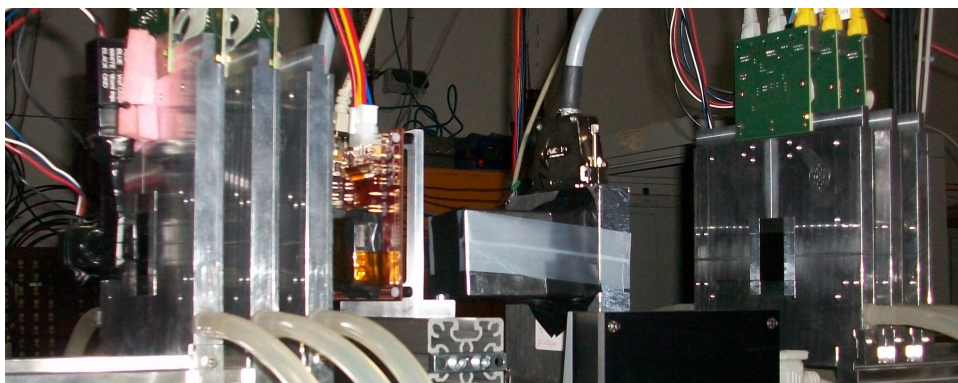
Figure 4.8: Picture of the setup of the `Anemone` telescope together with a FE-I4 reference plane.
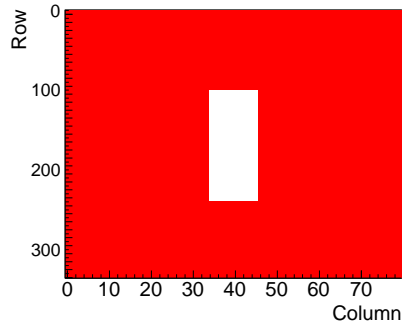
Figure 4.9: FE-I4 region of interest chosen to trigger the full `Anemone` telescope.

the ROI is smaller than the scintillators the trigger sensitive region is limited by it. In the hitmaps of all telescope planes, shown in figure 4.10, the shape of the active trigger region is clearly visible on their reference point of view. The `EUDET` telescope reference planes have square pixels with a pitch of 18.4 μm. The shape of the ROI is roughly 500 times 200 pixels big which corresponds to an area of 3 mm x 7 mm and therefore matches to the ROI preselected through the FE-I4 HitOr reference plane. The borders of the rectangular hit distribution are not sharply defined as the multiple scattering contributes to the deflection of the incoming e^-. This effect is escpecially visible in the hitmaps of the last three planes placed right after the *thick* FE-I4. Therefore, to avoid this effect, for the final arrangement, the FE-I4 is placed behind the last plane of the telescope. The area is also slightly shifted to smaller row numbers when going from the first to the last plane, which can be due to misaligned planes as well as from a not exactly perpendicular incident beam.

From the hitmaps of all telescope planes the general functionality and compatibility of the FE-I4 ROI trigger with the `EUDET` telescope can be concluded.

For efficiency measurements with FE-I4 DUTs it is necessary to take data with the FE-I4 plane in order to use it as a timing reference. The setup to test this is the same as above. A region of interest of some twenty pixels was chosen. All pixels are read out. The results are shown in figure 4.11. With the FE-I4 it is possible to distiguish noise hits from true hits through a time measurement of the trigger delay. When reading out the data from the FE-I4 16 consecutive triggers of 25 ns length are sent to the chip and only those matching to a counter that started with the hit are read out. Consequently true hits occur always at the same of these 16 triggers whereas noise hits appear at any time if they are uncorrelated to the trigger signal. Plotting the trigger distribution of the FE-I4

(a) Hitmap plane 0

(b) Hitmap plane 1

(c) Hitmap plane 2

(d) Hitmap plane 3

(e) Hitmap plane 4

(f) Hitmap plane 5
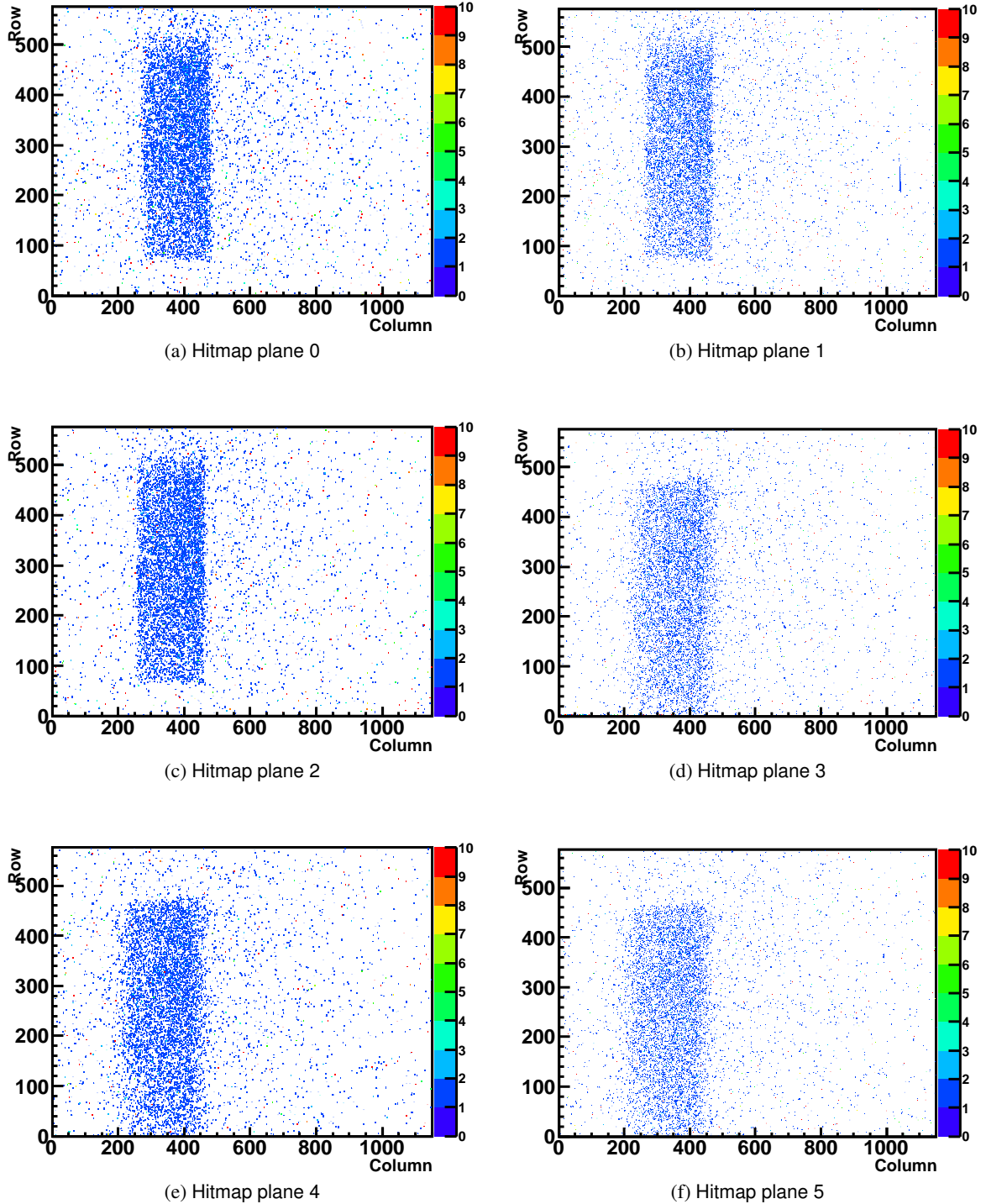
Figure 4.10: Hitmaps of reference planes of EUDET telescope triggered on region of interest implemented through the FE-I4 plane. The selected region of interest of 3 mm x 7 mm can be seen in all hitmaps.

results in the plot shown in figure 4.11b. A sharp peak at two is very pronounced. From this peak it follows that the triggers are generated from true particles and not from noise.

Furthermore, the two correlation plots of the FE-I4 and the telescope plane closest to it are shown, see figure 4.11c and 4.11d. The tiny visible part of the diagonal is exactly where expected. This shows that the data is sorted in a synchronous way and that the EUDET DAQ is not disturbed by the FE-I4 DAQ.

(a) Hitmap FE-I4 plane

(b) Trigger distribution FE-I4 plane

(c) X Correlation FE-I4 plane to MIMOSA plane 2

(d) Y Correlation FE-I4 plane to MIMOSA plane 2
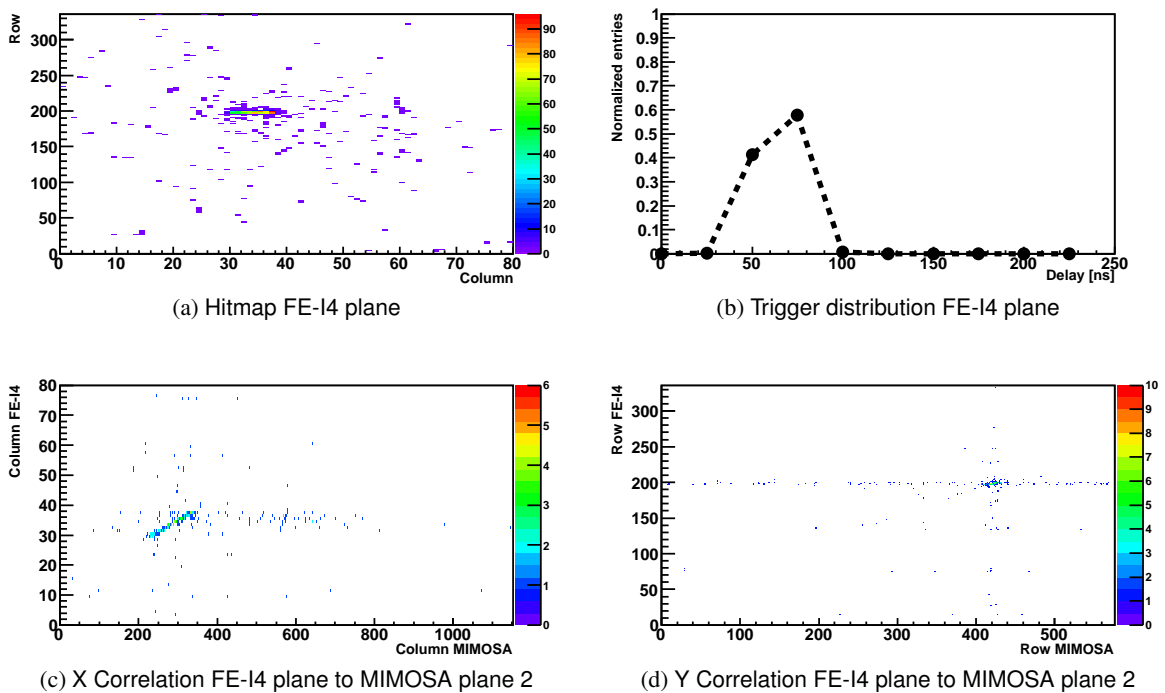
Figure 4.11: Hitmap and trigger distribution of FE-I4 reference plane and correlation plots of FE-I4 reference plane to the closest EUDET reference plane.

4.4 Triggering the `DEPFET` DUT in a test beam with the ROI trigger

A measurement to test the complete functionality of the ROI trigger in a test beam environment together with an external DUT, is carried out at CERN. The setup - as shown schematically in figure 4.12 (a real picture can be seen in figure 4.13) - consists of the `EUDET` telescope with six planes, a `DEPFET` pixel detector [28] in between the two arms as DUT and a FE-I4 ROI trigger plane at the end. This setup reflects a possible configuration of a future `AIDA` telescope.
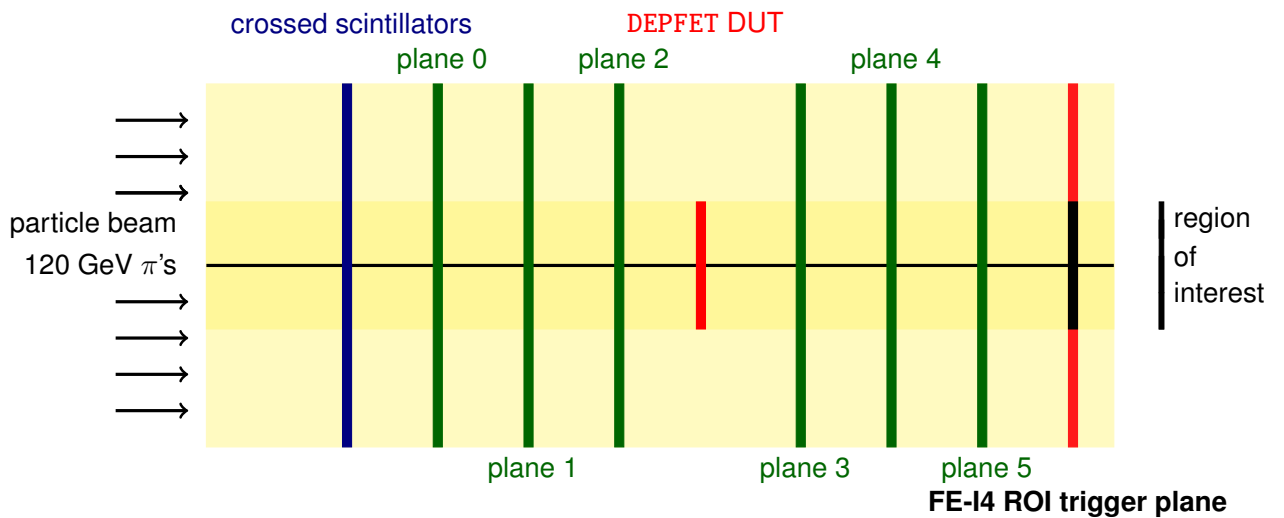
Figure 4.12: Setup of `Eudet`-telescope with a `DEPFET` DUT and a FE-I4 ROI trigger plane.
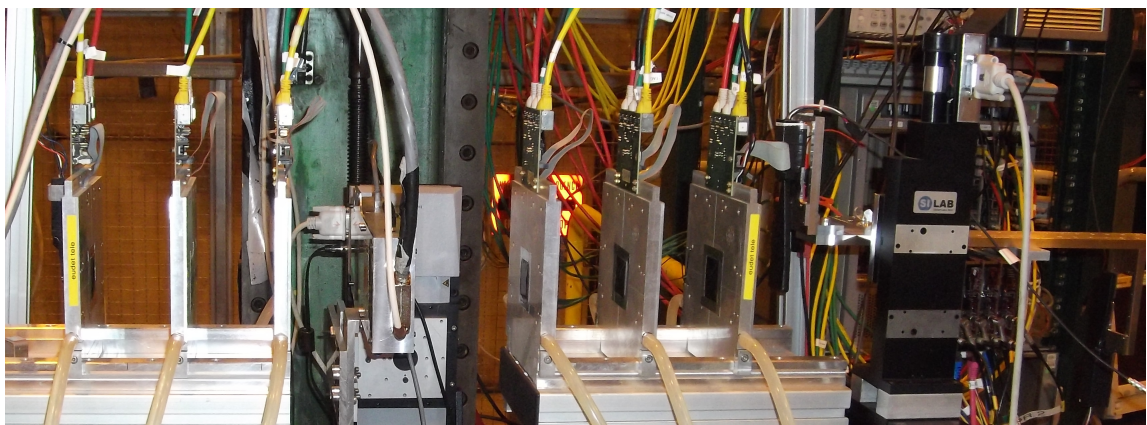
Figure 4.13: Setup of `Eudet`-telescope with a `DEPFET` DUT and a FE-I4 ROI trigger plane, at H6B CERN North Area.

The `DEPFET` has 32 columns and 64 rows and that, together with a pixel pitch of $50\,\mu$m x $75\,\mu$m, results in a matrix with a total size of 4.8 mm x 1.6 mm. Compared to the `EUDET` telescope reference

planes - 2 cm x 2 cm - the DEPFET is only one tenth in area. As a consequence the usual trigger-
ing scheme as tested in previous test beams [29] leads to a data taking where 80% of the events
triggered and stored, do not show a hit in the DEPFET. To be more efficient in terms of having a
track going through the DEPFET the trigger for the whole system is generated through a coincidence
between one of the scintillators in the front and the FE-I4 plane with the ROI conveniently chosen
to cover the area defined by the DEPFET. The HitOr signal from the FE-I4 plane is integrated as
described in section 2.4.2. As the scintillator covers the whole FE-I4 reference plane the limiting
area in the coincidence between the scintillator and the ROI selected by the FE-I4 is the ROI.

After a coarse alignment of the FE-I4 plane to the EUDET sensors using the correlation plots of the
online monitor, an iterative selection of the optimal ROI based on the track efficiency is done. As the
ROI is freely adjustable, even small areas can be switched on or off. After a few iterations, the final
position of the ROI is found, with a size of 20 FE-I4-columns and 36 FE-I4-rows, which is equivalent
to 5 mm x 1.8 mm, overlapping the DEPFET. The limiting factor in both directions is the pixel pitch,
so 250 μm in x-direction and 50 μm in y-direction. Each side of the ROI was chosen to be 0.2 mm
longer than the size of the DEPFET in order to have a complete overlap. As this position depends on
the location of the DEPFET it has to be selected individually after changing the DUT position.

The first step was to check that only hits were recorded in a small area, see figure 4.14 for the
chosen ROI and the correspondig hitmap of the DEPFET. Then the ROI as extended to overlap the
DEPFET and like this the DAQ was done. The track efficiency of the measurement with an overlap-
ping ROI is 80% as compared to 20% which is reached when triggering only on the scintillators.
Therefore an improvement of a factor four concerning the track efficiency is reached.

(a) ROI as selected through the FE-I4 plane.

(b) Hitmap of DEPFET DUT.
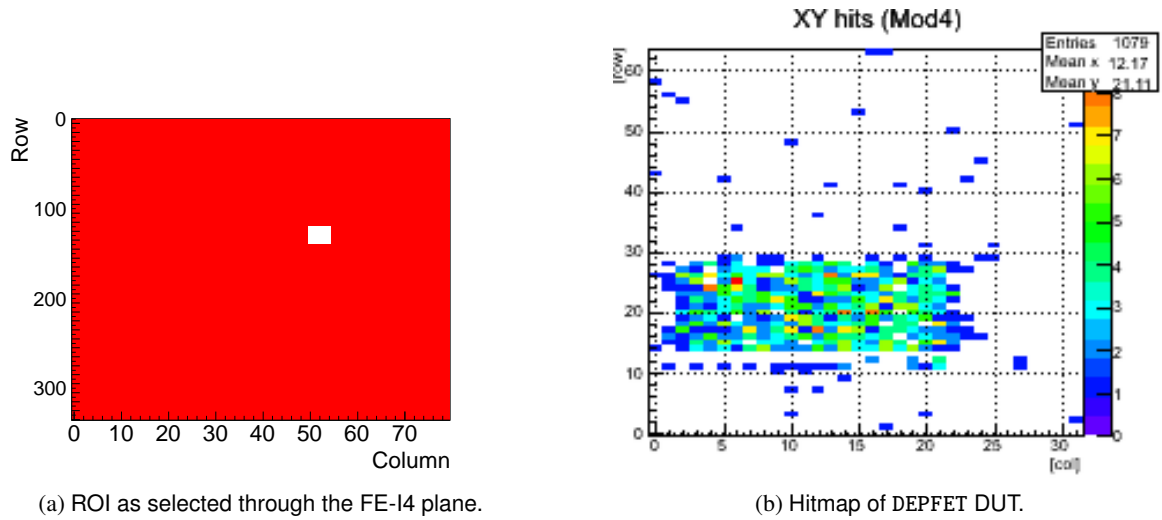
Figure 4.14: Selected ROI, which is smaller than the DEPFET and corresponding Hitmap of DEPFET. The trigger is generated as a coincidence between the front scintillator and the ROI trigger.

(a) ROI as selected through the FE-I4 plane.

(b) Hitmap of DEPFET DUT.
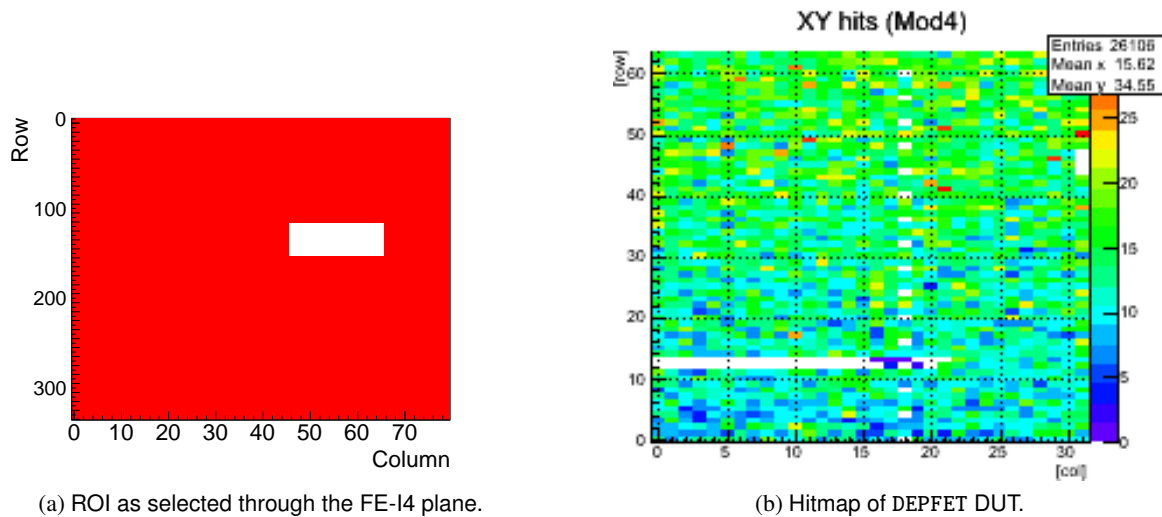
Figure 4.15: Selected ROI trigger and corresponding Hitmap of DEPFET. The trigger is generated as a coincidence between the front scintillator and the ROI trigger.

Chapter 5

Analysis of test beam data

The analysis of test beam data, meaning the offline event and track reconstruction, can be done with the software package `EUTelescope`, a general analysis infrastructure developed by the `EUDET` collaboration. This package, described in detail in [9], is based on the highly modular `Marlin` framework that was designed for the `ILC`[1] project [30]. The full analysis is achieved using a modular approach and it is possible to adapt the different packages of this software to a FE-I4 beam telescope as well. The data analysis chain is divided into five steps. First, a conversion into a common data format is done and the geometry of the setup (including material properties) is defined. Second, clusters need to be found and hits reconstructed. Third, a transformation from the local reference frame into a global reference frame has to be done. Fourth, the planes have to be aligned, which can be done properly with a data sample of 10.000 events. Fifth, the tracks are fitted and the results can be analysed. In order to get to the DUT properties, residuals and efficiencies can be calculated using the software package `TBMon`, a Testbeam Monitoring software package.

The individual steps shall be explained in more detail here:

- File conversion: As Marlin relies on the `LCIO`[2] format, the raw data written by the `EUDAQ` software needs to be converted. In addition, broken pixels can be identified and are masked automatically if their hit occupancy is higher than that of a normal working pixel.

- Clustering: The number of pixels firing when a particle traverses the sensor is, in general, larger than one. Therefore, nearby firing pixels that are likely to belong to one common hit

---

[1] International Linear Collider.
[2] Linear Collider Input Output.

can be grouped to clusters. The cluster algorithm used in this step is the nearest neighbour algorithm where the cluster size - that means the number of pixels belonging to the cluster in the corresponding direction - can be limited in order to cut a significant fraction of δ-electrons or nuclear reactions. Both δ-electrons and nuclear reactions share the signature of long tracks.

- Hit Maker: After finding all clusters, the hit positions must be calculated. This is done by computing the signal weighted average position of the cluster using the charge Center of Gravity (CoG) algorithm. Further a transformation from the local reference frame, in which all coordinates are pure plane coordinates, to the global telescope reference frame, where all plane coordinates are in one frame, is done.

- Alignment: As the telescope geometry can only be adjusted with coarse mechanical precision, typically much larger than the desired resolution, the deviations between the nominal sensor and the actual sensor positions must be corrected for. The misalignement of the sensors is determined using `Millepede II` [31]. A track fit procedure is performed and the alignment constants are calculated from the resulting tracks. Such constants are shifts and rotations of the sensors in the *x*-*y*-plane as well as angles of rotations around the *x* and *y*-axis. The *z*-positions are measured and act as fixed parameters in the alignment.

- Track fitting: As the particles scatter while passing through the telescope, the tracks are not straight lines. The track fit takes into account the measured hit position as well as the expected scattering angle distribution. The major contribution to the deflection of the particle comes from multiple `Coulomb`-scattering. For small angles the distribution of the scattering angles is Gaussian. The width of this distribution is the mean multiple scattering angle, see formula 1.3. The track fit is performed via a χ^2 minimization, where the χ^2 function includes both the measurements x_{meas}^i and y_{meas}^i and the expected scattering angle distributions. The total χ^2 function is the quadratic sum of the χ_x^2- and χ_y^2-functions (in *x* and *y* directions respectively),

where the calculation is analogous for both directions and only the χ_x^2 is given here:

$$\chi_x^2 = \underbrace{\sum_{i=1;i\neq i_{\text{DUT}}}^{N} \left(\frac{x_{\text{meas}}^i - x_{\text{fit}}^i}{\sigma_{\text{sensor}}}+\right)^2}_{\text{measurement}} + \underbrace{\sum_{i=2}^{N-1} \left(\frac{\theta_x^i - \theta_x^{i-1}}{\sigma_\theta^i}\right)^2}_{\text{expected scattering}}. \tag{5.1}$$

The first sum, where i runs over the N different planes except for the DUT plane, includes the measured and fitted hit positions as well as the intrinsic resolution of the sensor σ_{sensor} while the second sum takes into account the effect of multiple scattering where θ_x is the angle projection defined through figure 5.1 and σ_θ the mean multiple scattering angle. With the additional assumption that the multiple scattering angle is small the problem can be solved analytically. All assumptions on which the analytical approach is based on are [23]:

– all telescope planes are parallel to each other

– the incoming beam is perpendicular to the telescope planes and has a small angular spread

– particle scattering angles in subsequent telescope layers are small

– thicknesses of all material layers are small compared to the distances between the planes

– particle energy losses in the telescope layers can be neglected

As inputs to the χ^2 function are, since they are properties well known, the following:

– z position of the sensors

– thickness of the sensors

– resolution of the sensors σ_{sensor}.

Here a significant difference between the EUDET telescope and the FE-I4 telescope becomes apparent. As the reference planes of the EUDET telescope consist of pixels with 18 μm x 18 μm pitch, the value σ_{sensor} is the same for both directions. This is different for the FE-I4 based reference planes, where the pixel pitches are 50 μm and 250 μm, and therefore two different sensor resolutions $\sigma_{\text{sensor,x}}$ and $\sigma_{\text{sensor,y}}$ are needed. Also the EUDET telescope
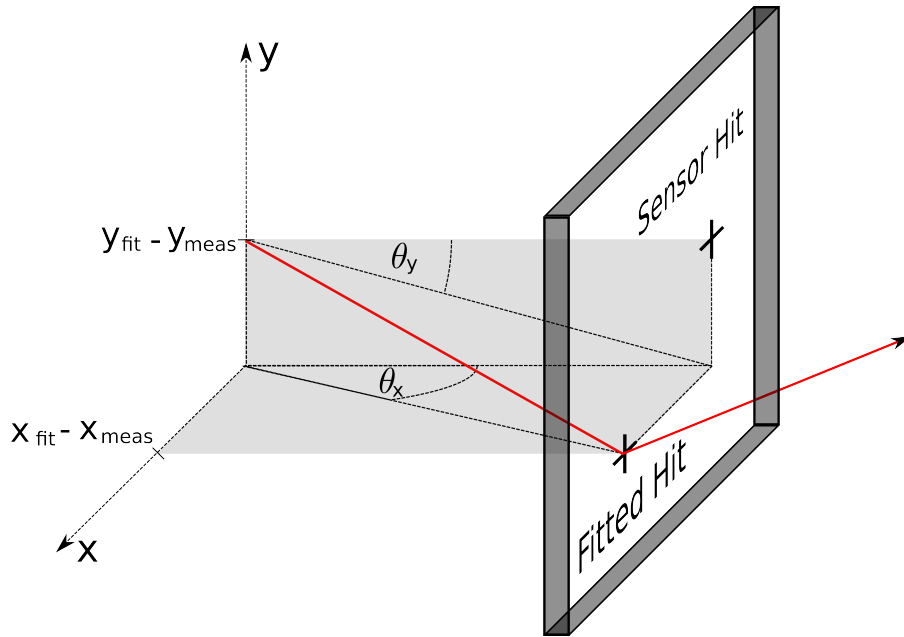
Figure 5.1: Definition of the projected scattering angles. The displayed angles correspond to the sensor preceding the one shown [32].

reference planes have a sensitive thickness of 20 μm, while in the FE-I4 beam telescope, the reference planes are a factor 10 thicker.

5.1 Analysis of test beam data using a $120\,\text{GeV}\,\pi$ beam at CERN

The analysis of the test beam data from CERN is presented here. After converting all data from raw to LCIO format, the analysis chain is done in several steps.

5.1.1 Clustering

Once the geometry and sensor properties are defined, the channels along the sensor with the highest energy deposition are found. They are called seed channels. It happens nevertheless that a particle typically deposits its energy in more than one pixel. If that is the case the hit position can be estimated from all these pixel, which form a cluster. Further these pixels need to be grouped together in order not to mistake them as many different hits.

The clustering algorithm used here works as follows. For each event the pixel with the highest energy deposition is marked as the seed pixel. Then the algorithm checks the energy deposition

in the neighbour pixels. If these have a deposition above a certain cut value, they are included in the cluster and the search in this direction goes on, if not, the search stops. A single pixel showing a signal is defined to be a cluster of size one, if two neighbour pixels show a signal they make a cluster of size two and so on.

5.1.2 Influence of δ-electrons

δ-electrons alter the hit position significantly if they reach a neighbour pixel and deposit their energy partially there and in the pixel they originate from. In particular, events in which δ-electrons cause errors in the reconstruction of the hit position, must be cut. Separating events with δ-electrons from those without can be achieved using the cluster size of both pitches.

Calculation of rate of δ-electrons in telescope reference planes

A characteristic of δ-electrons, that can be used to identify them, is that they have higher energies (T) at smaller angles (θ), where $\theta(T) = \arctan \sqrt{2m_e/T}$ holds, see figure 5.2a for the angular range from 0 to 90°. The rate of δ-electrons depends on the velocity of the incoming particle, on the material properties and on the kinetic energy of the δ-electrons themselves [T_{min}; T_{max}].

$T_{\mathbf{max}}$: The highest energy T_{max} at which a δ-electron can still reach another pixel is given by $\tan \theta_{max} = \frac{\text{pitch}}{\text{thickness}} = \frac{50 \, \mu m}{200 \, \mu m} = 1/4 \rightarrow \theta_{max} = 14°$ for the short 50 μm side. This corresponds to
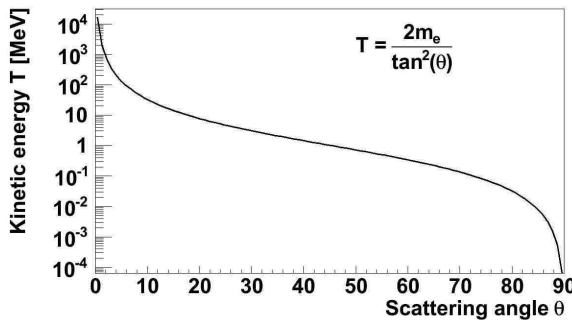
(a) Energy-angle relation of δ-electrons.
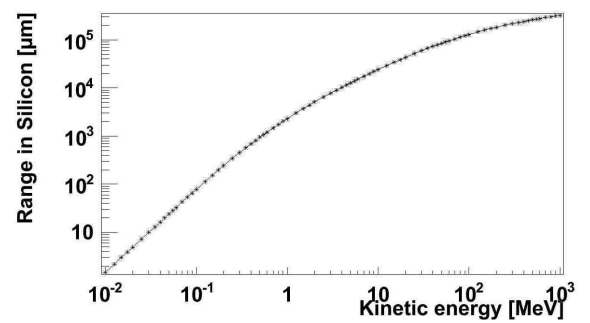
(b) Range of δ-electrons in silicon [33].

Figure 5.2: From these two plots the minimum and maximum energies for the calculation of the rate of δ-electrons is taken.

an energy of $T_{max} = 16$ MeV. If a δ-electron has a higher energy (T) and correspondingly a smaller

angle (θ) it travels more closely to the trajectory of the passing particle. However δ-electrons at small angles are supressed by a factor $1/cos^3\theta$.

T_{min}: An estimate for the minimum energy of a δ-electron T_{min} to cause an effect in the detector can be obtained from a range-energy plot which can be found in 5.2b. Here one can read off that for a range of 50 μm an electron needs at least T_{min} = 90 keV.

Using these values as input to equation 1.2 one obtains the rates summarized in table 5.1. The $1/T_{min}$ dependence of the rate can be seen directly from the calculated numbers. The short pixel pitch corresponds to the smallest T_{min} and consequently the influence of δ-electrons is expected to be larger in this direction than in the direction of the long pitch.

Measurement of rate of δ-electrons in telescope reference planes

To measure the effect of δ-electrons the cluster size of both directions can be used. As such, the fraction of δ-electrons can be estimated by comparing the fraction of clusters with a size above a chosen cut to the ones below that cut.

The cluster size in both directions is shown in figure 5.3 for all planes for one run with roughly 400.000 triggers. In the long pixel pitch direction the cluster size is predominantly one which means

(a) Clustersize X - long pixel pitch   (b) Clustersize Y - small pixel pitch
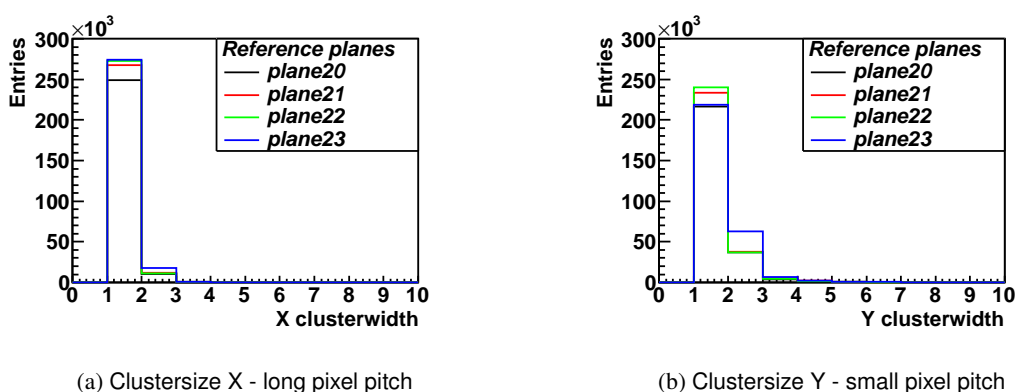
Figure 5.3: Cluster size in x and y for all planes for one run with 120 GeV pions.

that only one pixel is hit. A small fraction of cluster size two can be seen, that is due to particles crossing the sensor close to the border of the pixels in the x-direction. In the short pixel pitch direction the fraction of cluster size two is larger compared to the long pitch and clusters consisting

of three and even four exist. Because of the shorter pitch the charge sharing is more pronounced here. Also the effect of particles passing through the sensor close to the border of a pixel is more apparent here. Making a cut on the clustersize that allows only one pixel in the long direction and

sensor thickness [μm]	pixel pitch [μm]	energy range [keV]	$(N_\delta/N_0)_{\text{calc}}$ [%]	$(N_\delta/N_0)_{\text{meas}}$ [%]
200	250	200-670	1.2	2.5 / 2.9 / 2.4
	50	80-16.000	4.4	4.3 / 4.4 / 4.1
250	250	200-1500	1.9	3.8
	50	80-25.000	5.6	6.3

Table 5.1: Rates of δ-electrons normalized to the number of incident particles for the two different sensor thicknesses used in the FE-I4 telescope. The calculated rates are confronted against the measured rates for a cut at one pixel in the long pitch direction and at two pixels in the short pitch direction.

two in the short direction the normalized fraction of cut events is given in the last column of table 5.1. These numbers are in the same order of magnitude than the estimated rate of δ-electrons. The cuts have the biggest effect on the last plane which is expected as it is 50 μm thicker than the others. Further in the x direction some data is lost, as roughly 4 % are cut while only $1 - 2$ % of the events are expected to be due to δ-electrons. Further, the calculated rate fits much better for the short side than for the long side. This effect can be due to the cut selection which is in the case of the long pixel pitch limited to one as there are no clusters bigger than two.

5.1.3 Transformation into global reference frame

For completeness, the steps of the transformation from the pixel coordinate frame to the local reference frame to the global reference frame are shown in figure 5.4. The origin in the global reference frame is in the middle of the reference planes.

5.1.4 Alignment

The alignment is done using `Millepede II`. The first plane is taken as a fixed plane and all other shifts in *x* and *y* are being calculated, knowing the *z* positions of all the planes. The shift in the *x* direction between the first plane and the last plane is Δx=1.759 mm and in *y* it is Δy=0.219 mm respectively. These shift are applied to the data. In figure 5.5 the correlation plots before and after

(a) Pixel reference frame   (b) Local reference frame   (c) Global reference frame
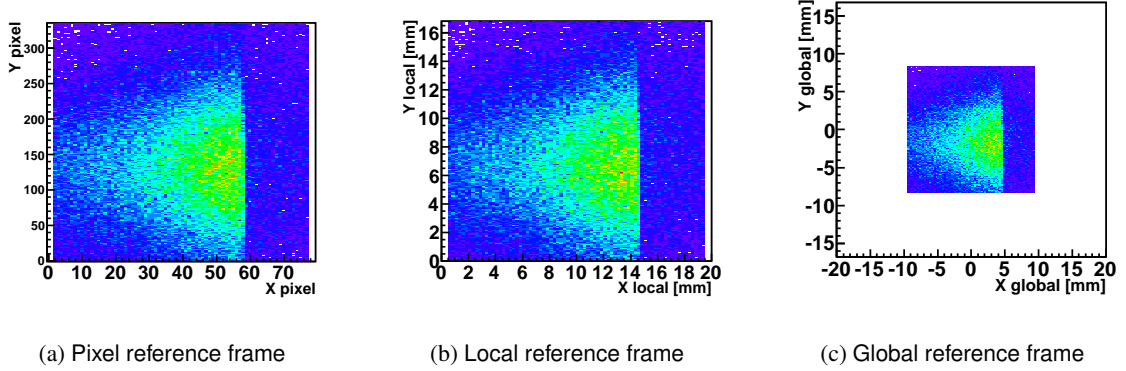
Figure 5.4: Transformation of reference frame, from pixel to global reference frame.

an alignment can be seen. In the plots before alignment one can see that the diagonal does not go through zero whereas after the alignment it does. It follows that the alignment procedure works as expected and small misalignments can be corrected for.

5.1.5 Track fitting and spatial resolution estimates

The track fitting does not give any conclusive results yet. A reason for that could be the already mentioned different sensor resolutions. Further, as there are mainly clusters with only one pixel in the *x*-direction, no improvement in resolution from the 'Center of Gravity' algorithm is to be expected in that direction.

The expected pointing resolution of the FE-I4 beam telescope can be estimated from the unbiased residuals of each of the telescope reference planes and the specific geometrical arrangement, see [32, 34] for a similar analysis with the EUDET telescope. The unbiased residual is the difference between the measured position and the extrapolated position of a hit. In the case of a telescope with a DUT, three factors influence the width of the unbiased residual distribution (σ_{residual}) of that DUT. Those are the intrinsic resolution ($\sigma_{\text{intrinsic, DUT}}$) of the DUT, the smearing due to multiple scattering $\sigma_{\text{multiple scattering}}$ and the error of the extrapolation ($\sigma_{\text{telescope}}$) which depends on the positions of the planes as well as on their intrinsic resolution ($\sigma_{\text{intrinsic, plane}}$). These three contributions add up quadratically to the width of the unbiased DUT residual width:

$$\sigma_{\text{residual, DUT}}^2 = \sigma_{\text{intrinsic, DUT}}^2 + \sigma_{\text{multiple scattering}}^2 + \sigma_{\text{telescope}}^2. \tag{5.2}$$

(a) X Correlation before alignment

(b) Y Correlation before alignment

(c) X Correlation after alignment

(d) Y Correlation after alignment
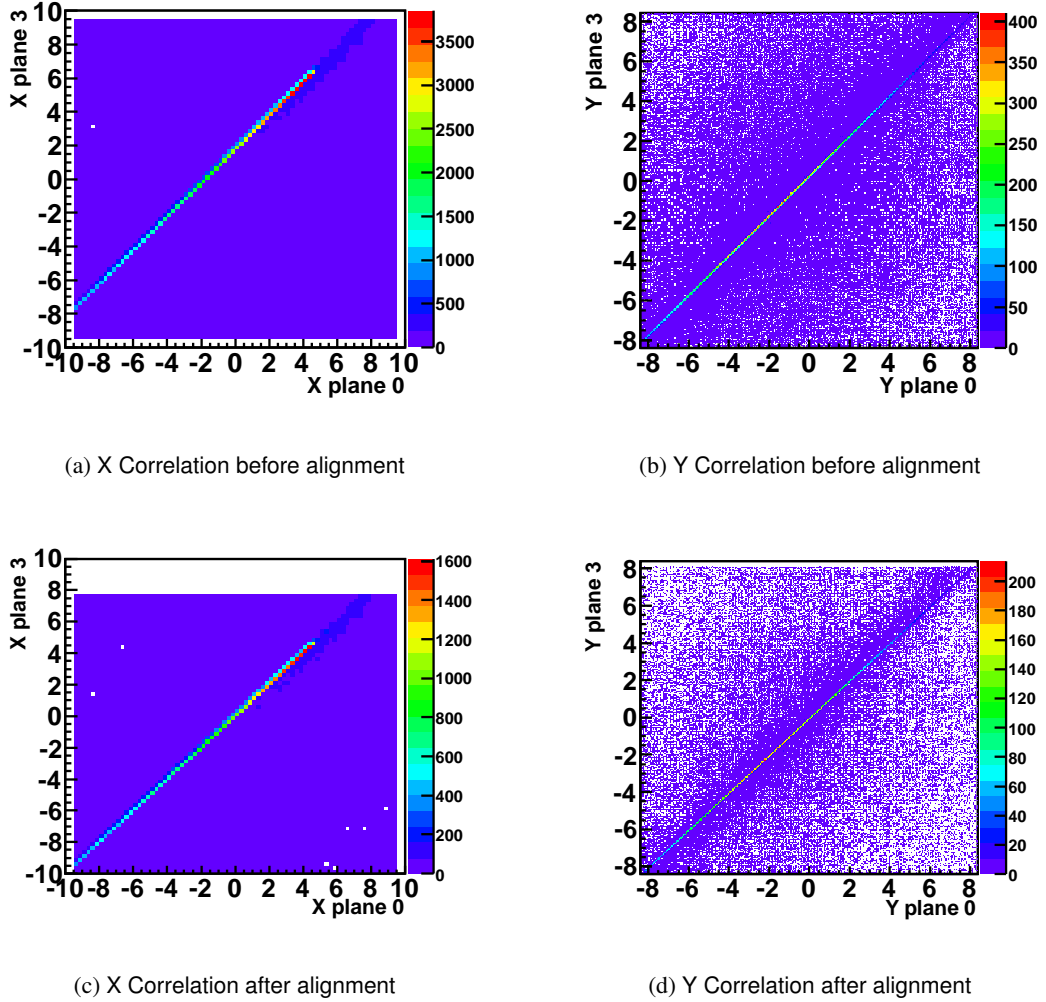
Figure 5.5: Alignment of telescope planes. The correlation plots of both directions between the first and last plane are shown before and after alignment. As can be seen, small mismatches in the sensor positioning can be corrected for using the offline analysis.

First, for binary readout, the intrinsic resolution is $d/\sqrt{12}$, where d is the pixel pitch of the DUT. Second, the effects of multiple scattering can be calculated, see chapter 2.3.1 table 2.1. For the energy used at CERN it can be completely neglected. Third, the pointing resolution of the telescope $\sigma_{\text{telescope}}$ depends on the geometrical configuration of the telescope as well as on the intrinsic resolution of the telescope planes:

$$\sigma^2_{\text{telescope}} = k \cdot \sigma^2_{\text{intrinsic, plane}} \qquad k = \frac{\sum_i^N z_i^2}{N \sum_i^N z_i^2 - \left(\sum_i^N z_i\right)^2} \qquad (5.3)$$

where k is a geometrical scaling factor, N is the number of planes used to calculate the track and z_i is the position of the planes. In the case that the DUT and the reference plane are of the same pixel detector, the overall telescope resolution can be derived directly from the measured residual width $\sigma_{residual, plane}$:

$$\sigma_{telescope}^2 = \frac{k}{1+k}\sigma_{residual, plane}^2 \qquad (5.4)$$

where $\sigma_{residual, plane}$ is the residual of a telescope reference plane that is not included in the track fitting of the telescope in the given configuration. As such, for the FE-I4 telescope (with four planes) four different telescope geometries are used to estimate the pointing resolution of the telescope. The intrinsic resolution of the FE-I4 reference planes is 72 μm in the long pixel pitch direction and 21 μm in the short pixel pitch direction. The error due to the extrapolation of the track can be calculated for a given geometry, as shown in figure 5.6 for the different energies used in this thesis for various DUT placements. For simplicity this calculation is done here for a setup of only two planes and in dependence of the position of the DUT. This calculation, which is done separately for
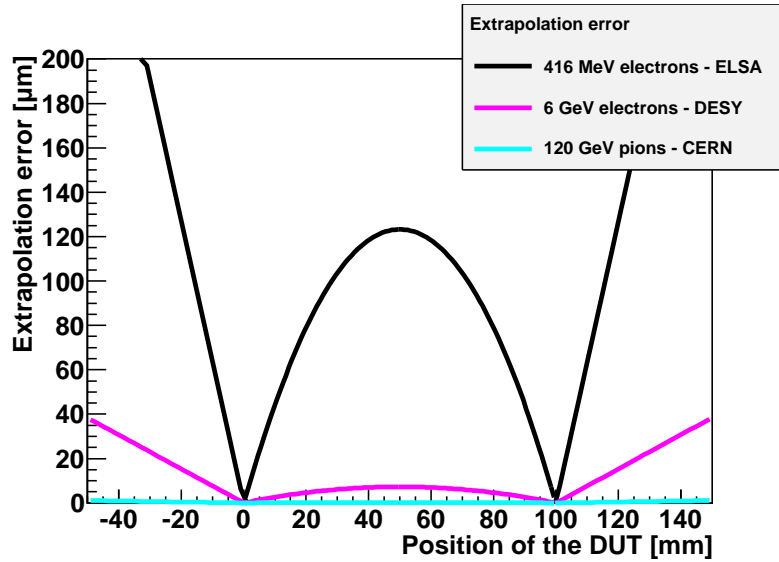
Figure 5.6: Extrapolation error in dependence of the position of the DUT for a setup of two telescope reference plane modules and different energies.

the region in front of the first telescope plane σ_{front}, in between the two planes σ_{middle} and behind the second plane σ_{back} depends on the z position of the planes and DUT, on the multiple scattering angle θ, on the parallel shift in air y_0 and on the distance between the two planes d. Here a distance

of 10 cm is used. The formulas used for this simulation are [35]:

$$\sigma_{\text{front}} = (z_{\text{first}} - z_{\text{DUT}}) \sqrt{\left(\frac{y_0}{d}\right)^2 + (\theta_{\text{first}})^2} \tag{5.5}$$

$$\sigma_{\text{back}} = (z_{\text{DUT}} - z_{\text{last}}) \sqrt{\left(\frac{y_0}{d}\right)^2 + (\theta_{\text{last}})^2} \tag{5.6}$$

$$\sigma_{\text{middle}} = \frac{(d - z_{\text{DUT}}) \cdot z_{\text{DUT}}}{d} \tan \theta_{\text{DUT}} \tag{5.7}$$

Nevertheless, conclusions about the estimated resolution can be drawn from that configuration. The extrapolation error for the 416 MeV e^- of the ELSA setup is about 100 μm whereas the error reduces to below 10 μm for the 6 GeV e^- at DESY. The error of the setup at CERN is negligible. A zoom into the plot to below 2 μm shows the error expected at CERN, see figure 5.7. As can be seen, the extrapolation error reduces to below 2 μm. Consequently, the contribution from the intrinsic resolution has the biggest effect on the spatial resolution and is of order $\mathcal{O}(10 - 100 \, \mu\text{m})$ while the effects of multiple scattering and extrapolation add less than order $\mathcal{O}(1 \, \mu\text{m})$, in between the planes. As all factors add up quadratically, the influence of the intrinsic resolution of the sensors on the pointing resolution of the FE-I4 beam telescope is, for high energy particles, even more dominating over the other mentioned effects.
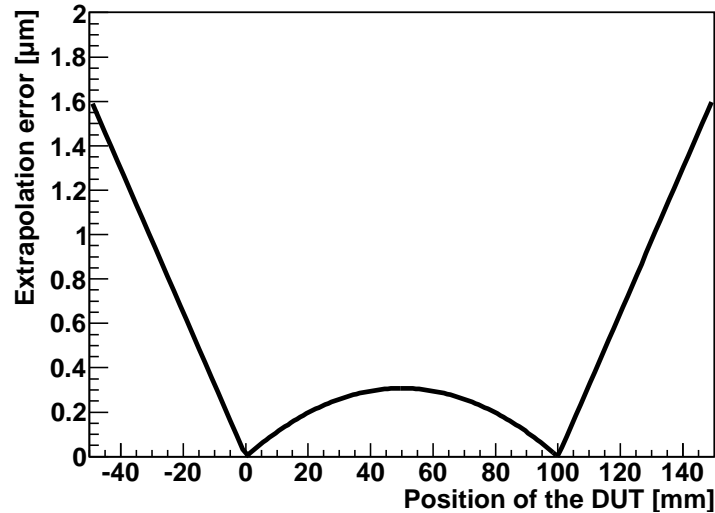
Figure 5.7: Extrapolation error in dependence of the position of the DUT for a setup of two telescope reference plane modules and the energy used for the measurement done at CERN.

Chapter 6

Summary and outlook

In this thesis a new beam telescope which makes use of FE-I4 readout chip based pixel modules as reference planes was developed. The DAQ of this FE-I4 telescope is composed of two parts, the first being the testing system `USBpix` for the reference plane specific DAQ and the second one being the telescope DAQ `EUDAQ` used for the combination of the data from all planes to telescope data. As a common hardware part to the FE-I4 telescope and the `EUDET` telescope, the `TLU` is used for the trigger generation.

A new triggering scheme, the ROI trigger, for general purpose beam telescopes making use of one FE-I4 based reference plane was developed and commissioned. The new triggering scheme has the advantage of a programmable sensitive region which can be as small as one FE-I4 pixel (50 μm x 250 μm) and as big as the whole FE-I4 pixel matrix (20 mm x 16.8 mm).

First, tests of the ROI trigger together with a `EUDET` telescope show the compatibility of the triggering signal with the `TLU`. The resulting hitmaps of the `EUDET` telescope reference planes reflect the sensitive trigger region and are the first proof of principle of the ROI trigger together with a beam telescope. Second, different regions of the ROI were tested in order to show the full flexibility of the trigger. With a setup of only two FE-I4 telescope reference planes, one was used to trigger the DAQ of both sensors. Consequently the possibility of triggering also the FE-I4 telescope with the ROI was shown. Third, the full commissioning of the ROI was done together with a `DEPFET` DUT. Through the selection of a sensitive trigger region covering only the `DEPFET` DUT an increase in track efficiency up to 80 % was possible.

In the near future, an upgraded version of the existing `AIDA` telescope is expected. The usage of

one FE-I4 based reference plane is already a considered option. That plane cannot only be used for a selective trigger in order to increase the track efficiency, as was shown in this thesis, but it can also serve as a timing reference. This feature has been already used in other beam tests and the functionality is well established, yet it is not integrated into the `EUDET` telescope.

The modular approach of the `EUTelescope` analysis software package should make the extensions necessary for the analysis of the FE-I4 beam telescope data easily accomplished. All steps of the analysis have been performed, a final results about the spatial resolution is expected soon.

Further, in order to increase the pointing resolution of the FE-I4 beam telescope, a rotation of two of the planes by 90 ° is considered and needs to be verified experimentally. By doing so one would exploit the short pixel pitch for both plane directions. Another feature to explore and test further is the high rate capability of the FE-I4 beam telescope. The setup of the FE-I4 beam telescope at `ELSA` is suitable for that kind of measurements.

Bibliography

[1] *ATLAS Homepage*. URL: http://atlas.web.cern.ch/Atlas/Collaboration/.

[2] *LHC Homepage*. URL: http://lhc.web.cern.ch/lhc/.

[3] *CERN Homepage*. URL: http://public.web.cern.ch/public/.

[4] ATLAS Collaboration. 'Observation of a New Particle in the Search for the Standard Model Higgs Boson with the ATLAS Detector at the LHC'. In: *Physics Letters B* (). Submitted in August 2012 to Physics Letters B. URL: http://atlas.web.cern.ch/Atlas/GROUPS/PHYSICS/PAPERS/HIGG-2012-27/HIGG-2012-27.pdf.

[5] CMS Collaboration. 'Observation of a new boson at a mass of 125 GeV with the CMS experiment at the LHC'. In: *Physics Letters B* (). Submitted in August 2012 to Physics Letters B. URL: http://arxiv.org/pdf/1207.7235.pdf.

[6] Marlon Barbero et al. 'The FE-I4 Pixel Readout Chip and the IBL Module'. In: *Proceedings of Science* AIDA-PUB-2011-001 (2011).

[7] *EUDET Homepage*. URL: http://www.eudet.org/.

[8] *EUDAQ Homepage*. URL: http://eudaq.hepforge.org/.

[9] *EUTelescope Homepage*. URL: http://eudaq.hepforge.org/Eutelescope/.

[10] Malte Backhaus et al. 'Development of a versatile and modular test system for ATLAS hybrid pixel detectors'. In: *Nucl.Instr.and Meth.A* 650 (2011), pp. 37–40.

[11] Malte Backhaus. 'Development of an USB-based test system for the FE-I3 readout chips of the ATLAS pixel detector and Noise Occupancy Studies'. Diplomarbeit. Rheinische Friedrich-Wilhems Universität Bonn, 2009.

[12] Kenzo Nakamura. *PDG: Review of particle physics 2010*. 2010. URL: http://cdsweb.cern.ch/record/1299148?ln=en.

[13] Gerhard Lutz. *Semiconductor Radiation Detectors*. Springer Verlag, 1999.

[14] Helmuth Spieler. *Semiconductor Detector Systems*. Oxford Science Publications, 2005.

[15] ATLAS Collaboration. *ATLAS Insertable B-Layer Technical Design Report*.

[16] G. Aad et al. 'ATLAS pixel detector electronics and sensors'. In: *Journal of Instrumentation* 3.07 (2008), P07007. URL: http://stacks.iop.org/1748-0221/3/i=07/a=P07007.

[17] Sebastian Schultes. 'Entwicklung eines Strahl Teleskops mit ATLAS Pixeldetektoren'. Diplomarbeit. Rheinische Friedrich-Wilhems Universität Bonn, 2011.

[18] M. Garcia-Sciveres et al. 'The FE-I4 pixel readout integrated circuit'. In: *Nuclear Instruments and Methods in Physics Research Section A: Accelerators, Spectrometers, Detectors and Associated Equipment* 636 (2011), S155 –S159. URL: http://www.sciencedirect.com/science/article/pii/S0168900210009551.

[19] Leonardo Rossi et al. *Pixel Detectors: From Fundamentals to Applications*. Springer Verlag, 2006.

[20] Teaching. *Semiconductor Lab. Course Manual University of Bonn*.

[21] Malte Backhaus. *Characterization of new hybrid pixel module concepts for the ATLAS Insertable B-Layer upgrade*. 2012.

[22] Jens Janssen. 'Development of an FPGA-based FE-13 pixel readout system and characterization of novel 3D and planar pixel detectors'. Diplomarbeit. Rheinische Friedrich-Wilhems Universität Bonn, 2010.

[23] Aleksander Filip Zarnecki and Piotr Niezurawski. *EUDET Telescope Geometry and Resolution Studies*. URL: http://arxiv.org/pdf/physics/0703058.pdf.

[24] David Cussans. *Description of the JRA1 Trigger Logic Unit (TLU)*. URL: http://www.eudet.org/e26/e28/e42441/e57298/EUDET-MEMO-2009-04.pdf.

[25] Maren Eberhardt. 'Messung und Korrektur der Arbeitspunkte während der Energierampe am Stretcherring von ELSA'. PhD thesis. Rheinische Friedrich-Wilhems Universität Bonn, 2010.

[26]   Crystal Barrel Collaboration. URL: `http://www1.cb.uni-bonn.de/`.

[27]   Kathrin Fornet-Ponse. 'Die Photonenmarkierungsanlage für das Crystal-Barrel/TAPS-Experiment an ELSA'. PhD thesis. Rheinische Friedrich-Wilhems Universität Bonn, 2009.

[28]   J. Kemmer and G. Lutz. 'New Detector Concepts'. In: *Nucl. Instrum. Meth. A* (1987).

[29]   C. Marinas and M. Vos. 'The Belle-II DEPFET pixel detector: A step forward in vertexing in the superKEKB flavour factory'. In: *Nucl.Instrum.Meth.* A650 (2011), pp. 59–63.

[30]   *ILC Homepage*. URL: `http://www.linearcollider.org/`.

[31]   *Millepede II software homepage*. URL: `https://www.wiki.terascale.de/index.php/Millepede_II`.

[32]   Silvan Kuttimalai. *Resolution Measurements with the Eudet Pixel Telescope*. Summer school program DESY. 2011. URL: `http://www.desy.de/f/students/2011/reports/kuttimalai.pdf`.

[33]   *ESTAR-NIST*. URL: `http://physics.nist.gov/PhysRefData/Star/Text/ESTAR.html`.

[34]   A. Bulgheroni. 'Results from the EUDET telescope with high resolution planes'. In: (). URL: `http://www.eudet.org/e26/e26/e27/e50990/eudet-report-09-02.pdf`.

[35]   Markus Keil. 'Teststrahlmessungen am BIER ET PASTIS-Pixelchip fr das ATLAS-Experiment mit einem Silizium-Mikrostreifen-Strahlteleskop'. PhD thesis. Rheinische Friedrich-Wilhems Universität Bonn, 1998.

List of Figures

List of Tables

Acknowledgements